GEOCHEMISTRY AND PETROGENESIS OF THE VANCE SEAMOUNTS: A NEAR-RIDGE SEAMOUNT CHAIN ADJACENT TO THE JUAN DE FUCA RIDGE

By

RACHEL ELIZABETH WENDT

A THESIS PRESENTED TO THE GRADUATE SCHOOL
OF THE UNIVERSITY OF FLORIDA IN PARTIAL FULFILLMENT
OF THE REQUIREMENTS FOR THE DEGREE OF
MASTER OF SCIENCE

UNIVERSITY OF FLORIDA

2008

To my family.

ACKNOWLEDGMENTS

I would like to thank several people for their support and contributions during my tenure as a graduate student. First, I would like to express my deepest thanks to my advisor, Mike Perfit, for all his guidance and financial support during my Master's research. I would also like to thank Dave Foster, Phil Neuhoff, and Ray Russo for their support as committee members and also whose doors were always open when I needed them. Thanks also goes to Matt Smith and George Kamenov for assistance with analytical techniques, without them, there would be no data to talk about!

I am also grateful to the Monterey Bay Aquarium Research Institute for providing the funding and opportunity to participate in the Vance research cruise, it was an amazing experience, one that I will not soon forget. I would also like to thank the crew and scientific party, especially Dave Clague and Jenny Paduan for their contributions of data and helpful comments on data interpretation and abstracts. Big thanks go to Liz Cornejo and Brian Cousens of Carleton University, for their contributions to my research and interpretations, as well as providing the isotopic data that makes the story the Vance Seamounts complete.

A great deal of thanks goes to Dorsey Wanless and Allison Fundis for their constant mental and emotional support during the past three years. I would also like to thank the other faculty and students of the Geological Sciences department, it has been a pleasure knowing everyone. Last, but certainly not least, I would like to thank my family (especially Tommy) for always listening when I ranted about writing, or rocks, or teaching, or lab work, etc.! I thank them for their constant encouragement and support.

TABLE OF CONTENTS

page

LIST OF TABLES

LIST OF FIGURES

Abstract of Dissertation Presented to the Graduate School
of the University of Florida in Partial Fulfillment of the
Requirements for the Degree of Master of Science

GEOCHEMISTRY AND PETROGENESIS OF THE VANCE SEAMOUNTS: A NEAR-RIDGE SEAMOUNT CHAIN ADJACENT TO THE JUAN DE FUCA RIDGE
By

Rachel Elizabeth Wendt

December 2008

Chair: Michael Perfit
Major: Geology

The Vance Seamounts are a NW-SE trending chain of eight seamounts (Vance A through G) at approximately 45° 15'N and 130° 20'W on the flanks of the southern Juan de Fuca Ridge (SJdF). The chain consists of truncated cone-shaped volcanoes (A, C, E/D, and F) and large areas of disorganized volcanic constructs comprised of numerous small cones and volcanic ridges (B and G). Geologic evidence suggests that the seamounts progressively increase in age from the southeast (G) to the northwest (A). Eruptive products include pillow lavas, sheet flows, massive flows, and volcaniclastites. During July-August 2006, samples of the seamounts were collected using the *ROV Tiburon*; volcanic glass and whole rock samples were analyzed for major element, trace element, and isotopic compositions.

Analyses show there are significant geochemical differences in lava composition between the seamounts in the chain, as well as within individual seamounts. Overall, Vance lavas are more primitive and exhibit greater diversity than samples from the adjacent SJdF. Major element data indicate that all samples are subalkaline-MOR basalts, but a range of depleted to moderately enriched varieties exist (0.02 to 0.31 wt.% K_2O). Incompatible trace element data indicate samples range from very depleted to slightly enriched ($[La/Sm]_N$ 0.354 to 1.07; $[Ce/Yb]_N$ 0.498 to 1.59; Zr/Y 1.69 to 3.86). Variations in major and trace elements along with geochemical

modeling suggest differing sources along with different extents of partial melting, rather than shallow level processes like fractional crystallization as the reason for most of the geochemical diversity. Sr-Nd-Pb isotope data supports slight variations in source characteristics as well as mixing between end members ($^{87}Sr/^{86}Sr$ = 0.702477 to 0.702687; $^{206}Pb/^{204}Pb$ = 18.117 to 18.816; and $^{143}Nd/^{144}Nd$ = 0.513052 to 0.513181). Variations are just outside of analytical error for many of the seamounts, but fall along a general mixing trend between the Depleted Mantle (DM) and High μ (HIMU) mantle reservoirs. Mantle heterogeneity beneath the Vance Seamounts appears to be on a very small scale, with each seamount showing significant incompatible trace element and isotopic variations that are somewhat correlated. The very depleted nature of many of the Vance samples compared to adjacent ridge samples is similar to observations made at other near-ridge chains (for example the Lamont Seamounts, Heck Seamounts), but the presence of enriched mid-ocean ridge basalt is unusual for both the Southern Juan de Fuca Ridge and other near-ridge seamounts. These results support a "veined mantle" model for the Northeastern Pacific mantle. The near-ridge seamount samples appear to record small scale heterogeneity of the underlying mantle because individual melt batches undergo only minor amounts of differentiation and mixing whereas the inherent mantle diversity is homogenized for on-axis ridge samples due to the more steady-state shallow magmatic processes that occur in sub-axial magma bodies.

CHAPTER 1
INTRODUCTION

One of the primary goals of the study of mid-ocean ridges is to understand the magmatic processes that occur in the mantle which are ultimately expressed by the volcanic rocks exposed on the seafloor. Near-ridge seamounts are one such expression of volcanic activity that represent an important, yet poorly studied, accretionary process at the seafloor. Even though volcanism at mid-ocean ridges is concentrated within the neovolcanic zone (1-4 km wide), off axis eruptions, like those of near-ridge seamount chains, can add significant volume to the oceanic crust [*Perfit and Chadwick*, 1998].

Seamounts, described first by *Menard* [1964], have long been recognized as one of the most abundant volcanic edifices on Earth. Seamount chains have been of great interest in understanding mantle processes such as the dynamics of mantle plumes and the composition of geochemical reservoirs in the mantle. However, there are many seamounts located close to oceanic spreading centers (i.e. near-ridge) and petrologic and geochemical data suggests that they are chemically distinct from intra-plate hot spots, such as Hawaii [*Barr*, 1974; *Davis et al.*, 1979; *Batiza and Vanko*, 1984; *Fornari et al.*, 1988a; 1988b; *Epp et al.*, 1989; *Leybourne and Van Wagoner*, 1991; *Raddick et al.*, 2002]. These seamounts commonly occur as linear chains, but also include individual seamounts and are found adjacent to fast, intermediate, and slow spreading centers [*Fornari et al.*, 1987; *Batiza et al.*, 1989]. Bathymetric imaging has revealed that there are ridge-parallel faults on top of and on the seafloor flanking these seamounts [*Menard*, 1969; *Lonsdale and Spiess*, 1979; *Hammond*, 1997; *Clague et al.*, 2000]. These features indicate that these seamounts formed in a near-ridge environment (within 30-40 km of the ridge axis) where this type of faulting is still active. Near-ridge seamounts are present in several distinct tectonic environments, being preferentially located near transforms, fracture

zones, overlapping spreading centers (OSCs), and inflated ridge crest segments [*Batiza,* 1982; *Fornari et al*., 1988a]. Although the controls on near-ridge seamount formation and location are still unclear, their presence in these distinct areas suggests that tectonic as well as magmatic processes are important.

Petrologic and geochemical studies from near-ridge seamount lavas (i.e. Lamont, Cobb-Eickelberg, President Jackson, Heck and Heckle Seamounts) have indicated that these seamounts have quite different geochemical signatures than those of typical mid-ocean ridge basalts (MORB) erupted on-axis [*Batiza and Vanko,* 1984; *Fornari et al.,* 1988a; *Allan et al.,* 1989; *Batiza et al.,* 1989; *Finney*, 1989; *Desonie and Duncan;* 1990; *Leybourne and Van Wagoner,* 1991; *Niu and Batiza,* 1997; *Davis and Clague,* 2000]. The lavas from near-ridge seamounts are in general more primitive (higher MgO) in composition and depleted in the most incompatible trace elements relative to mid-ocean ridge basalts (MORB). However, some near-ridge seamount chains have also erupted both depleted and enriched basalts as well as alkalic basalts [*Cousens,* 1988; *Niu and Batiza*, 1997]. These lavas have isotopic signatures that are characteristic of both enriched and depleted mantle signatures (relative to ridge-axis lavas), but in general these isotopic signatures are similar to the sources common to the region and are all characteristic of the wide variety of MORB that have been studied world-wide [*Eaby et al*., 1984; *Cousens,* 1988; *Fornari et al*., 1988a; *Davis and Clague,* 1987; *Cousens,* 1996a; *Desonie and Duncan,* 1990].

The diverse geochemistry found at near-ridge seamounts suggests that they can be important indicators of dynamics and heterogeneity in the mantle beneath ridge systems. Both tectonic and magma supply variability seem to provide reasonable explanations for the differences in chemistry of on-axis basalts and off-axis seamount basalts, but it has been suggested that near-ridge seamounts tap different mantle sources or are undergoing different

mantle processes than their on-axis counterparts [*Fornari et al.*, 1988b; *Finney*, 1989; *Smith et al.*, 1994; *Perfit and Chadwick*, 1998; *Clague et al.*, 2000]. *Fornari et al.* [pg. 79, 1988b] suggested that the variations observed in the geochemistry between the Lamont Seamounts and the adjacent East Pacific Rise (EPR) around 10° N reflect "fundamental differences in melting dynamics and the process of magma ascent and storage" that function between the two environments.

Many authors have also suggested that seamounts provide the best evidence for small-scale mantle heterogeneities [*Batiza and Vanko*, 1984; *Zindler et al.*, 1984; *Fornari et al.*, 1988a; *Leybourne and Van Wagoner*, 1991; Cousens, 1996a; Davis *and Clague*, 2000]. These compositional variations are often masked at the ridge axis, because of mixing, homogenization, and differentiation of melt batches in sub-axial magma bodies [*Batiza and Vanko*, 1984; *Langmuir et al.*, 1992; *Cousens*, 1996a]. While the idea of compositional heterogeneity in the upper mantle is well accepted, the nature and scale of this heterogeneity is still debated. The primitive nature of near-ridge seamount lavas as well as the lack of evidence for mixing and extensive fractionation make them good candidates for studying the compositional variety in the upper mantle. Also, the presence of distinct geochemistry between seamounts in a chain as well as on an individual seamount suggests that the mantle is heterogeneous on a relatively small scale (< few km).

The Vance Seamount Chain is one of many morphologically similar near-ridge seamount chains in the Northeast Pacific on the flanks of the Juan de Fuca Ridge (Figure 1-1). The chain consists of seven volcanic cones (Vance A through Vance G; from northwest to southeast; Figure 1-2) that lie ~19 km west of the ridge axis on the Pacific Plate. The morphology, petrology, and geochemistry of NE Pacific seamount chains, including the President Jackson, Heck and Heckle,

and Cobb-Eickelberg Seamount Chains, have been fairly well studied. The Vance Seamount Chain is one that is *not* well studied. Although a few morphological studies have included the Vance Seamounts, very little geochemical data is available.

This thesis is part of a larger investigation into the Vance Seamounts, which includes both geochemistry and volcanology of the chain; in particular this thesis focuses on the trace element geochemistry of the Vance lavas. This study will describe geochemical variations in the Vance Seamounts, compare those variations to other near-ridge seamount chains, and compare the lavas to those erupted on the ridge axis. This study proposes that near-ridge seamounts show considerable geochemical variation from lavas found on axis and that this variation may be a consequence of differences in source composition and/or styles of partial melting rather than simply a shallow-level process such as fractional crystallization.

Samples from the Vance Seamount Chain were recovered using the *ROV Tiburon* in the summer of 2006. Previous research cruises in the region recovered seamount samples by dredging, which limits the control on location of lava samples, thus making it difficult to determine geochemical variation among seamounts and within individual seamounts. This project is one of the most detailed and extensive studies of near-ridge seamounts in the NE Pacific. The sample set recovered from the Vance Seamounts is extraordinarily complete and allows for detailed investigation into the petrogenesis of near-ridge seamount lavas.

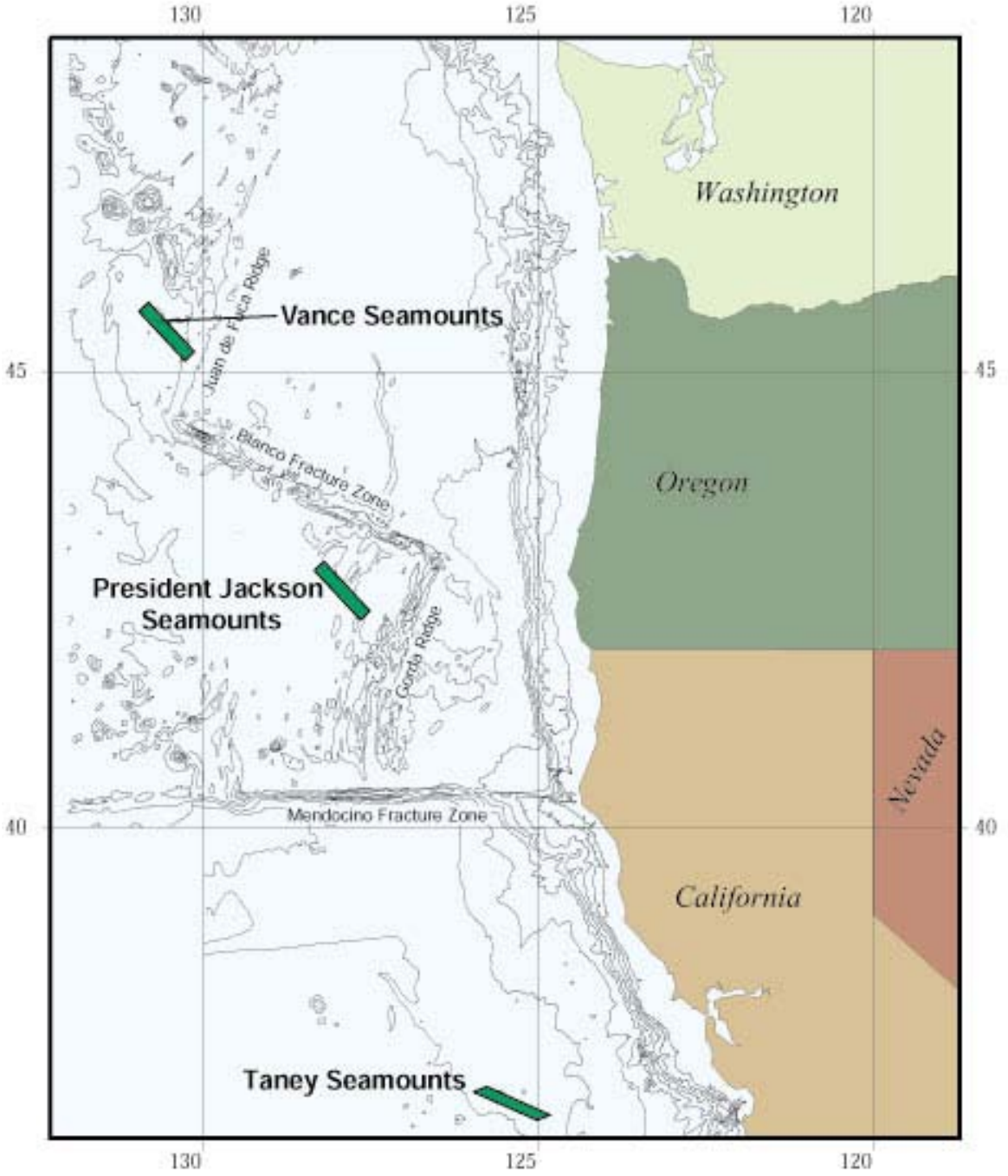

Figure 1-1. Near-ridge seamount chains in the Northeast Pacific (image courtesy MBARI).

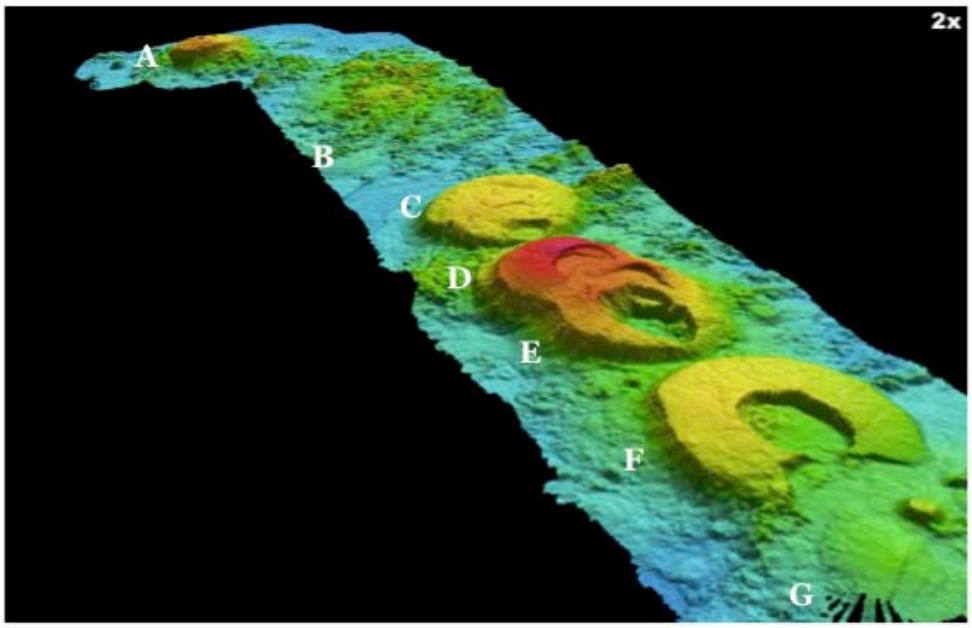

Figure 1-2. Close up perspective side scan image of the Vance Seamount Chain with seamount names. Vertical exaggeration is 2x (image courtesy MBARI).

CHAPTER 2
REGIONAL GEOLOGY

The Juan de Fuca Ridge (Figure 2-1) is a moderate spreading rate ridge (6 cm/yr full rate) and is located approximately 600 km off the coast of Washington and Oregon. It spans nearly 500 km between the Blanco (44º 27' N) and Sovanco (48º 50' N) fracture zones and has been divided into seven morphologically and tectonically distinct segments [*Karsten et al.,* 1990]. Seamounts and chains of seamounts are especially common along fast spreading ridges, but can also be found along moderate spreading ridges. The distribution of these seamount chains is commonly asymmetric, with more seamounts being located on one side of the ridge than the other [*Davis and Karsten*, 1986]. No symmetrical seamount chains occur on the Juan de Fuca Plate. Several studies have focused on the morphology and geochemistry of samples dredged from near-ridge seamount chains in the northeastern Pacific (e.g. President Jackson, Cobb-Eickleberg, Taney, Heck and Heckle Seamounts), but there is little geochemical data available for the Vance Seamounts [*Leybourne and Van Wagoner*, 1991; *Hammond*, 1997; *Clague et al*., 2000]. The control on sample location and the abundance of geochemical analyses incorporated in the Vance Seamounts 2006 project (of which this study is a part of) provides one of the most detailed pictures of this class of seamounts.

The Vance Seamounts

The Vance Seamount Chain is located on the southern flanks of the Juan de Fuca Ridge at approximately 45° 15'N and 130° 20'W (Figure 2-1). This linear seamount chain lies on the Pacific Plate extending northwest at an azimuth of ~325º and is positioned near the overlapping spreading center between the Cleft and Vance segments of the JdFR. It lies on oceanic crust between 2.55 Ma in the northwest and 0.78 Ma in the southeast [*Cande and Kent,* 1995]. It consists of seven volcanic cones (Vance A through G, Figure 2-2) that are morphologically

similar to many other seamount chains located along ridges in the eastern Pacific [*Hammond,* 1997; *Clague et al*., 2000]. This suggests that a similar sequence of processes occurred during each volcano's formation and that the Vance Chain is a typical example of near-ridge seamount chains [*Hammond,* 1997]. The chain has been suggested to parallel absolute or relative plate motion vectors [*Davis and Karsten,* 1986], but more recently has been proposed to parallel subaxial asthenospheric motion [*Schouten et al.,* 1987; *Clague et al.,* 2000]. The height of the individual seamounts ranges from 440 m to 1140 m above the surrounding seafloor and their volumes range from 15-67 km^3 [Clague et al., 2000].

The chain consists of truncated cone-shaped volcanoes (A, C, E/D, and F) and large areas of disorganized volcanic constructs comprised of numerous small cones and volcanic ridges (B and G) (Figures 1-2 and 2-2). Each of the volcanic cones contains at least one caldera (some are nested), which is offset toward the ridge and all have relatively flat floors [*Hammond,* 1997; *Clague et al.,* 2000]. Geologic evidence (e.g. cross-cutting relationships between calderas in a single seamount and overlap between seamounts) suggests that the seamounts progressively increase in age from the southeast (G) to the northwest (A) and that the cones were formed in the near ridge environment (e.g. they are cut by ridge-parallel faults). The circular nature of the volcanic cones (in map view) suggests that the major cone building stage was centered directly over a magma source and that the calderas are due to collapse after withdrawal of lava [*Hammond,* 1997; *Clague et al.,* 2000]. *Hammond* [1997] suggests a simple model to explain why all collapse features face the ridge. As plate motion transports the volcanic cones away from the magma source in the lithosphere, the volcanoes' magma supply conduits lag behind. Eventually, the supply conduits are abandoned in favor of new, more direct conduits to the surface and the volcano becomes extinct. This accounts for the nature of the nested calderas

common on the Vance volcanoes as well as for the breached openings (Vance F, reminiscent of a half-eaten doughnut, Figure 2-2). These types of morphology and collapse features are extremely common among near-ridge seamount chains [*Lonsdale and Spiess,* 1979; *Batiza,* 1982; *Batiza and Vanko,* 1983; *Hammond,* 1997; *Clague et al.,* 2000].

Hammond [1997] also suggests that the morphology of these volcanic cones is dependent upon their relatively rapid construction (i.e. the cone was formed while still directly over the stationary magma source). His model includes two major phases: 1) the voluminous, rapid constructional phase, and 2) the collapse phase as magma supply diminishes. *Clague et al.* [2000] take this a step further and suggests that the Vance Seamounts (as well as other near-ridge seamounts) formed by voluminous, episodic pulses of magma, between which the magmas cooled and solidified or intruded into ridge-parallel fractures. The multiple calderas and collapse features found on these seamounts are attributed to this succession of magma withdrawals from a shallow magma chamber. From the morphology of the Vance, President Jackson, and Taney Seamounts and experimental results by *Marti et al.* [1994] and *Roche et al.* [2000], they estimated that the volumes of these magma chambers were about 3 km^3. There has been much debate as to whether or not these near-ridge seamounts do indeed have crustal magma chambers. The primary argument against magma chambers is that these seamounts have primitive (high MgO) lavas, lack evidence of crystal fractionation (e.g. simple mineralogy), and lack evidence for magma mixing (e.g. a lack of crystal zoning, crystal resorption, and xenocrysts) [*Fornari et al.,* 1988a]. *Clague et al.* [2000] suggest that these signatures can be produced if the magmas *do* reside in crustal magma chambers, but do so only for a short period of time. This can be achieved by high magma supply rates and rapid movement of the lavas from the mantle to the surface.

The seamounts without well-defined cones (B and G) consist of disorganized volcanic constructs, but have erupted volumes similar to those of the large circular volcanoes. There are several mechanisms that might explain their origin. First, it is possible that this type of disorganized volcanism precedes a more organized, focused cone-building stage; this may be what is happening at Vance G, which may still be active [*Hammond,* 1997]. Secondly, these structures may have formed during a period with smaller, more frequent eruptions through more permeable oceanic crust rather than less frequent, longer lived, voluminous eruptions that build the cones [*Clague et al.,* 2000].

Although there are no absolute ages for the Vance Seamounts, estimates of the chain's lifespan and the ages of individual volcanoes have been made. Based on the rate of subaxial asthenospheric flow and spreading rates of the ridge near the Vance Chain, the time to form the chain was at a minimum 1.67 Myr (the chain is presumably still active). The oldest volcano (Vance A) initially formed on oceanic crust that was 0.9 Myr, which corresponds to its location ~26 km off axis [*Clague et al.,* 2000]. *Hammond* [1997] calculated the lifespan of an individual seamount within a chain using structural evidence, which was later revised by *Clague et al.* [2000] to include the fact that the chain's propagation rate is dependent on subaxial asthenospheric flow. They determined that the volcanic cycle of a seamount in the Vance Chain is approximately 75,000 years. This lead them to a conclusion (based also on assumptions made about the size of crustal magma chambers, seamount volumes, observations made at sub-aerial volcanoes, and ridge propagation rates) that eruptive events on near-ridge seamounts occurred on average once every 1,000 to 10,000 years.

Observations from Other Near-ridge Seamounts in the Eastern Pacific

The geochemistry and petrology of other near-ridge seamount chains in the eastern Pacific have been fairly well studied. These seamount chains are morphologically similar to the

Vance Seamounts and consist of seven to eight seamounts per chain. The lavas from these seamounts are in general more primitive and are more geochemically diverse than the adjacent ridge.

The Heck and Heckle Seamounts, located west of the West Valley ridge segment, have lavas that are very primitive (Mg# 68.7-59.5) and have restricted incompatible element ranges. They have very highly depleted (DMORB) compositions (Zr/Y 1.9-2.4) and have LREE depleted chondrite-normalized REE patterns ($[La/Sm]_N$ 0.65-0.77). These compositions are on the lowest end of the spectrum for MORB. The lavas are more compositionally restricted and show radiogenic isotopic signatures characteristic of more depleted mantle sources (less radiogenic $^{87}Sr/^{86}Sr$ and Pb ratios; more radiogenic $^{143}Nd/^{144}Nd$) than the adjacent West Valley Ridge segment. These seamounts differ from other near-ridge seamounts (e.g. Lamont and President Jackson Seamounts) in that they do not show the relatively large range in trace elements common to this type of seamount [*Leybourne and Van Wagoner*, 1991; *Van Wagoner and Leybourne,* 1991; *Cousens et al.,* 1995].

The President Jackson Seamounts also have primitive compositions (Mg# to 69.5), but are all NMORB. The incompatible elements range from highly depleted to slightly depleted in incompatible elements [K_2O 0.07-0.24 wt. %; $(La/Sm)_N$ 0.54-0.86] and the REE patterns exhibit depletions in the LREEs. The isotopic signatures also range from those characteristic of depleted mantle signatures to those characteristic of enriched mantle signatures (more radiogenic $^{87}Sr/^{86}Sr$ and Pb ratios; less radiogenic $^{143}Nd/^{144}Nd$) and Pb isotopic ratios trend toward typical EMORB values. The lavas from the President Jackson Seamounts are in general more heterogeneous than lavas from the adjacent Gorda Ridge. They have similar incompatible trace element patterns to the ridge lavas, but on average are more depleted. The isotope ratios however, are more typical

of enriched mantle signatures in the lavas from the President Jackson Seamounts than basalts from the adjacent Gorda Ridge [*Davis and Clague*, 2000].

Although there are slight variations in their trace element and isotopic compositions, lavas from the Heck, Heckle, and President Jackson Seamount Chains are all more primitive compared to those from the adjacent ridge. None of the lavas from these chains show evidence for magma mixing or for extensive amounts of fractional crystallization. This supports the hypothesis proposed by *Clague et al.* [2000] that these seamount lavas did not reside long in crustal magma chambers [*Leybourne and Van Wagoner*, 1991; *Davis and Clague*, 2000].

The Lamont Seamounts, located along the East Pacific Rise, also share many characteristics common to near-ridge seamount chains, even though the EPR is a fast rate spreading center. The Lamont Seamount lavas are also more primitive (Mg# to 71) than lavas found on the EPR. They have low incompatible element concentrations (e.g. La 0.96-3.77 ppm; Hf 1.19-2.69 ppm) and LREE-depleted trace element patterns [$(La/Sm)_N$ 0.26-0.57] relative to the basalts found on-axis. The isotopic ratios range from less radiogenic to more radiogenic than the adjacent EPR MORB values. In particular, the range in Pb isotopic ratios for the Lamont Seamounts is significantly greater than that found on the EPR, Juan de Fuca, and Gorda Ridges [*Fornari et al.*, 1988a].

Although there is very limited geochemical data available for the Vance Seamounts, the few published data sets indicate that they consist of high-MgO primitive lavas with incompatible element-depleted NMORB trace element signatures [*Finney*, 1989; *Smith et al.*, 1994].

Formation of Near-ridge Seamounts and Implications for Geochemistry

The structural and geochemical data collected from many near-ridge seamounts has lead many authors to hypothesize about the formation of these near-ridge seamounts and seamount chains. Several hypotheses have been proposed: (1) they are the result of small thermal

anomalies (or "minihotspots") that preferentially melt in advance of a migrating ridge system [*Desonie and Duncan,* 1990], (2) melting of low-temperature, enriched heterogeneities occur in advance of a migrating ridge crest [*Davis and Karsten,* 1986], and (3) fracture zones and transforms may act as conduits from below ridge magma chambers, supplying magma to the off-axis seamounts [*Sleep,* 1984]. The geochemistry found at near-ridge seamounts will thus be dependent upon how the seamount formed.

The structure of the mantle which the seamounts are tapping also has implications for the geochemistry observed. *Cousens* [1996a] and others before him [*Batiza and Vanko,* 1984; *Zindler et al.,* 1984] proposed the "plum-pudding" or "veined" model for the upper mantle in the Northeast Pacific. They suggest that the mantle consists of a *depleted* peridotite matrix with imbedded veins (or plums) of *enriched* lherzolite/clinopyroxenite. Various degrees of melting, fractionation, and mixing of these two different types of sources can produce a variety of melts. Incompatible element concentrations will be high in lavas that are produced from the initial melting of a mantle that contains enriched veins. As the extent of melting increases, the lava compositions will reflect the further melting of the enriched component, and if melting proceeds far enough, the depleted component. This also has consequences for the isotopic ratios observed at these near-ridge seamounts because it is assumed that the enriched component also has a radiogenic isotopic composition characteristic of an enriched mantle source (more radiogenic $^{87}Sr/^{86}Sr$ and $^{206}Pb/^{204}Pb$ and less radiogenic $^{143}Nd/^{144}Nd$). While the degree of partial melting and subsequent fractional crystallization does not directly affect radiogenic isotope ratios, magma mixing can obscure them. Distinct isotopic ratios can therefore be observed in lavas that result from melts of different veins in the mantle.

As discussed above, it is likely that near-ridge seamount lavas do not reside in magma chambers for extended periods of time. Thus, the extent of differentiation and magma mixing will be small, allowing for melts to essentially rise directly from the mantle and erupt on the seafloor [*Clague et al.,* 2000]. Melts in sub-axial magma chambers often are produced from various degrees of partial melting, experience extensive fractionation, and undergo varying degrees of mixing with many different components. Because near-ridge seamounts have different plumbing systems than the near-by ridge axis, the seamounts may be able to better reveal the degree of heterogeneity in the upper mantle and provide insight into how they form better than the ridge axis. This study will explore the role of shallow level processes such as fractionation, mixing, and varying degrees of partial melting as well as mantle source material using geochemical analysis of major and minor element compositions, trace elements, and isotopic ratios.

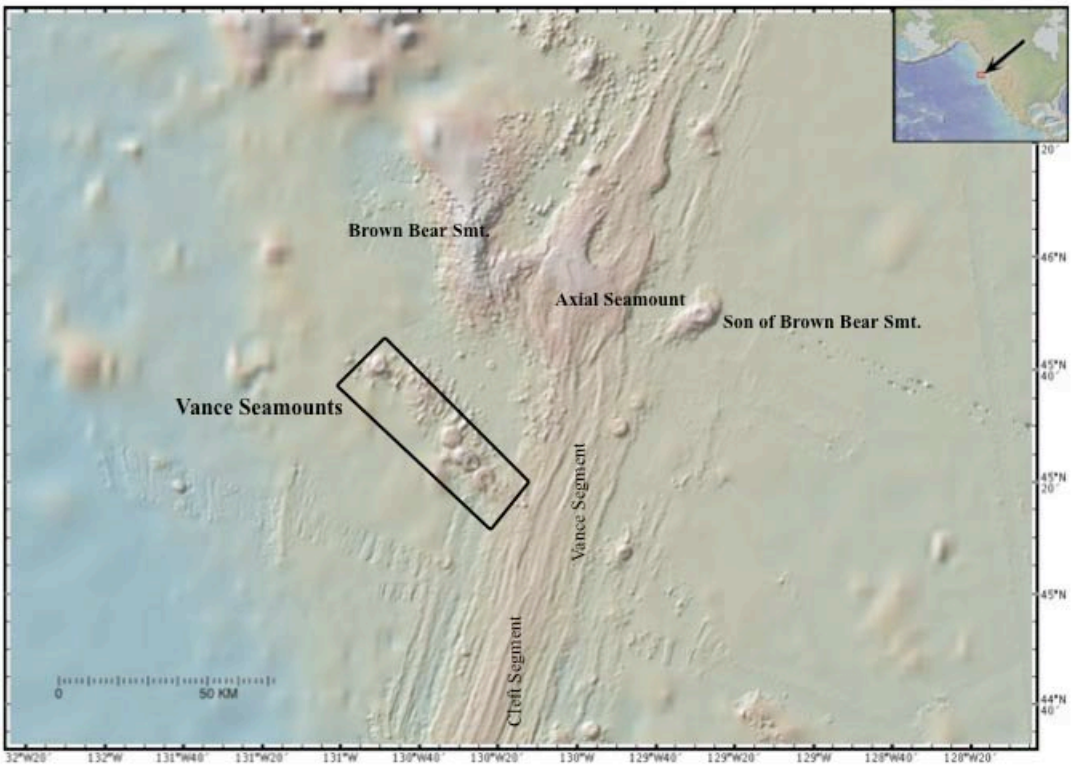

Figure 2-1. Bathymetric map of the southern Juan de Fuca Ridge (JdFR), located 600 km off the coast of the northwestern United States. The Vance Seamounts (as outlined) are located at 45° 15'N and 130° 20'W, near the overlapping spreading center of the Cleft and Vance Segments of the southern JdFR. Map created using the open source java application at www.geomapapp.org.

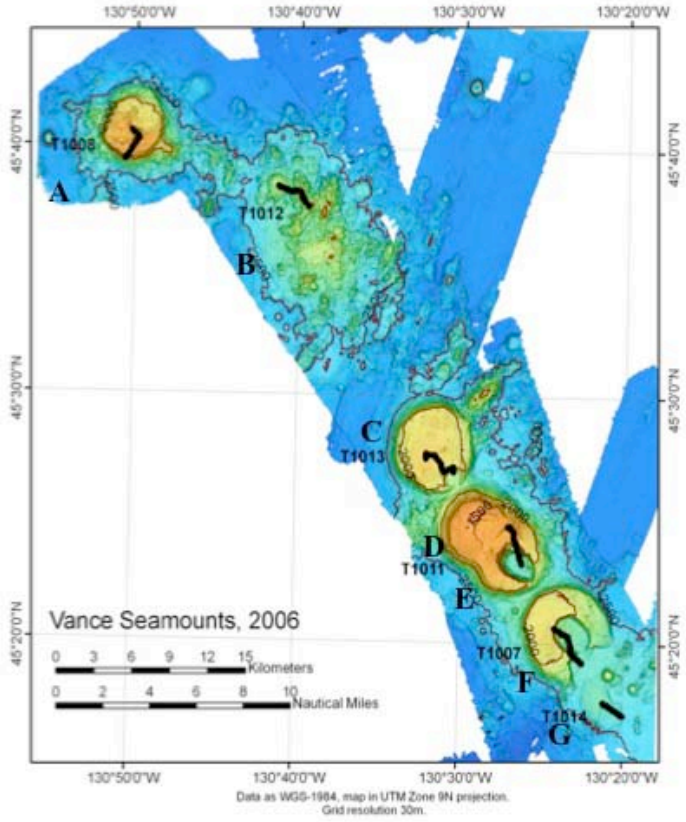

Figure 2-2. Bathymetric map of Vance Seamount Chain, with seamount names created from EM300 Multibeam data [*Clague et al.*, 2000]. Resolution is 30 meters and warmer colors indicate higher elevations from the seafloor. Contours are 500 meters. Dive tracks as performed by the *ROV Tiburon* in 2006 are indicated by the solid black lines (image created by J. Paduan, MBARI).

CHAPTER 3
FIELD STUDIES: VANCE EXPEDITION

During the Vance Expedition from July 30 to August 5, 2006, a detailed study of the Vance Seamount Chain was completed aboard the *R/V Western Flyer* (Figure 3-1) when six dives were conducted using the remotely operated vehicle (*ROV) Tiburon* (Figure 3-2), both owned and operated by the Monterey Bay Aquarium Research Institute (MBARI). The expedition also included sampling and collecting video footage and sediment from Axial Seamount; a large on-axis volcano north of the Vance Chain. The location of the *ROV Tiburon* dives were planned based on bathymetric features seen in high-resolution swath bathymetry and side-scan images previously collected by D. Clague [*Clague et al.* 2000] using a hull-mounted 30-kHz Simrad EM300. Simultaneous observations made by the scientists, high-definition digital still and video images, and sample locations were located with respect to the EM300 base bathymetry using a real-time ArcView navigation and GIS system during the cruise. The bathymetric data, ship location, and ROV navigation used a common GPS data-stream with real time depth (from the ROV), which provided position information accurate to within 10-20 m of the EM300 bathymetry.

The locations of the dive tracks were directed towards studying and sampling the caldera floors and walls. A variety of sample types were collected using the manipulators of the *Tiburon*, including lava samples, sediments, volcaniclastics, and biological samples using push cores, scoop bags and vibra-cores. Each sample was photographed in place on the seafloor and after recovery, aboard the ship. In total 103 lava samples and 37 volcaniclastite samples were collected for study. Previously, only a limited number of samples had been recovered from the Vance Seamounts, all of which were imprecisely located dredge samples taken from the cones nearest to the ridge (Vance G, F, and C). Only a small subset of these samples has been

geochemically or petrographically analyzed [*Finney*, 1989; *Smith et al.*, 1994]. Rock samples collected by the *ROV Tiburon* were limited to what the manipulator arm could break from the outcrop, but a variety of lava morphologies were collected where possible. Sampling location was chosen based geologic setting and change in lava morphology. As many as 30 precisely located rock samples were collected per dive, allowing for adequate spatial and some temporal range. Below, a short summary of each dive and the findings is provided. More information including logbook entries and detailed equipment descriptions can be found at http://www.mbari.org/expeditions/vance.

Dive T1007- Vance F, July 29, 2006

The dive (Figure 3-3) began on the relatively young-looking southernmost caldera floor and proceeded northwest toward the caldera wall separating the younger caldera from the central (older) caldera. The ROV encountered lava flows that erupted within the caldera, draping ridge-parallel faults. The caldera wall was comprised of a large talus slope for much of its height, then graded into interbedded, truncated pillow and massive flows in the upper section (Figure 3-4 and 3-5). The caldera wall was capped by a thin layer of fine-grained volcaniclastite (Figure 3-6). The *Tiburon* then dropped into the central caldera floor, which was covered by rippled pelagic sediment. As the ROV traversed the caldera floor, it encountered small outcrops of post-caldera lava flows and exposures of volcaniclastite. Near the northwest caldera wall, there was a hummocky deposit composed of constructional volcanics, indicating the presence of effusive eruptions after the caldera(s) collapsed. The dive ended with one more traverse up the northwestern caldera wall toward the flat-topped summit. The same sequence of morphologies was observed (talus slope, interbedded pillow and massive flows, capped by volcaniclastics).

Dive T1008, Vance A: July 30, 2006

Vance A is the oldest volcanic cone of the chain and bathymetric imaging indicated that there was no large caldera feature, which was confirmed by the observations made from the dive. The *Tiburon* landed on the flanks of the volcano, characterized by steep slopes of talus and continued northeast to the nearly flat summit of the volcano (Figure 3-7). Small volcanic shields (Figure 3-8), ridge-parallel faults, and a thin layer of volcaniclastite marked the summit. There was also abundant sediment cover, which consisted of sand and gravel size lava fragments (as opposed to the pelagic sediment found in the calderas of Vance F). Thick coatings of manganese oxide on the outcrops made sample description and collection extremely difficult. While traversing the summit to the northeast, the ROV encountered a small outcrop of highly altered hydrothermal sulfide, one of the oldest such deposits to be found on the seafloor. A variety of flow morphologies were observed including pillow lavas, lobate flows, sheet flows, and massive flows (Figure 3-9 and 3-10).

Dive T1011, Vance E: August 2, 2006

Vance E is the second youngest volcanic cone in the chain and is part of a very complex structure resulting from two large volcanic cones (Vance D and E) that have coalesced. The dive (Figure 3-11) focused on the younger shield (Vance E) and its three nested calderas. The dive began in the southeast caldera at ~2320 meters below sea level and continued toward the caldera wall to the northwest. Small pillow lavas outcropped through pelagic sediment on the caldera floor. The base of the caldera wall consisted of a long slope of talus blocks and then abruptly gave way to near vertical wall of interbedded massive and pillow lava units, many of them truncated (Figure 3-12). Columnar jointing (Figure 3-13) was observed in a nearly 30 m thick section of massive flow as well as in many other massive flow units. The caldera wall was capped by a 2 meter thick section of layered fine-grained volcaniclastite (Figure 3-14 and 3-15).

The dive continued on the floor of the middle caldera, which was covered by pelagic sediment (Figure 3-16). The northwest wall of this caldera had similar morphology to the wall that was observed in the southeast, suggesting that it may not be a separate caldera, but a section of the youngest (southeastern) caldera that did not subside completely. The ROV continued northwest across the floor of the older (northwestern) caldera and observed unbroken pillow lavas covered by volcaniclastite. This observation suggests that the caldera may have collapsed in a cylinder-like fashion, leaving the uppermost sections of lava in tact. The caldera wall to the northwest was an indistinguishable (due to thick Mn-oxide coatings) mix of talus, ponded lava flows and/or dikes, and pillow flows in the upper units. Coarse-grained volcaniclastite capped the rim of the caldera.

Dive T1012, Vance B: August 3, 2006

Vance B is one of two seamounts in the chain that is not a discrete volcanic cone, but a large area of disorganized volcanic constructs including ridges and small cones. The dive traverse (Figure 3-11) crossed one of the largest features, a cone that is 2 kilometers across. The observed lava morphologies included only pillow lavas and talus, but there were abundant pillow mounds present during the entire dive traverse (Figure 3-18 to 3-20). The lack of sheet or lobate flows suggests that eruption rates in this area were low. Volcaniclastite was also not observed, indicating that it was not produced in this area and perhaps these small vents did not experience explosive eruptions. The eruptive vents had steep sides with talus at their base and much of this talus was draped by elongate pillow flows.

Dive T1013, Vance C: August 4, 2006

The dive began on the southeast caldera floor and continued northwest up the caldera wall (Figure 3-21). The caldera wall was dominated by talus at the base, massive flows, and pillow flows in the upper section. Identification and sampling of the lavas was again difficult because of

the extremely thick Mn-oxide coatings. Volcaniclastite draped both the lava flows and the rim of the caldera. Sheet flows and sediments were observed on the upper caldera floor (Figure 3-22) and this caldera's wall was also composed of talus and massive flows. The summit of the volcano consisted of small areas of constructional pillow ridges (Figure 3-23).

Dive T1014, Vance G: August 5, 2005

Vance G consists of a broad shield with no evidence of collapse or caldera structures. The dive began to the southeast of the shield and the ROV crossed young ridges of sheet flows and pillow lavas (Figure 3-24 and 3-25). The dive continued northwest across two large normal faults parallel to the JdFR and multiple small fractures, which have resulted in a downdropping of the southeastern side of the shield. The relatively younger flows graded into older, sediment covered volcaniclastite and protruding pillow lavas (Figure 3-26). Gentle slopes were expected based on the bathymetric imaging, but instead there were large fault scarps that exposed interbedded pillow and sheet flows with talus at the base of the scarps.

Summary of Dive Observations

Eruptive products include pillow lavas, sheet flows, massive flows, and volcaniclastites. Caldera floors consist of flat-lying volcaniclastite (presumably related to caldera collapse) with overlying pelagic sediment. In some areas, post-caldera pillow lavas protrude through the sediment, indicating volcanic activity after caldera formation. Caldera walls consist of truncated, interbedded massive flows sheet flows and pillow basalts, with talus accumulated at the base. The presence of thick sections of massive flows in the caldera walls supports the hypothesis proposed by *Clague et al.* [2000] that many of the caldera collapse structures had been filled/ partially filled by lava ponds after caldera formation. Volcaniclastic samples and sediment samples not only contained angular volcanic glass fragments, but also "limo o Pele" (bubble wall fragments) which may indicate submarine pyroclastic eruptions during caldera collapse. The

lavas recovered were encrusted with variable iron-manganese coatings, precipitated over time from the surrounding seawater and also from warm hydrothermal fluids that were released during caldera collapse. Mn-oxides coatings were very thick and prolific on the seamounts located farther from the ridge and sediment cover was also thick on these older volcanic cones. A large variety of samples were recovered, consisting of mostly parts of pillow lavas, but also ample numbers of sheet flows and massive flows, along with volcaniclastic samples.

Overall, the dives on Vance C, E, and F revealed similarities in the nature of the calderas, eruptive products, and structures between these seamounts. Vance A was distinct in that there are no collapse features observed on this volcanic cone and thus less is known about the stratigraphy of the volcanic construct, which is more observable on the other cones due to their collapsed caldera structures. Features observed on Vance B revealed much more complexity in the outcroppings than expected based on bathymetry, with abundant constructional features, such as pillow ridges, every few meters. The features observed on Vance G were also unexpected given the bathymetry. There were numerous small faults along with the large ridge parallel faults indicated by the bathymetric data, due to the formation of this seamount in the active, near-ridge environment. Young lavas flows were expected on this dive, due to its proximity to the ridge and the hypothesis that it may still be active. While there were young-looking lavas in the southeastern part of the seamount, older (sediment covered, hydrothermal Mn oxide coated) lavas were observed as the dive progressed. The morphology of this seamount was not similar to that of Vance B (abundant, steep pillow ridges and mounds) as was previously indicated by the bathymetry, instead having more fluid sheet flows with some small protruding lava pillows. Geochemical analysis of the precisely located samples may help reveal a geochemical control on the nature of the differences between the morphologies of the seamounts.

Figure 3-1. The *R/V Western Flyer*, a 117 ft. small water-plane twin hull (SWATH) oceanographic research vessel operated by the Monterrey Bay Research Aquarium Institute (photo courtesy MBARI).

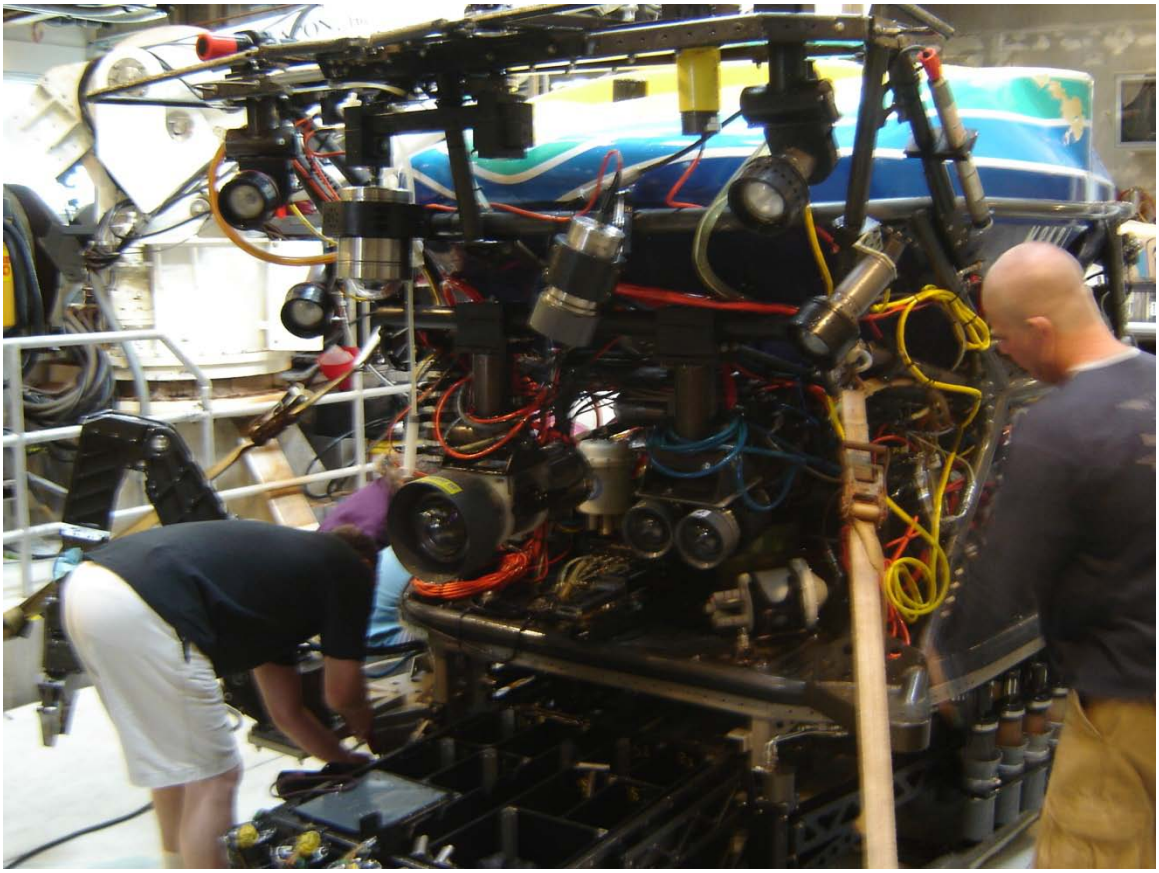

Figure 3-2. The *ROV Tiburon*, a remotely operated vehicle owned and operated by MBARI. Front view, with high definition cameras, sampling arm, and sample drawer shown.

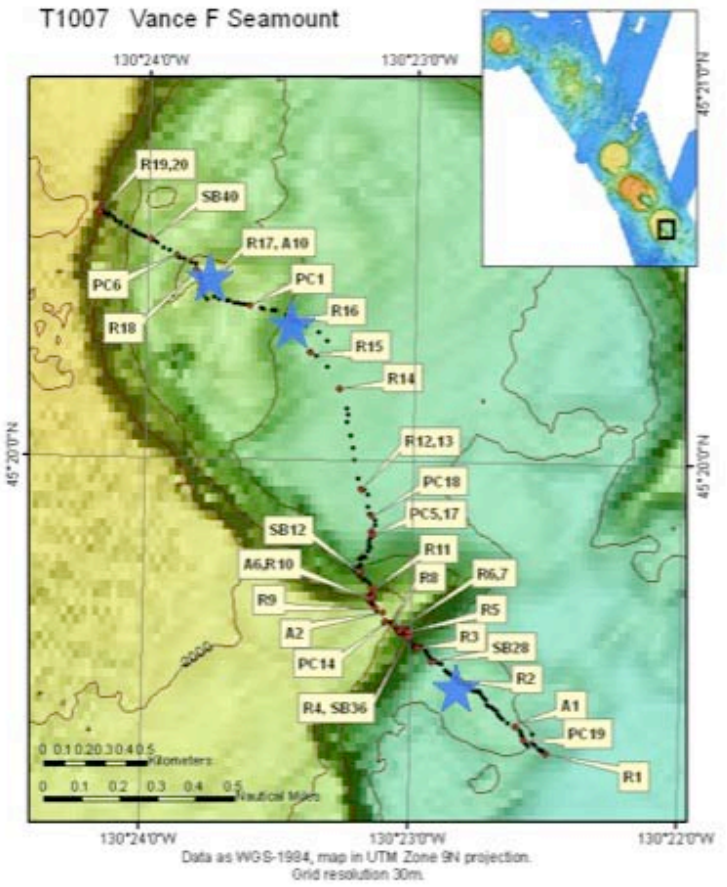

Figure 3-3. Bathymetric map of Vance F with dive track (T1007). Red dots indicate sampling locations; R=rock sample, PC/SB=sediment, A=biological. Blue stars indicate locations of samples used for trace element analysis (this study). Base map produced from EM300 data by MBARI mapping team [*Clague et al.*, 2000].

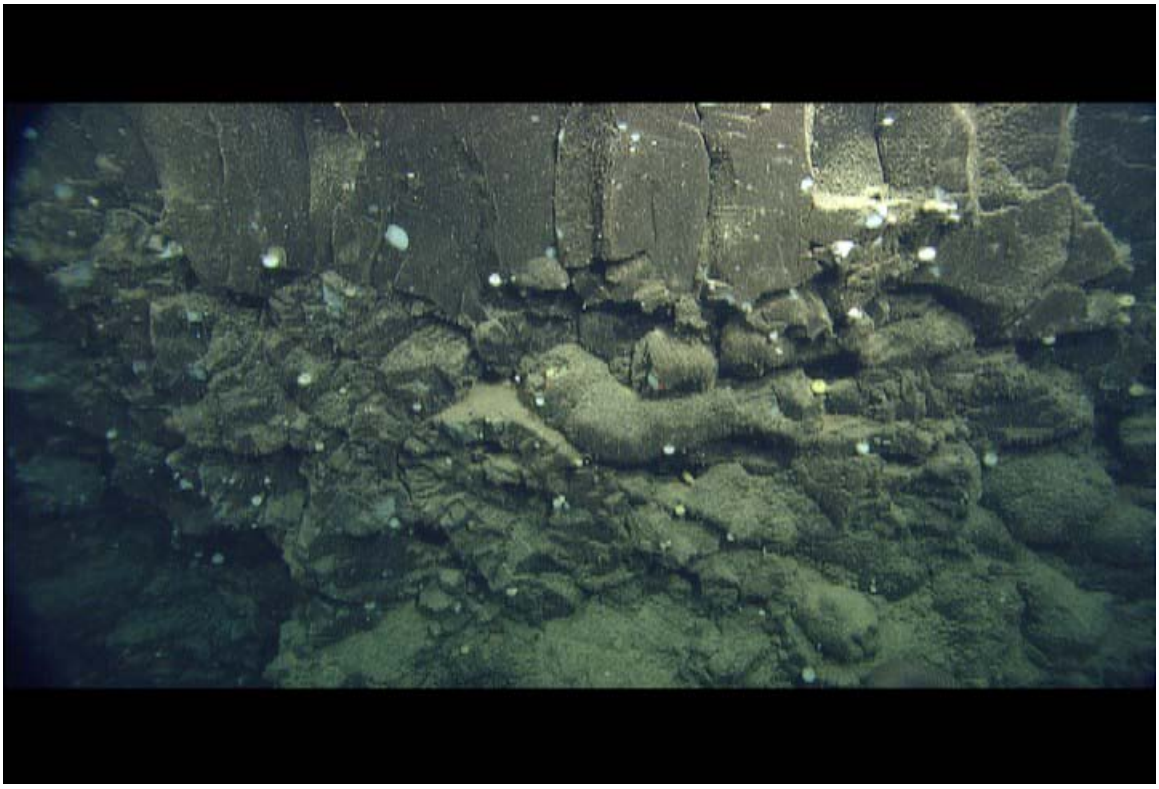

Figure 3-4. Interbedded pillow lavas and massive lavas in the caldera walls of Vance F.

Figure 3-5. Sample T1007-R19, an example of a massive flow collected near the top of the caldera wall on Vance F.

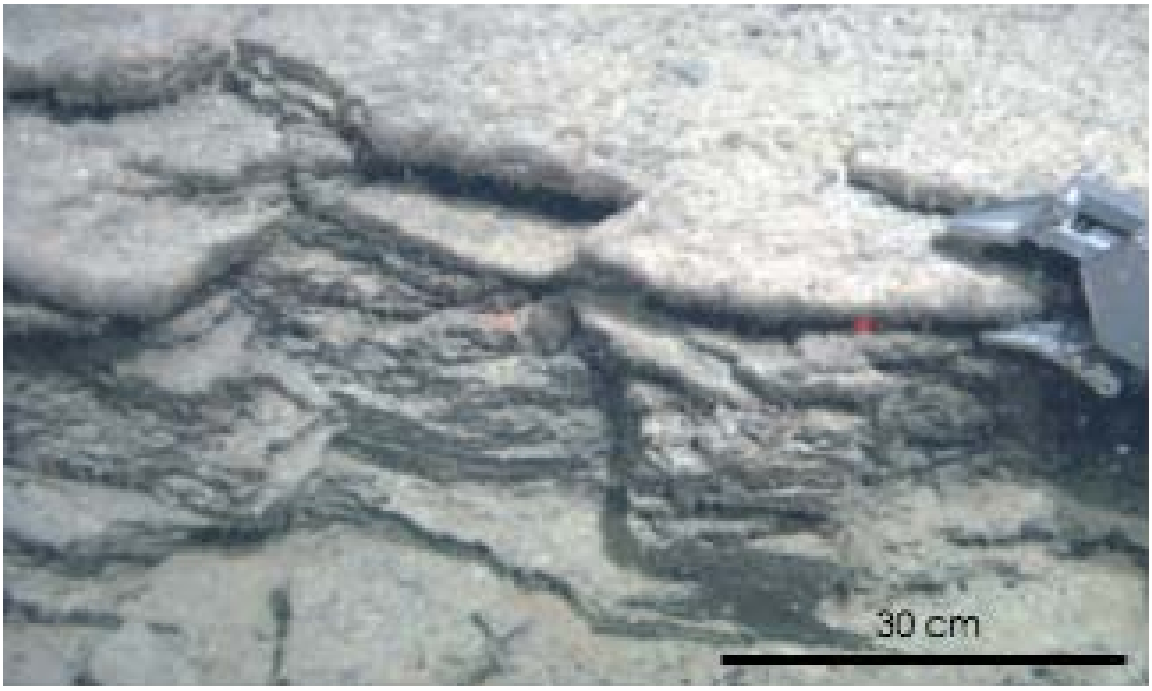

Figure 3-6. *ROV Tiburon* sampling bedded volcaniclastite on Vance F.

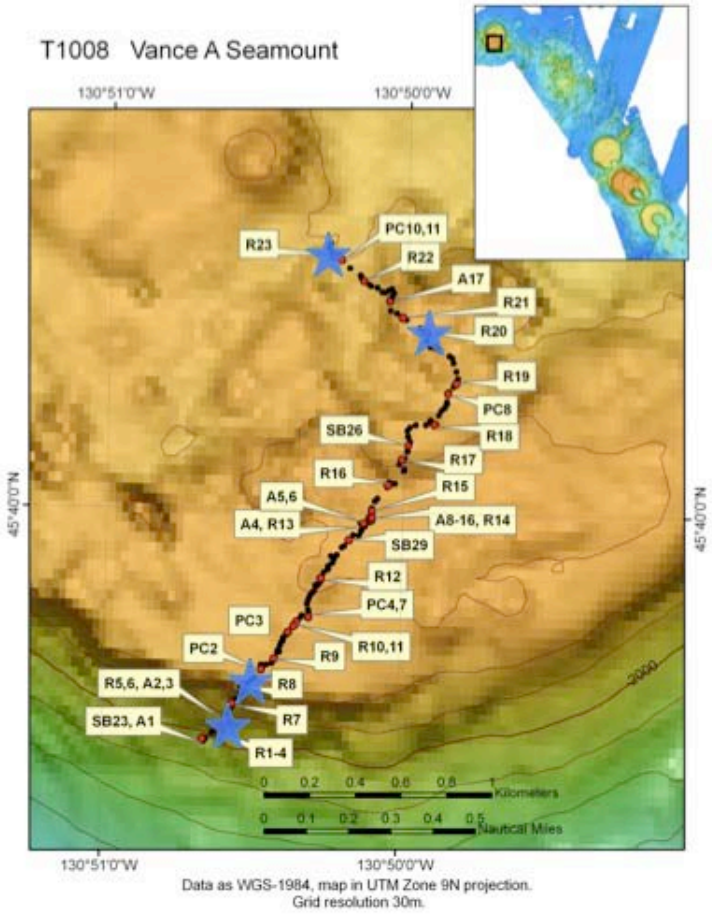

Figure 3-7. Bathymetric map of Vance A with dive track (T1008). Red dots indicate sampling locations; R=rock sample, PC/SB=sediment, A=biological. Blue stars indicate locations of samples used for trace element analysis (this study). Base map produced from EM300 data by MBARI mapping team [*Clague et al.*, 2000].

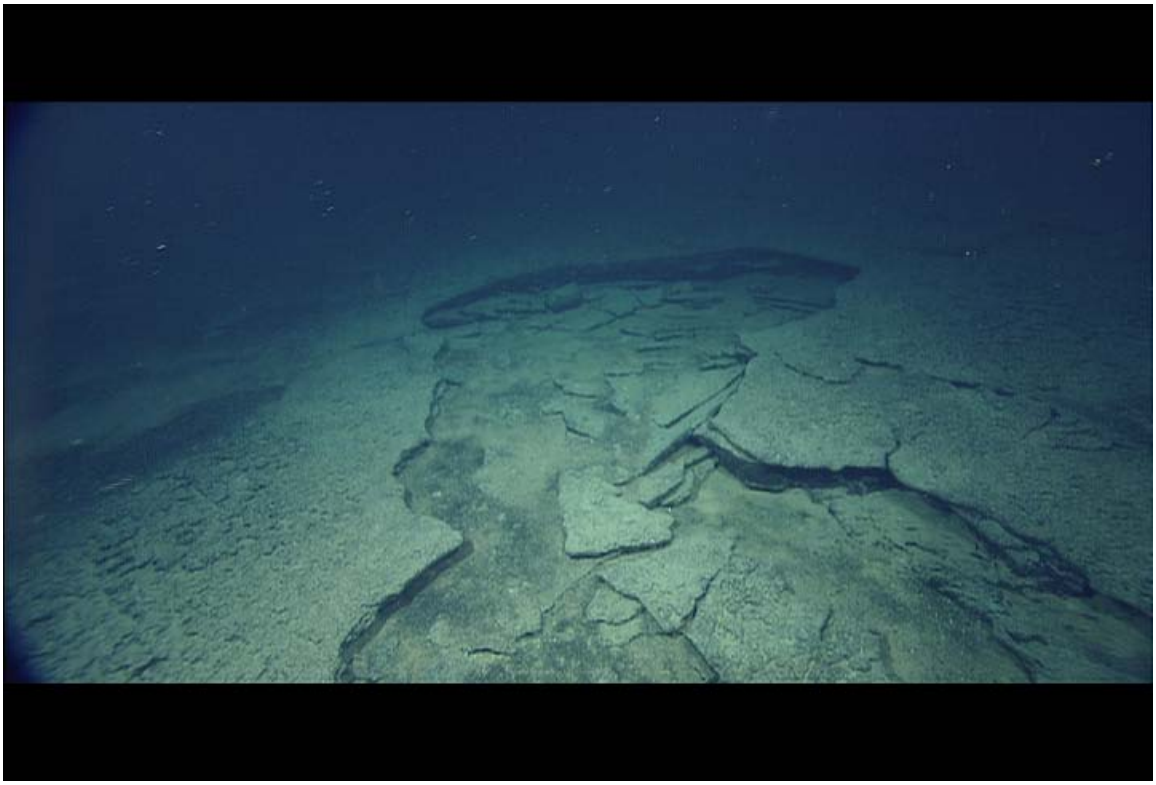

Figure 3-8. Sheet flows on the summit of Vance A.

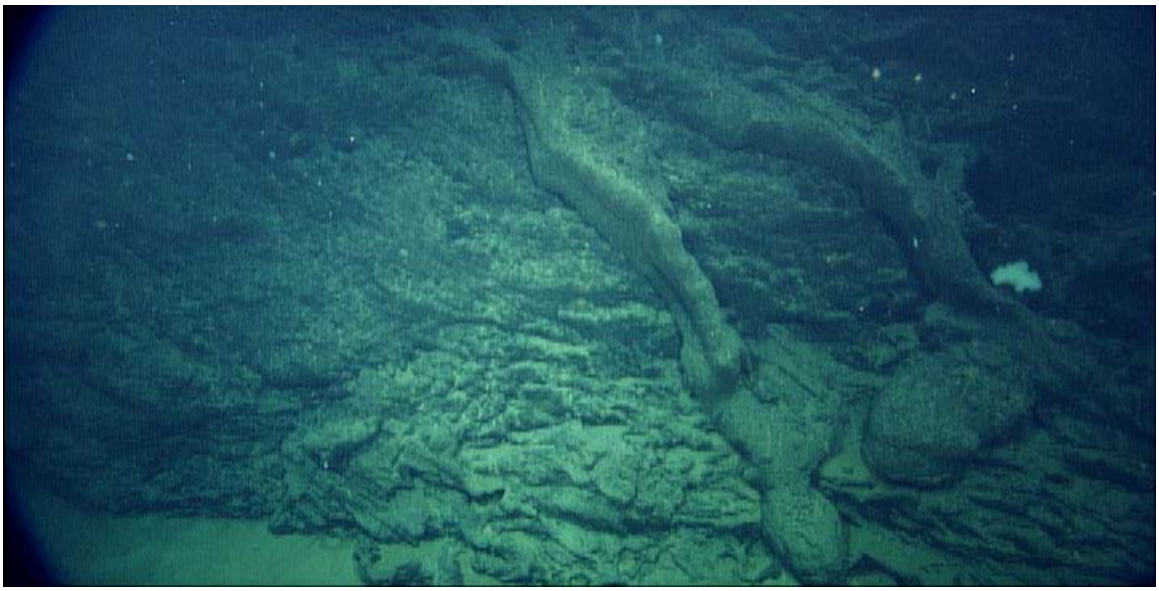

Figure 3-9. Elongated pillow lavas draping jumbled sheet flows on Vance A.

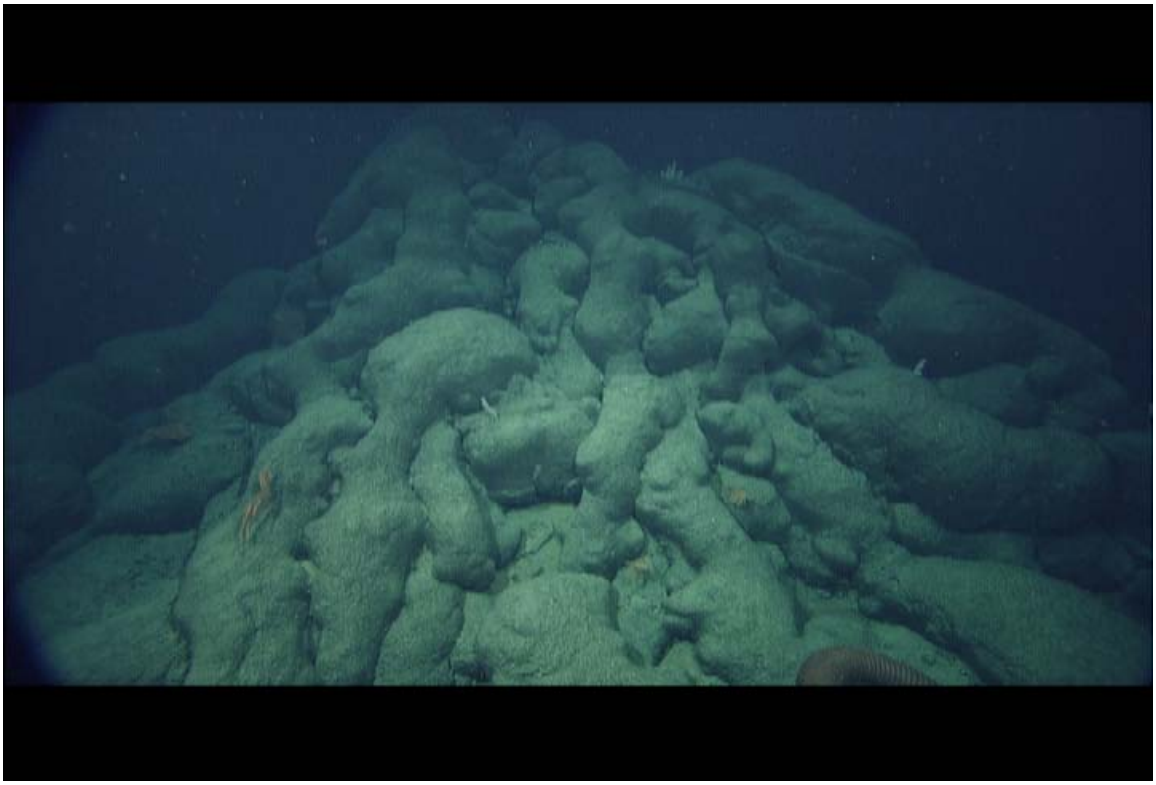

Figure 3-10. Elongate pillow lavas draping a small mound on Vance A.

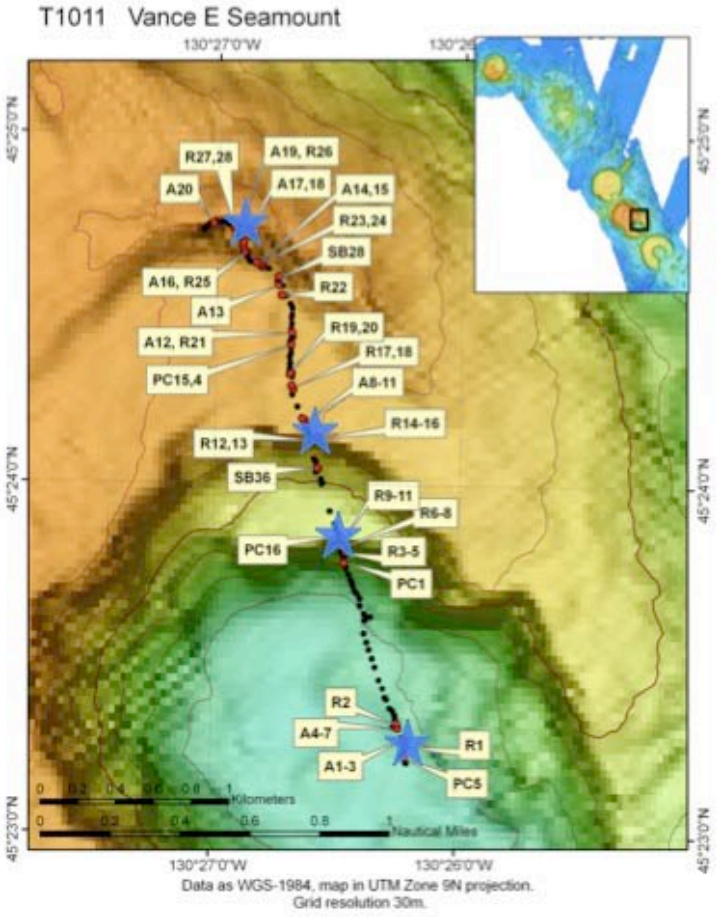

Figure 3-11. Bathymetric map of Vance E with dive track (T1011). Red dots indicate sampling locations; R=rock sample, PC/SB=sediment, A=biological. Blue stars indicate locations of samples used for trace element analysis (this study). Base map produced from EM300 data by MBARI mapping team [*Clague et al.*, 2000].

Figure 3-12. Truncated pillow flows in the caldera wall of Vance E.

Figure 3-13. Columnar jointing of a massive flow (or lava lake?) on top of ropey sheet flows. A common unit found along the caldera walls of Vance E.

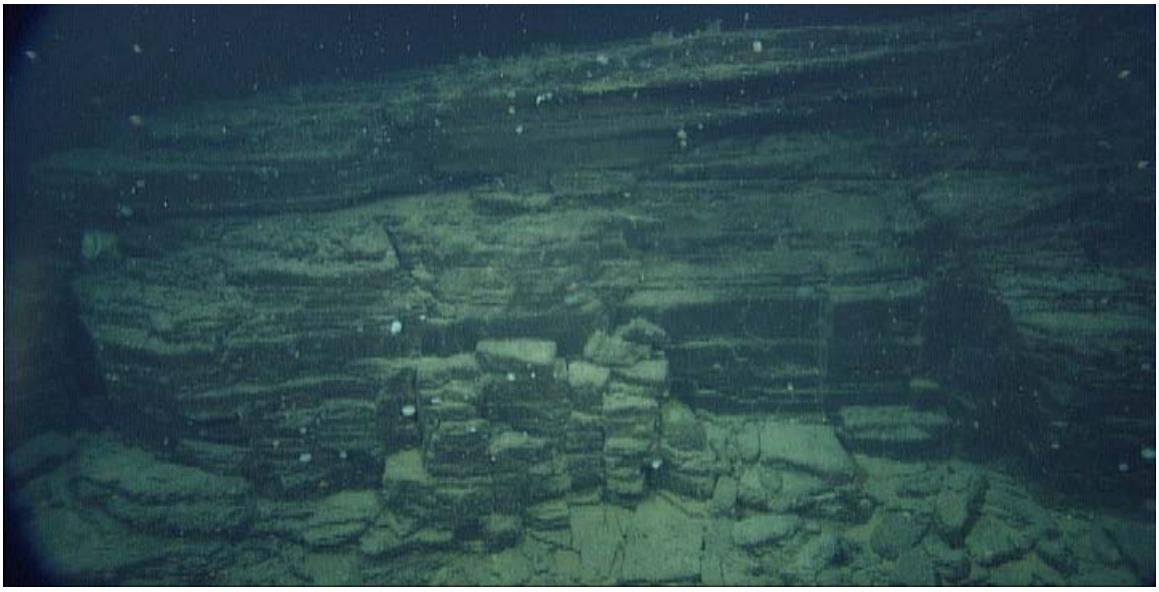

Figure 3-14. Thick sections of bedded volcaniclastite that forms the top unit of the caldera walls on Vance E.

Figure 3-15. Sample T1011-R8, cross-section of a layered volcaniclastite.

Figure 3-16. Rippled sediment that typically covered the caldera floors on the Vance Seamounts, this photo taken from Vance E.

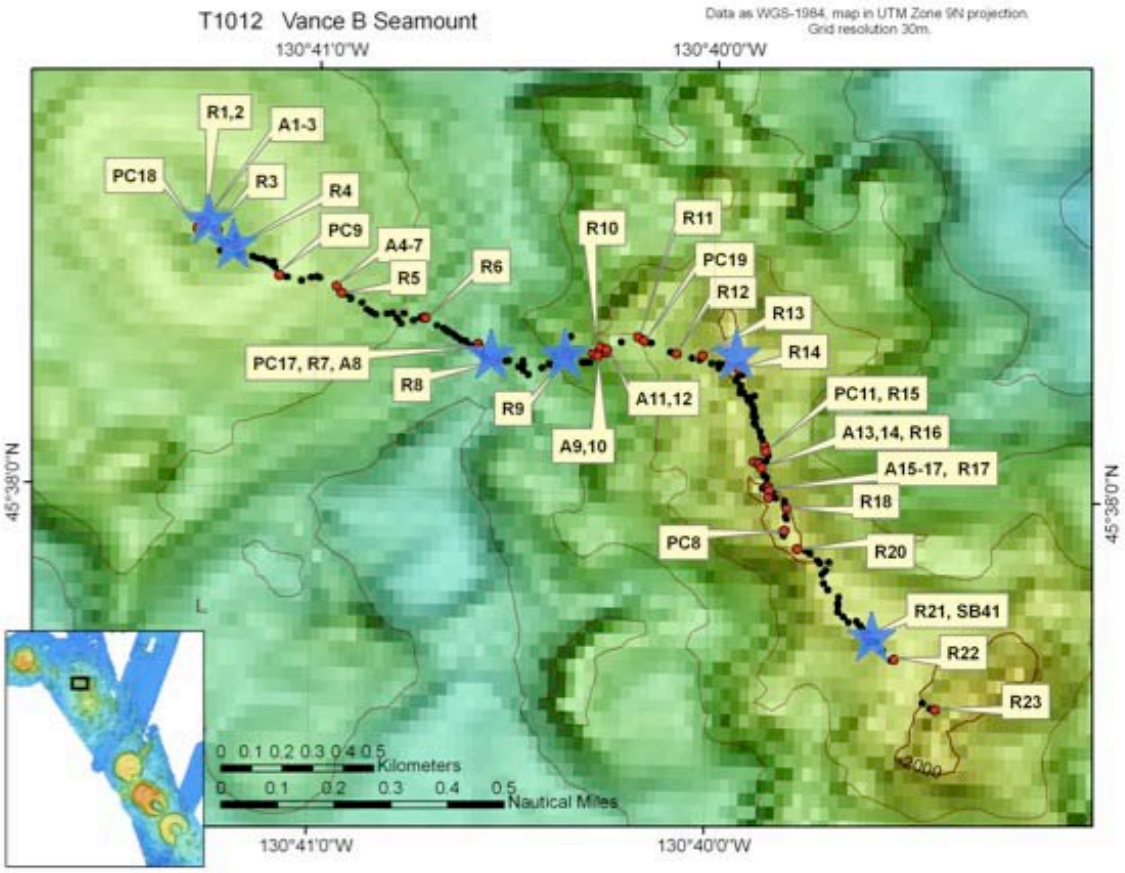

Figure 3-17. Bathymetric map of Vance B with dive track (T1012). Red dots indicate sampling locations; R=rock sample, PC/SB=sediment, A=biological. Blue stars indicate locations of samples used for trace element analysis (this study). Base map produced from EM300 data by MBARI mapping team [*Clague et al.*, 2000].

Figure 3-18. Burst pillow lava along the steep flanks of a pillow mound on Vance B.

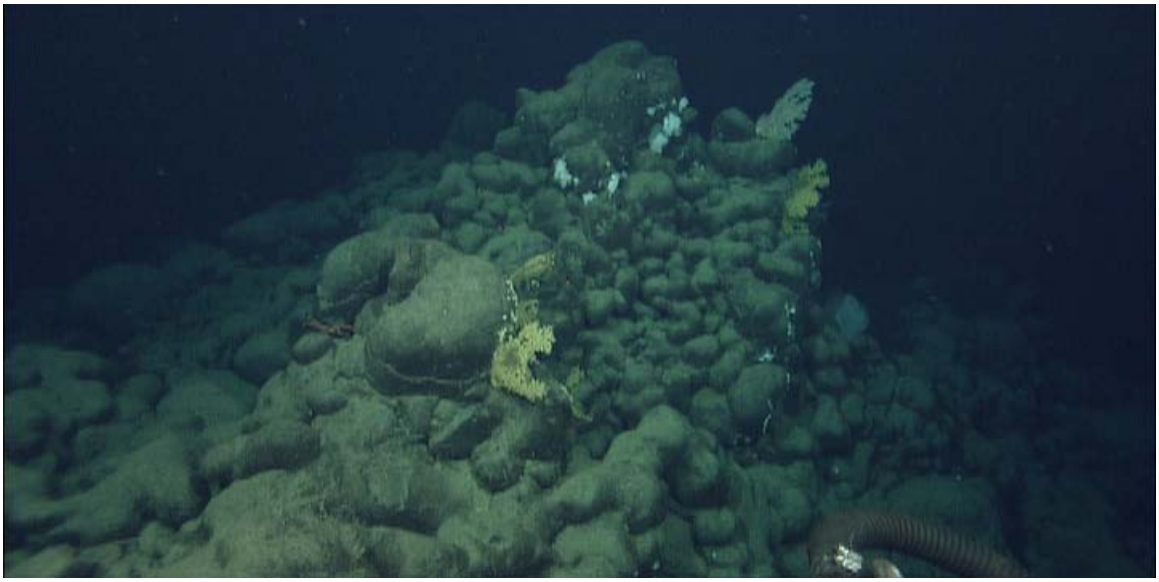

Figure 3-19. Steep pillow mound (or haystack) characteristic of Vance B.

Figure 3-20. Sample T1012-R8, a pillow bud sample with abundant glass (dark, shiny black material) and a Mn-oxide crust.

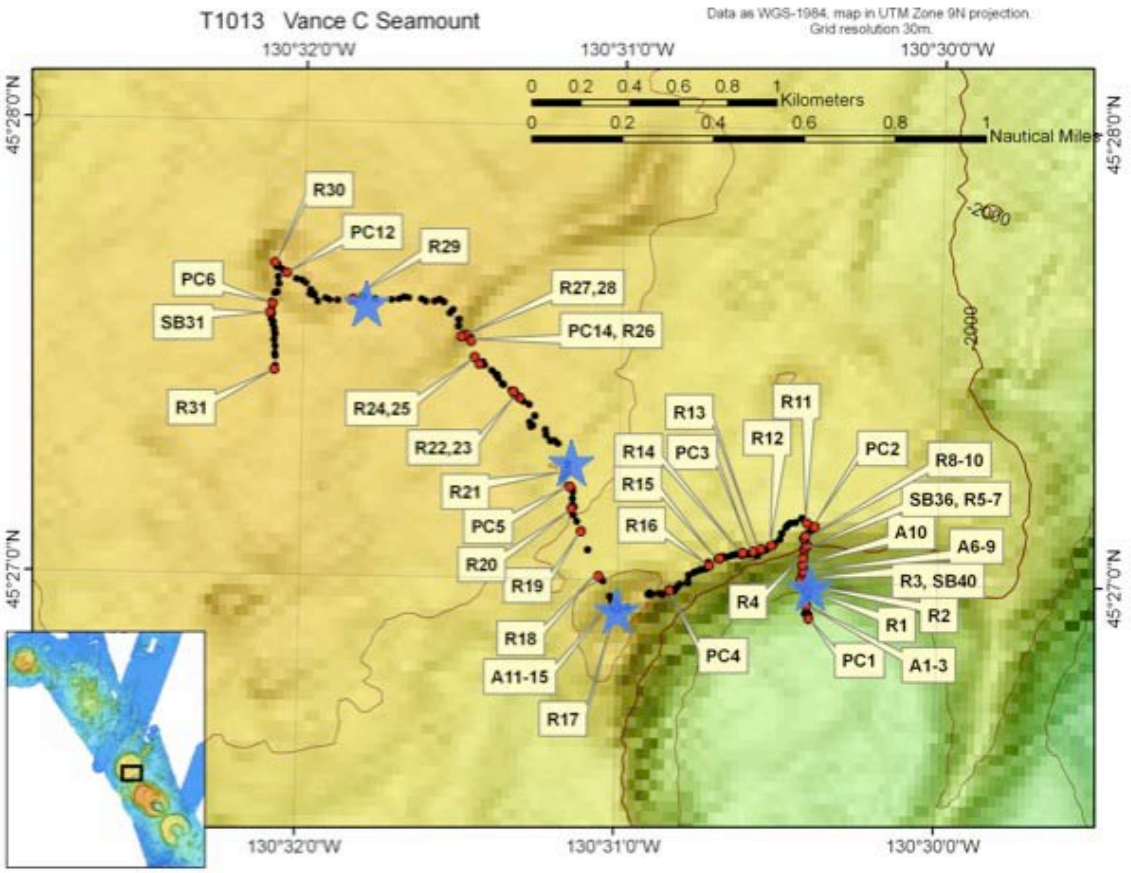

Figure 3-21. Bathymetric map of Vance C with dive track (T1013). Red dots indicate sampling locations; R=rock sample, PC/SB=sediment, A=biological. Blue stars indicate locations of samples used for trace element analysis (this study). Base map produced from EM300 data by MBARI mapping team [*Clague et al.*, 2000].

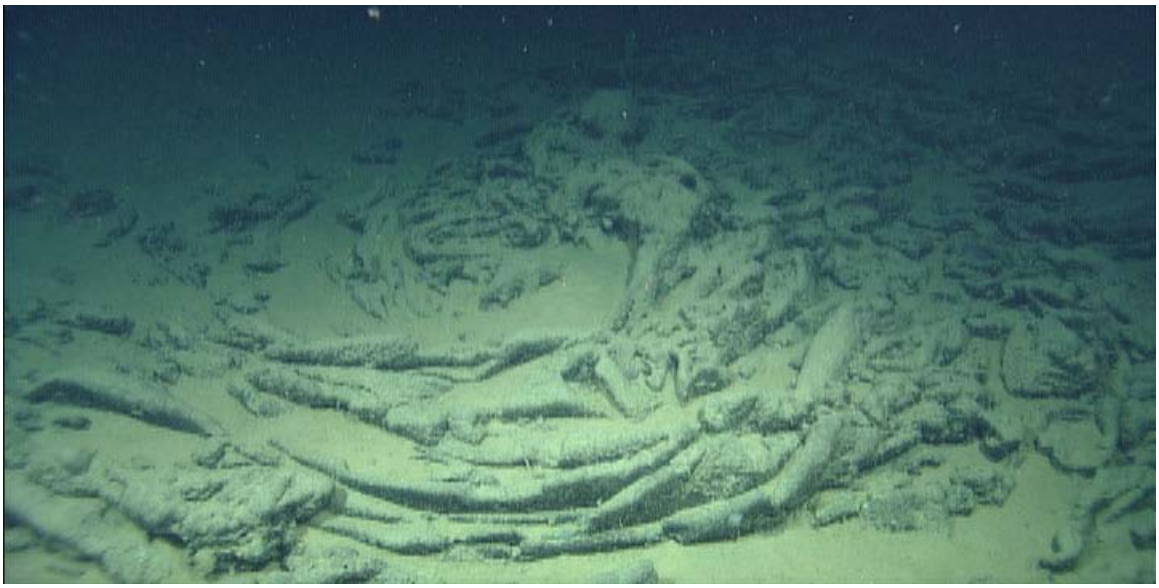

Figure 3-22. Ropey sheet flow covered with sediment on the caldera floor of Vance C.

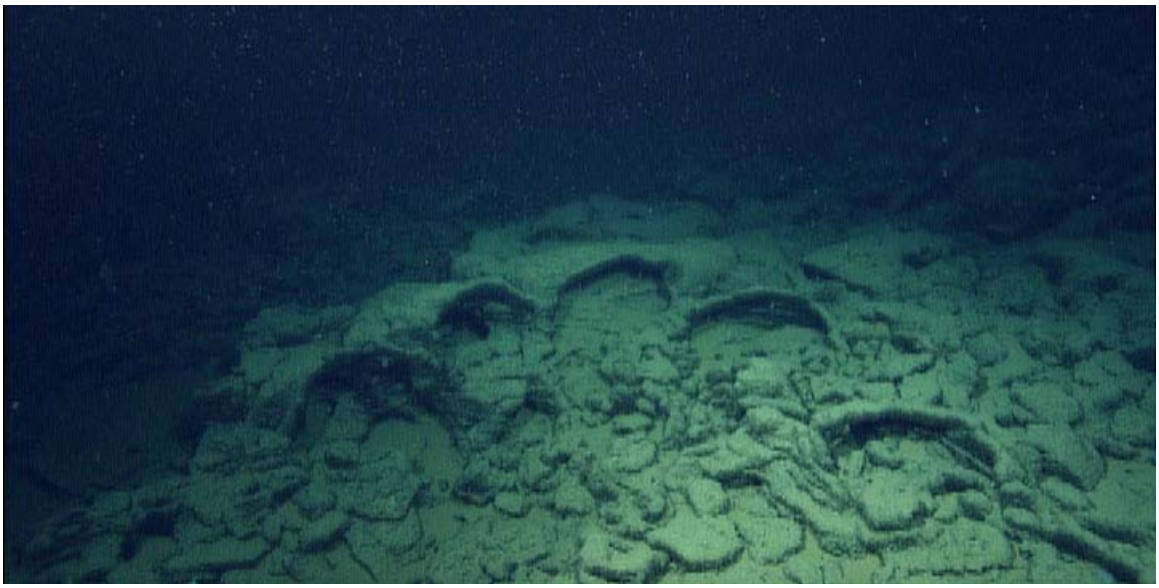

Figure 3-23. Pillow lavas that have collapsed due to lava drain-back; part of a constructional mound on the summit of Vance C.

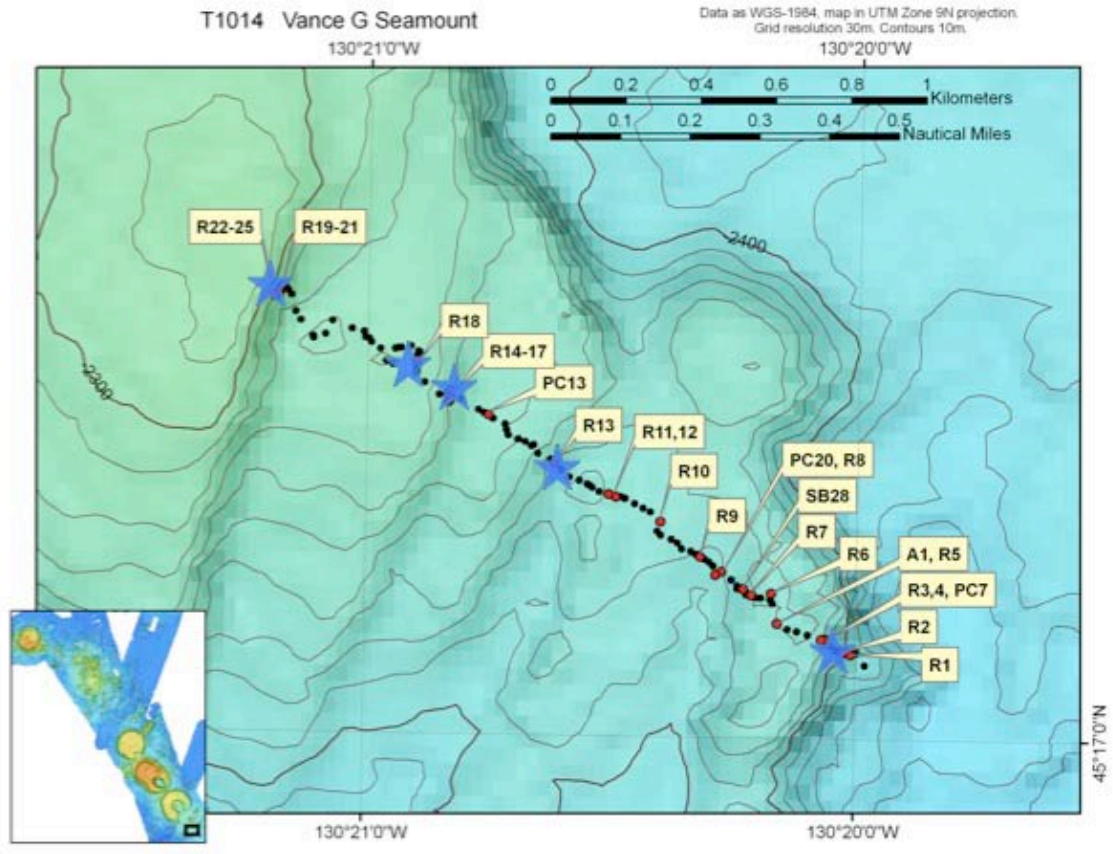

Figure 3-24. Bathymetric map of Vance G with dive track (T1014). Red dots indicate sampling locations; R=rock sample, PC/SB=sediment, A=biological. Blue stars indicate locations of samples used for trace element analysis (this study). Base map produced from EM300 data by MBARI mapping team [*Clague et al.*, 2000].

Figure 3-25. Sample T1014-R23, part of a folded sheet flow viewed from above with Mn-oxide coating.


Figure 3-26. Large pillow lava that is draped by volcaniclastic sediment on Vance G.

CHAPTER 4
ANALYTICAL METHODS

A total of 150 lava samples were collected from the Vance Seamount Chain using the *ROV Tiburon* during 6 dives during a research cruise on the *R/V Western Flyer* from July 30 to August 5, 2006. Glass from outer quenched rims were separated from the rock samples where possible during the cruise and distributed to the various institutions for individual analysis (Monterey Bay Aquarium Research Institute (MBARI), University of Florida, Carleton University, and McGill University). The sampled glass that was distributed was from the same glass fraction, to allow for direct comparison of the samples.

Major and Minor Elements

A total of 71 glass samples were analyzed for major element concentrations using a nine-channel ARL-SEMQ electron microprobe at the United States Geological Survey (USGS) in Menlo Park, by MBARI. The analytical precision for the major elements (except sodium) is ±1-2%. The precision for sodium is ±3-5%; for potassium and the other minor elements (P_2O_5, MnO) the precision is no better than ±10%. The methods used in these analyses are described in *Davis et al.* [1994] and a more detailed discussion of the standards used, precision, and accuracy is available in *Davis and Clague* [1987].

Trace Elements

A total of 49 samples from near-axis seamounts on the southern Juan de Fuca Ridge including the Vance Seamounts have been analyzed for their trace element contents. Nine clean powders of picked glass from the Vance Seamounts collected in 1988 and 1991 [*Finney*, 1988 and *Smith*, 1994] were selected for trace element analysis and twenty-nine samples collected in 2006 by the *ROV Tiburon* were selected based on their major element compositions. Samples were selected in an attempt to analyze as wide a range of compositions as possible. Eleven

additional samples were also chosen from other near-ridge seamounts along the Juan de Fuca Ridge that were collected during cruises in 1994 and 1995 (M. Perfit, personal communication). Glass samples were coarsely crushed and hand-picked using a binocular microscope. Phenocrysts and microlites were avoided, as were heavily MnO encrusted and altered glass chips. The picked samples were then cleaned ultrasonically for 5-7 minutes first in a solution made of a mixture of 100mL 30% H_2O_2, 80mL 2x distilled water, and 20mL 12.1 N reagent grade HCl, followed by three washes of 5 minutes each in 4x and 2x distilled water, in order to remove surficial coatings. After ensonification, the samples were dried under a heat lamp. Once dry, 50-60 mg of the cleanest glass chips from each sample were hand-picked using a binocular microscope for trace element analysis.

The samples were analyzed for trace elements at the University of Florida using an Element II Inductively Coupled Plasma Mass Spectrometer (ICP-MS). Dissolution and analytical procedures were developed by George Kamenov and a detailed description of these procedures can be found in Appendix A. Several certified rock standards (AGV-1, BHVO-1, BCR-2, and BIR-1) as well as two internal MORB standards (2392-9 and ENDV) were used to calibrate the Element II. Repeated chemical analyses of 2392-9 during each run were used to evaluate and correct for instrument drift as well as evaluate and refine accuracy and precision of the measurements; a discussion of accuracy and precision can also be found in Appendix A.

A set of 23 whole rock samples was also chosen for trace element analysis. The samples chosen for whole rock analyses included rock samples that did not have sufficient (and in some cases were completely lacking) glassy rinds. The analyses were performed using a HP 4500+ ICP-MS at the GeoAnalytical Lab at Washington State University (values provided by D. Clague

(MBARI)). Detailed procedures, precision, and accuracy are available electronically at http://www.wsu.edu:8080/~geology.

Radiogenic Isotopes

Twenty-four representative samples were chosen for analysis of $^{87}Sr/^{86}Sr$, $^{143}Nd/^{144}Nd$, $^{208}Pb/^{204}Pb$, $^{207}Pb/^{204}Pb$, and $^{206}Pb/^{204}Pb$. The samples were separated using ion-exchange column chromatography and then run on a ThermoFinnigan Triton T1 thermal ionization mass spectrometer in static mode at Carleton University. Several rock standards were used to calibrate the mass spectrometer, including NIST SRM981, BCR-1, Eimer and Amend (E&A) $SrCO_3$, and the La Jolla standards. The analytical uncertainty is ±0.00002 for $^{87}Sr/^{86}Sr$, ±0.00002 for $^{143}Nd/^{144}Nd$, ±0.05 for $^{208}Pb/^{204}Pb$ and $^{207}Pb/^{204}Pb$, and ±0.01 for $^{206}Pb/^{204}Pb$. Detailed analytical procedures can be found in *Cornejo* [2008], which uses refined methods found in *Cousens* [1996b].

CHAPTER 5
GEOCHEMICAL RESULTS

Major and Minor Elements

General observations

Major element data along with sample location for the 71 volcanic glass samples chosen for analysis can are presented in Table B-1, in Appendix B. Major element data indicates that all Vance Seamount lavas analyzed are subalkaline MOR basalts that follow a tholeiitic iron-enrichment trend typical of MORB. Figure 5-1 shows major and minor element variation diagrams plotted versus MgO concentrations. General trends *within* each of the seamounts exhibit increasing TiO_2, FeO*, Na_2O, and K_2O with decreasing MgO and decreasing Al_2O_3 and CaO with decreasing MgO. These types of trends are consistent with at least small amounts of fractional crystallization that include plagioclase, olivine, and perhaps minor clinopyroxene as mineral phases (further discussion of fractional crystallization trends is presented in Chapter 6). It is evident that there are differences in the major element abundances between seamounts in the chain as well as significant elemental variations within individual seamounts. The lavas are in general primitive in nature, with MgO contents that range up to 9.5 weight % and have Mg# 56-70 with high Cr and Ni (546 ppm and 315 ppm, respectively). The average MgO content of the lavas is 7.89 wt. %, but overall they range from 6.9 to 9.5 wt. %. Most of the seamount lavas have low K_2O concentrations, typical of NMORB compositions, but some lavas from Vance A have elevated K_2O values that are typical of EMORB compositions. Distinct groupings of major/minor element compositions for individual seamounts are particularly evident in the Na_2O, CaO, and K_2O variation plots. These groupings will be discussed below along with observations in the major element trends for each seamount.

Individual Seamount Characteristics

Vance A samples have moderate amounts of SiO_2, Al_2O_3, CaO, and FeO*, high Na_2O, and very high K_2O, although the data are somewhat scattered. They span a modest range of MgO values (7.25-8.57 wt. %) and have the highest TiO_2 values for a given MgO value for all the seamounts. The K_2O values of 4 of the Vance A samples are typical of EMORB and are significantly greater than concentrations of the rest of the seamounts in the Vance chain. They represent some of the most enriched samples recovered from a near-ridge seamounts in general and are unusual for MORB from the southern Juan de Fuca in particular.

Samples from Vance B have MgO contents ranging from 7.30 to 9.13 wt. % and relatively low concentrations of SiO_2 and CaO and high concentrations of Na_2O, Al_2O_3, and FeO*. They typically plot as a distinct group as compared to the other seamount lavas. The lavas also have very low K_2O concentrations, similar to those of Vance C, E, and F.

Samples from Vance C have relatively high SiO_2 and CaO and low concentrations of Na_2O, Al_2O_3, FeO*, and TiO_2. In fact, they have the lowest TiO_2 values for a given MgO value for the entire chain. Vance C has some of the most primitive lavas recovered from the seamount chain, but also has the largest range in MgO values (7.34-9.45 wt. %). The concentrations of K_2O are similar to the those in lavas from Vance B and F.

Samples from Vance E have high SiO_2 and CaO and intermediate concentrations of the other oxides compared to other seamounts in the chain. Vance E lavas tend to follow the most clear crystal fractionation trends for the Vance Seamounts. The samples from Vance E include some of the most evolved lavas from the Vance chain (MgO as low as 6.92 wt. %).

The Vance F lavas compositions fall within the extremes of the Vance lavas. They are not distinct within the data set, but do include some of the more primitive lavas sampled (MgO to

9.34 wt. %). The samples from Vance F tend to plot in two distinct groups, but the number of samples analyzed for the seamount is low (6 samples), so this may be an artificial observation.

Lavas from Vance G form a relatively tight group in all of the variation diagrams. Samples from this seamount tend towards lower MgO concentrations, which are the most restricted for the chain (7.40-7.91 wt. %). The samples also have relatively high SiO_2 concentrations (SiO_2 50.22-50.88 wt. %), similar to those of Vance E.

Trace Elements

General Observations

Trace element data for the 49 glass samples analyzed for this thesis can be found in Table B-2, in Appendix B. Representative plots of trace element concentrations, including compatible and incompatible elements, versus MgO are presented in Figure 5-2. REE variation and mantle-normalized diagrams are presented in Figures 5-3 and 5-4. The incompatible trace elements indicate that most of the seamount lavas are NMORB, because of their strong relative depletion in large ion lithophile elements (LILE) and light rare earth elements (LREE) $[(La/Sm)_N < 1]$ relative to the heavy REE. As a whole, the compatible elements (e.g. Ni and Cr) in the Vance Seamount lavas show a decrease with decreasing MgO, while the incompatible elements (LILE, REEs, Y, Zr, Nb, Sr, Rb) show an increase with decreasing MgO. Some of these trends can presumably be related to minor degrees of fractional crystallization; a more detailed discussion of fractionation trends regarding trace elements is presented in Chapter 6. Although there is significant variation of trace element concentrations in the lavas from different seamounts in the Vance Chain, many of the samples from individual seamounts plot along a similar trend, with some scatter. However, 4 EMORB samples from the Vance A seamount, have higher incompatible element abundances that plot in separate fields from the other seamount lavas in many of the trace element plots. Distinct correlations between elements (such as the groupings

present within the major element trends) are not as evident in the trace element data. The trace elements show fairly linear trends on variation diagrams (e.g. Zr versus Y, La versus Ce; Figure 5-5). The incompatible element ratios of some of the seamount lavas (e.g. Zr/Y 1.69-3.86) are indicative of highly depleted compositions (Zr/Y< 2.5).

On the chondrite- and primitive mantle-normalized variation diagrams (Figures 5-3 and 5-4), the Vance lavas show strongly LREE depleted patterns and unfractionated (flat) middle and heavy rare earth element patterns. Vance A lavas have LREE patterns that are slightly depleted to slightly enriched, with $(La/Sm)_N$ ratios of 0.60 to 1.07. The other seamounts have lavas that are generally more LREE depleted with $(La/Sm)_N$ ratios of 0.35 to 0.68. The seamounts tend to plot in groups and show mostly parallel patterns within individual seamounts (which is consistent with fractional crystallization). There are samples from different seamounts that exhibit crossing REE patterns, which may indicate different degrees of partial melting of a single mantle source or mantle sources with different compositions that were involved in the genesis of parental magmas.

Individual Seamount Characteristics

Vance A lavas have the highest concentrations of incompatible elements (e.g. La 2.02-5.85 ppm; Ce 6.25-15.56 ppm) of all the seamount lavas. In many of the plots, the Vance A lavas plot as a distinct group. These are the same samples that have very high values of K_2O. The chondrite normalized REE patterns also are the most enriched in the LREEs as compared to lavas from the rest of the chain.

Vance B lavas show the highest degree of variation in both compatible and incompatible trace element concentrations (Ni 54.9-314.3; Y 25.5-32.2 ppm). The trace element variation

patterns (REE and mantle normalized) of the Vance B lavas tend to cluster as a fairly tight group and fall within the extremes of the Vance Seamount lavas.

Vance C lavas have, as a group, some of the lowest concentrations of incompatible elements within the Vance Seamounts (La 1.32-1.43 ppm; Ce 4.39-5.16). These very low concentrations of incompatible elements correlate with the high MgO contents in the Vance C lavas (7.34-9.45 wt. %). Their trace element variation patterns are also the most depleted for the chain (with the exception of one sample from Vance F).

There are a limited number of samples for Vance E. This was due to the extremely thick crust of Fe-Mn oxides that covered most of the samples recovered from this seamount. Even after several acid washes, it was sometimes impossible to find a sufficient amount of clean glass required for trace element analysis. These lavas most clearly follow fractional crystallization trends, also shown in the major element data. They have relatively large variations in trace element concentrations (perhaps due to crystal fractionation). The multi-element variation patterns are similar to those of B, F, and G.

Lavas from Vance F are similar to Vance C in that they have almost identical trace element concentrations. One of the Vance F samples (T1007-R2) has some of the lowest concentrations of incompatible elements found in the Vance chain (e.g. La 1.12 ppm; Y 19.9 ppm), which correlates with its very high concentration of MgO (9.34 wt. %). This sample also shows the most LREE depleted pattern of all the samples analyzed. The other multi-element normalized variation patterns from this seamount are similar to those of Vance B and C.

Vance G lavas are also restricted in their incompatible element concentrations (along with their major element concentrations) and show some evidence for fractional crystallization. The

concentrations for these lavas fall within the extremes for the chain, but have relatively higher values compared to the other seamount lavas (La 2.83-3.12 ppm; Y 28.3-30.6 ppm).

Whole Rock Trace Element Variations

A set of 23 samples from the Vance Seamounts was selected for whole rock (WR) trace element analysis. These samples were those collected in 2006 that either lacked volcanic glass or had an insufficient amount of glassy rind on which to perform analyses. It is important to note that the samples selected for WR analyses *are not* the same samples as selected for volcanic glass analyses. The whole rock trace element concentrations are presented in Figure 5-5 and REE variation and spider diagrams in Figure 5-6 and 5-7. Although the whole rocks are different samples and were analyzed by a different lab, the trace element concentrations are extremely similar to the concentrations in the glass samples and fall along the same trends in elemental variation plots. The multi-element normalized trace element patterns are also very similar to those of the glasses. The anomalous pattern of one whole-rock Vance A sample reflects the fact that this sample is an erratic, perhaps a sandstone. The other enriched patterns of the Vance A whole rock lavas may be due to the amount of crystals in the sample, as this may greatly affect the concentration of trace elements measured within sample splits. Overall, the results show that there is good analytical correlation between analyses performed at the Washington State University Laboratory and the University of Florida. That being said, the discussion of the petrogenesis of Vance Seamount lavas will focus mainly on the volcanic glass analyses, because the glass compositions better reflect the composition of the liquid at the time of eruption.

Trace Elements from other Seamounts along the Juan de Fuca Ridge

Eleven additional samples from other near-ridge seamounts along the Juan de Fuca Ridge (Figure 5-8) collected by dredging on cruises in 1994 and 1995 (M. Perfit, personal communication) were analyzed for trace element concentrations. These seamounts were

analyzed in order to provide a larger data set for near-ridge seamounts along the Juan de Fuca Ridge. These seamounts are all individual volcanic cones (as opposed to linear chains of seamounts) and are located 30-40 km from the ridge axis. The volcanic cones of these seamounts also share similar morphologies to other near-ridge seamounts in the east Pacific. One of the seamounts is located on the Pacific Plate, west of the JdFR, but 3 of the seamounts are located on the Juan de Fuca Plate, east of the JdFR. This thesis will hereafter refer to these seamounts as "JdF Seamounts". Representative trace element variation plots and multi-element diagrams of these seamounts as compared to the Vance Seamounts are presented in Figures 5-9, 5-10 and 5-11.

The JdF Seamount lavas have trace element concentrations very similar to the Vance Seamount lavas. On variation plots, the JdF Seamount lavas fall with the range of trace elements observed at the Vance Seamounts and along the same treadlines with little scatter. In general the JdF Seamounts have the same range of trace element concentrations of the Vance lavas. However, there are 3 samples that have incompatible trace element concentrations that plot higher than those in the Vance B through G samples, one of these samples is from a seamount on the Pacific Plate directly south of the Vance Seamount Chain and the other two are from seamounts further south on the Juan de Fuca Plate. These samples do not have trace element concentrations that are as high as the EMORB lavas from Vance A. The multi-element normalized variation patterns of the JdF Seamount lavas are also very similar to those of the Vance Seamount lavas and fall within the Vance Seamount field, although some of the JdF Seamounts have higher heavy rare earth element (HREE) concentrations presumably because they are less depleted than the Vance Seamounts.

Radiogenic Isotopes

A detailed discussion of the $^{87}Sr/^{86}Sr$, $^{143}Nd/^{144}Nd$, $^{208}Pb/^{204}Pb$, $^{207}Pb/^{204}Pb$, and $^{206}Pb/^{204}Pb$ values and variations in the Vance Seamount basalts is presented in *Cornejo* [2008]. A summary of those results is presented here so that correlations can be made between the trace element data and the isotopic data.

Twenty-four samples from the Vance Seamounts were analyzed. Most of these samples are the same as those analyzed for major and trace elements and are from the same glass fraction; a few of the samples analyzed for radiogenic isotopes however, were not analyzed for trace elements and vice-versa. Isotopic values are presented in Table B-3, in Appendix B and are plotted in Figures 5-12 through 5-14. $^{87}Sr/^{86}Sr$ ranges from 0.702473 to 0.702755, although some samples may have been affected by seawater contamination [*Cornejo,* 2008]; samples deemed to have been affected by seawater were not used in further discussion or figures relating to isotopes. Values of $^{143}Nd/^{144}Nd$ range from 0.513048 to 0.513182. The variations in Pb ratios are much greater than for Sr or Nd; $^{208}Pb/^{204}Pb$ ranges from 37.48 to 38.56, $^{207}Pb/^{204}Pb$ from 15.46 to 15.58, and $^{206}Pb/^{204}Pb$ from 18.12 to 18.82.

In general there are no consistent trends in isotopic variation along the seamount chain, other than the fact that isotopic values tend to cluster by seamount. Many of the isotopic ratios between seamounts, especially in Vance C, E, and G, tend to overlap one another. The Vance F samples are characterized by more radiogenic $^{143}Nd/^{144}Nd$ and less radiogenic $^{87}Sr/^{86}Sr$. Vance B is characterized by less radiogenic$^{143}Nd/^{144}Nd$ and intermediate $^{87}Sr/^{86}Sr$ values. The Vance A lavas tend to fall between the Vance C/E/G group and the Vance B lavas.

Correlations Among Data Sets

Similar magmatic processes such as the degree of partial melting, fractional crystallization, and magma mixing often affect major and trace element concentrations. In the following chapter

(Chapter 6), the roles of these different processes in the petrogenesis of the Vance Seamount lavas will be further discussed. Some general correlations between these two data sets will be made here.

In general, seamounts show a large variation in major and trace element concentrations. The seamounts that display an enriched major element signature (Vance A) also show higher incompatible trace element concentrations, as shown in a plot of $(La/Sm)_N$ versus K_2O (Figure 5-15). Seamounts that have more depleted signatures (Vance C and F) also have low concentrations of (i.e. are depleted in) incompatible elements. Individual seamounts plot in relatively tight groups in these types of plots.

Major elements do not correlate strongly with isotopic values, but this is expected because isotopic ratios are not affected by different degrees of partial melting and fractional crystallization, which strongly influence major element concentrations. The EMORB major and trace element characteristics of some Vance A lavas (high K_2O, La) do not in general correspond to expected radiogenic isotopic values characteristic of an enriched source (more radiogenic $^{87}Sr/^{86}Sr$ and Pb ratios; less radiogenic $^{143}Nd/^{144}Nd$). This lack of correlation between major elements and isotopic ratios as well as the lack of strong correlations between trace elements and isotopic ratios has also been found in other near-ridge seamounts [*Fornari et al.*, 1988a; *Leybourne and Van Wagoner*, 1991].

There is some correlation between trace elements and isotopic ratios. Figure 5-16 shows $(La/Sm)_N$ versus several isotopic ratios. In general, the higher (more enriched) $(La/Sm)_N$ values of Vance A tend to correspond with more radiogenic $^{87}Sr/^{86}Sr$ and $^{206}Pb/^{204}Pb$ and less radiogenic $^{143}Nd/^{144}Nd$, which is characteristic of a more enriched mantle source (higher Rb/Sr, lower Sm/Nd). As in previous plots of major, trace, isotopic values, lavas from Vance A and B tend to

plot separately from the other Vance lavas. Vance A lavas have relatively higher $(La/Sm)_N$ values along with isotopic values characteristic of a more enriched mantle source (more radiogenic $^{87}Sr/^{86}Sr$ and Pb ratios; less radiogenic $^{143}Nd/^{144}Nd$). The Vance B lavas have moderate $(La/Sm)_N$ values with the slightly less depleted isotopic signatures. In Figure 5-16, the Vance F samples also plot separately from the other Vance seamounts. They have very depleted $(La/Sm)_N$ values and isotopic values characteristic of a depleted mantle source (less radiogenic $^{87}Sr/^{86}Sr$ and Pb ratios; more radiogenic $^{143}Nd/^{144}Nd$).

Correlating Geochemistry with Depth, Sample Location, and Sample Type

Careful measurements of location and depth of lavas sampled were taken by the *ROV Tiburon*, but there appears to be no simple or systematic correlation between lava composition and depth (i.e. stratigraphy) within any of the geochemical data. There also appears to be no simple relationship between the individual seamounts with respect to sample depth. *Fornari et al.* [1988] found the same to be true for the Lamont Seamount Chain adjacent to the EPR.

There are also no clear trends in geochemistry based on sample location. In many instances samples that were collected from the same caldera floor or topographic ridge had similar values, but many times they did not. Samples located at a very large distance from each other had similar values in some cases, in some cases they did not. An attempt was also made to correlate sample type (e.g. pillow lava, sheet flow, massive flow) with the geochemistry. Again, there is no simple or clear relationship between lava flow morphology and geochemistry.

It is important to note that while there were a large number of samples collected from the Vance Seamounts, not all samples were geochemically analyzed. There may be no consistent trends in the data because there are not a sufficient number of analyses present to make such correlations. Also, a detailed study of the volcanology and lava flow morphology of each individual seamount may be needed to constrain flow units to distinct eruptive events. Then,

along with supplementary geochemical analyses, correlations can be made; this is perhaps beyond the scope of this thesis. However, despite these limitations, there is still much that can be learned about the petrogenesis of these seamounts from the available data.

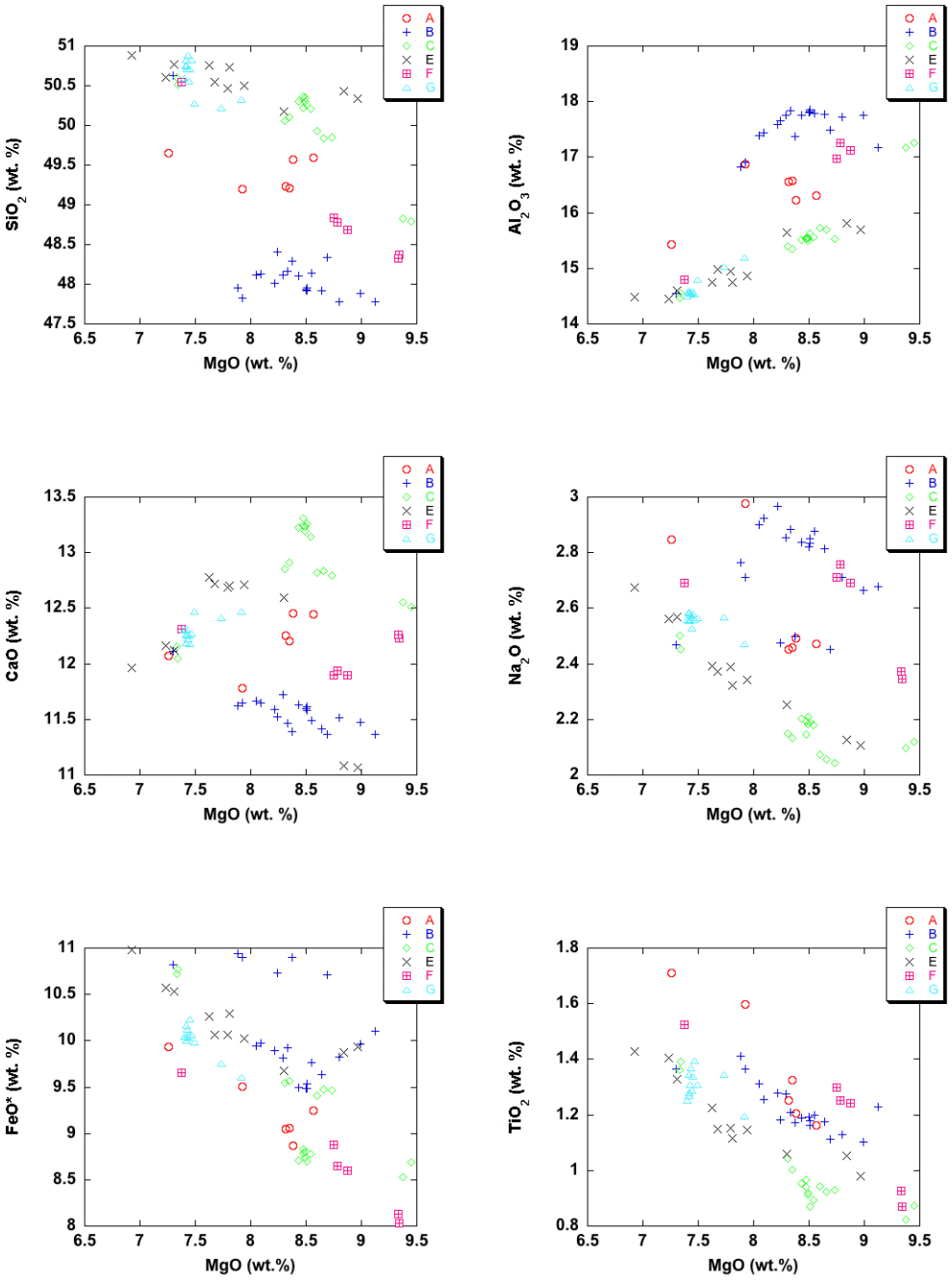

Figure 5-1. Major and minor element oxide (in weight percent) variation diagrams of Vance Seamount lavas plotted versus MgO. FeO* (total Fe) is all iron as FeO. Major element data provided by D. Clague (personal communication).

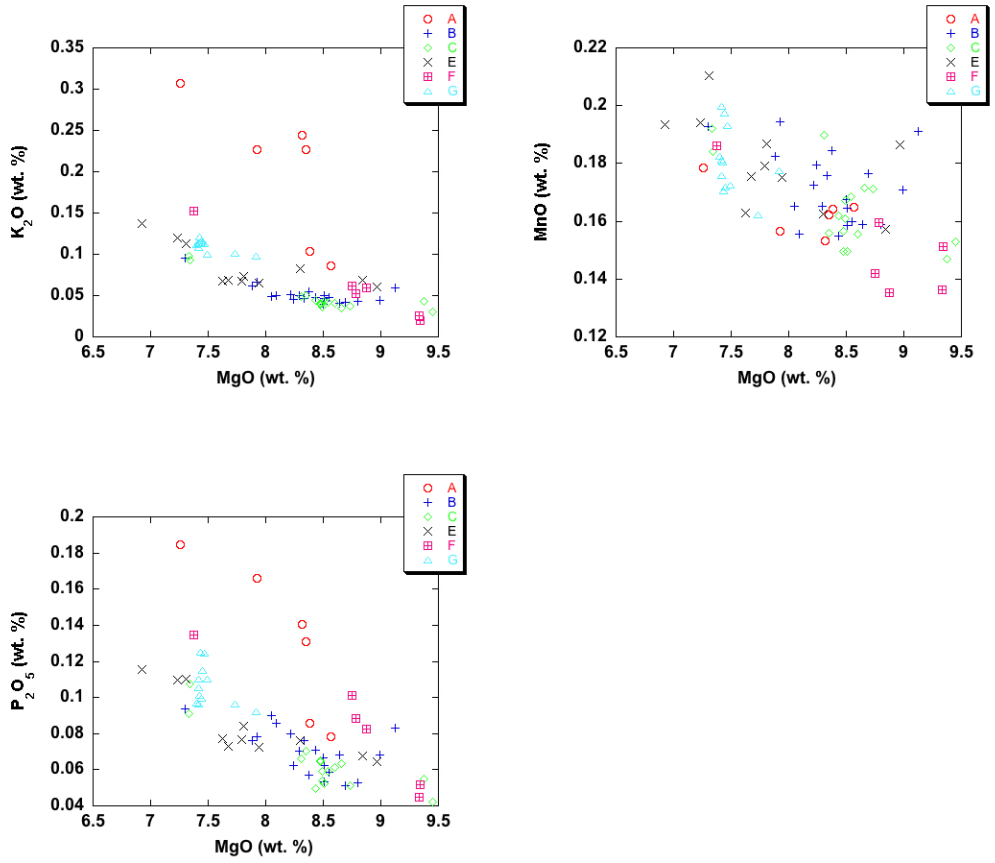

Figure 5-1. Continued.

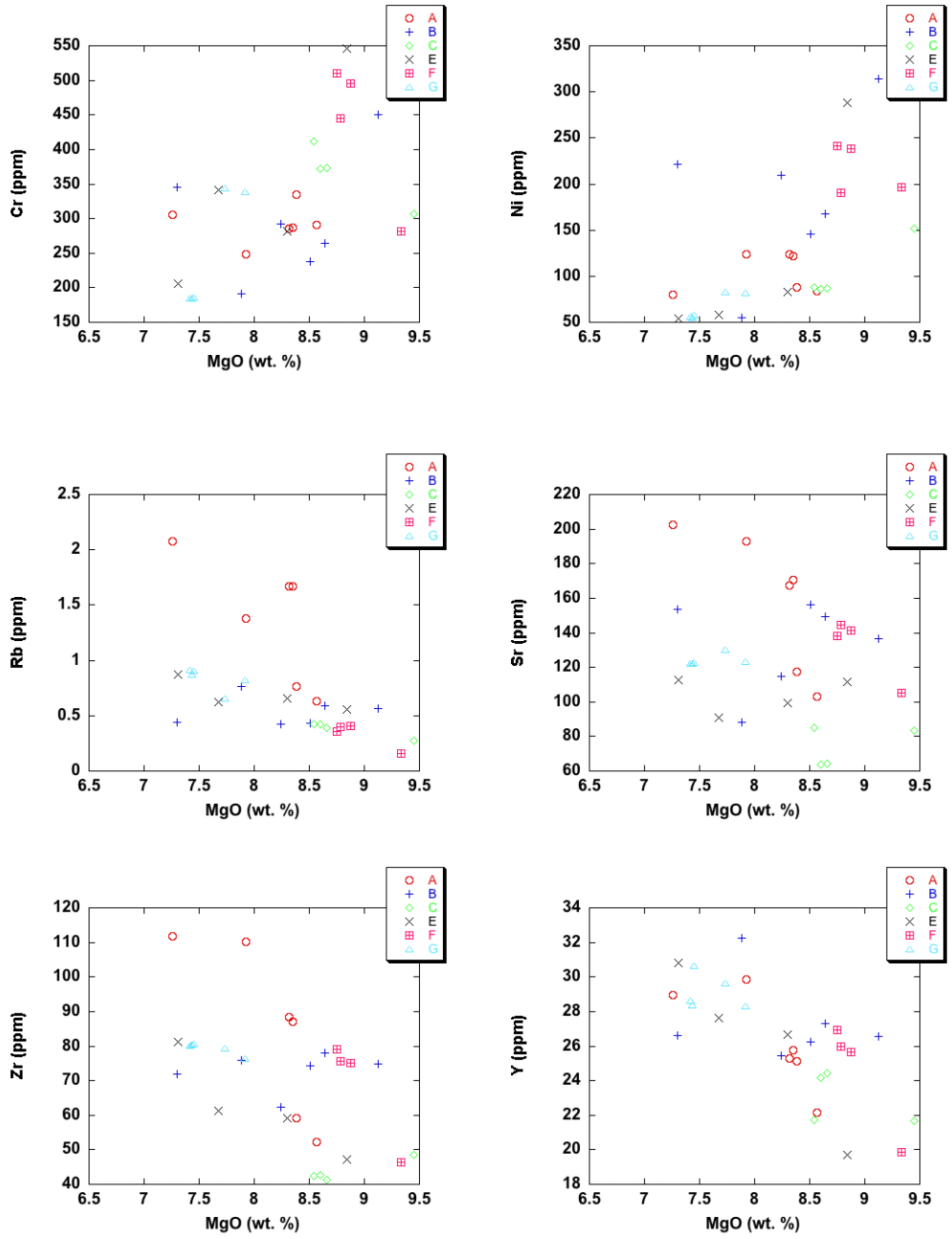

Figure 5-2. Trace element concentrations of Vance glass samples (in ppm) versus MgO. Major element data provided by D. Clague (personal communication).

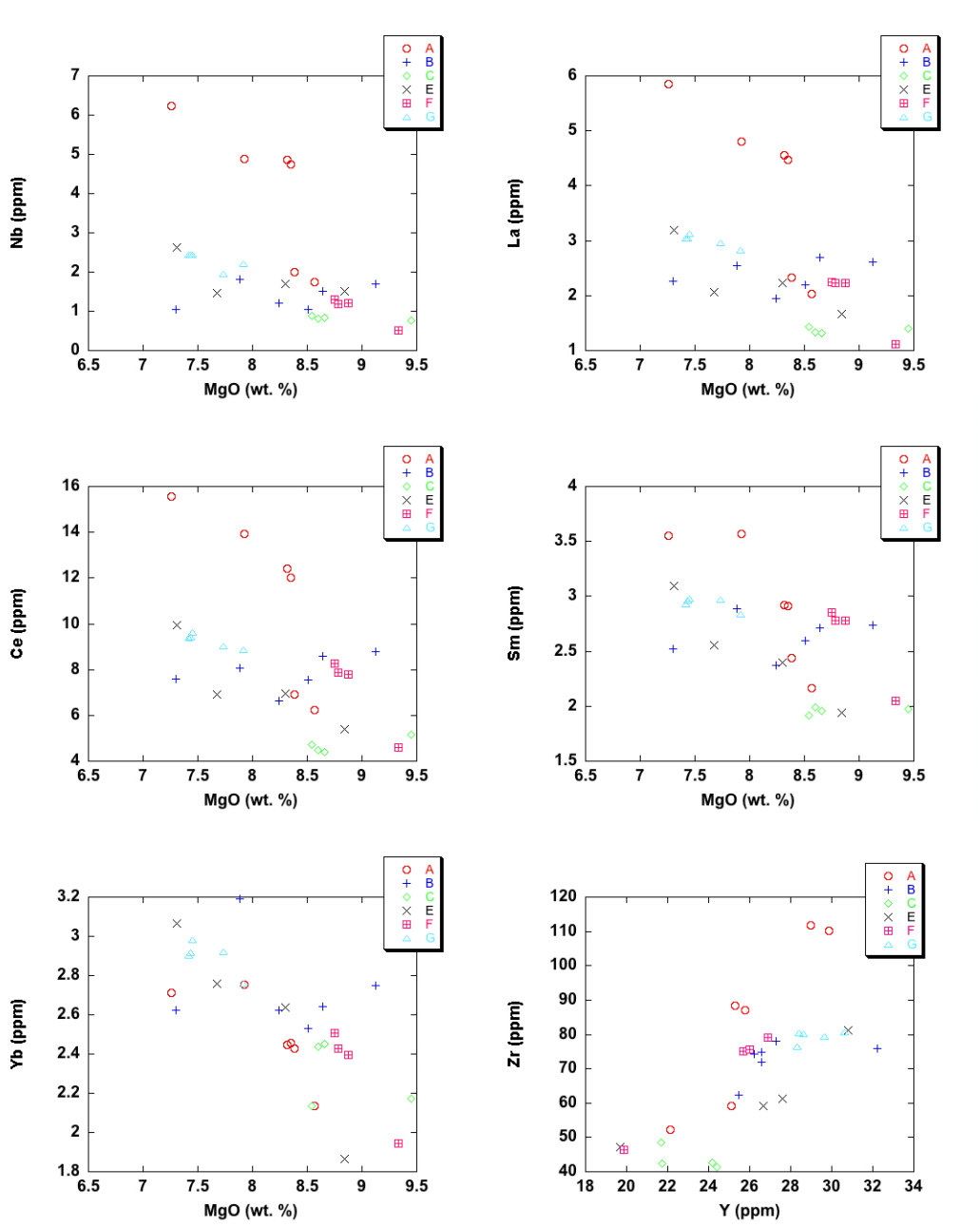

Figure 5-2. Continued.

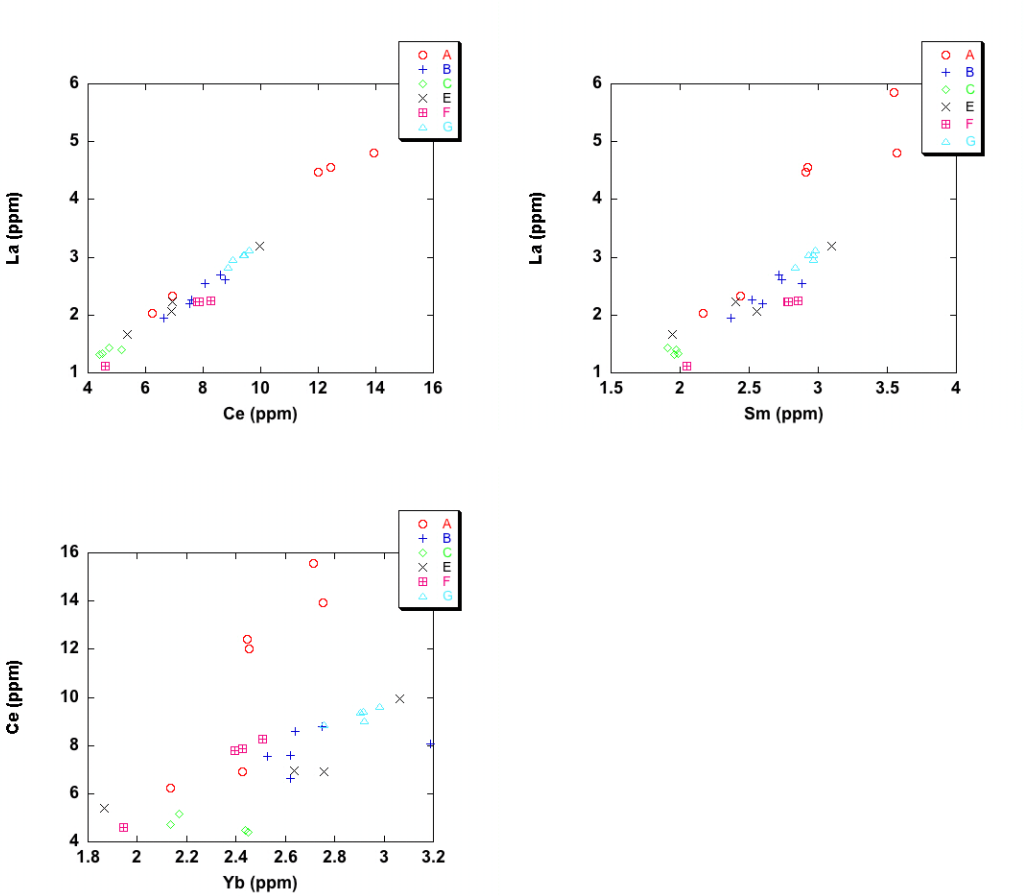

Figure 5-2. Continued.

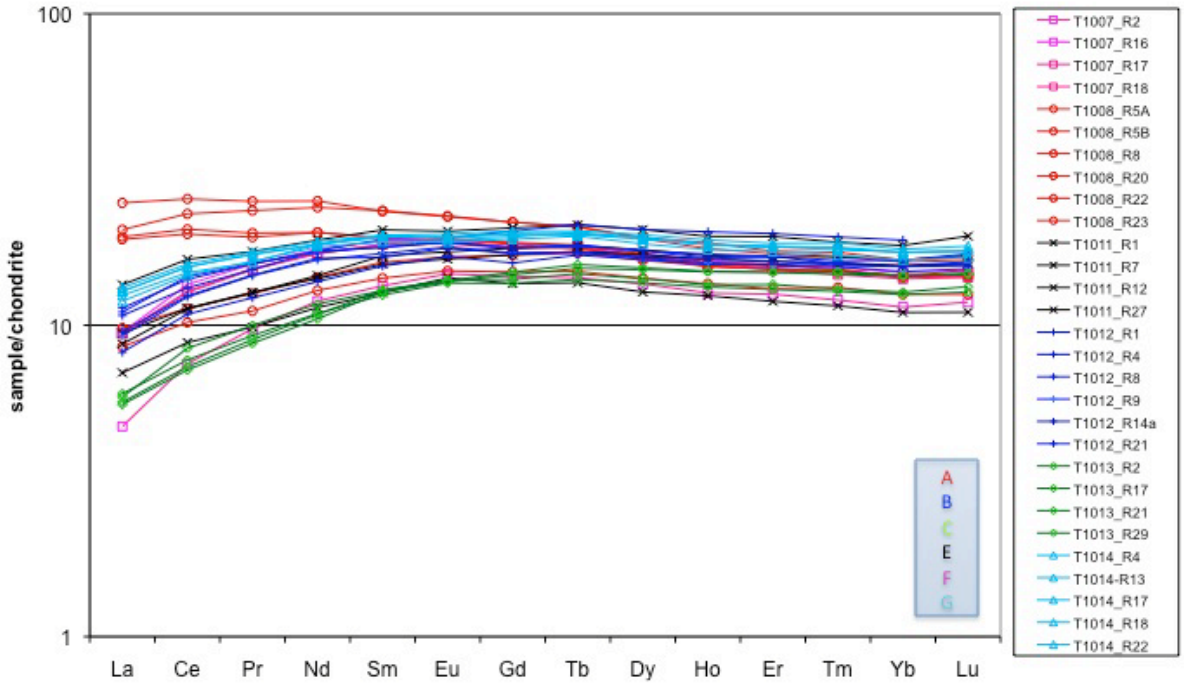

Figure 5-3. Chondrite normalized [*Sun and McDonough*, 1989] rare earth element patterns for Vance Seamount lavas.

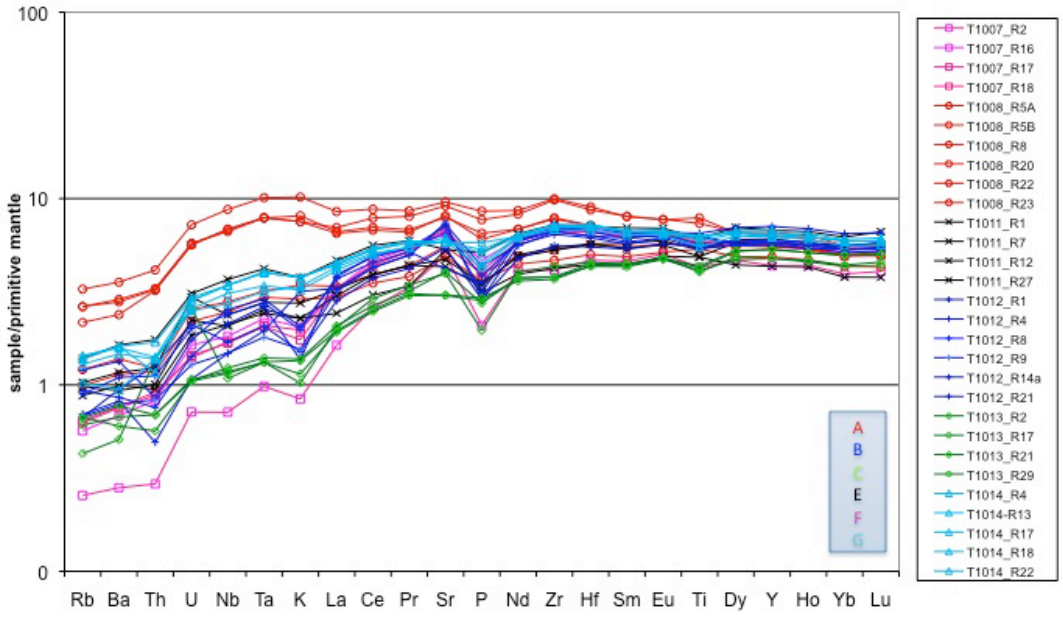

Figure 5-4. Primitive mantle normalized (or Spider Diagram) [*Sun and McDonough*, 1989] incompatible elelement patterns for Vance Seamount lavas.

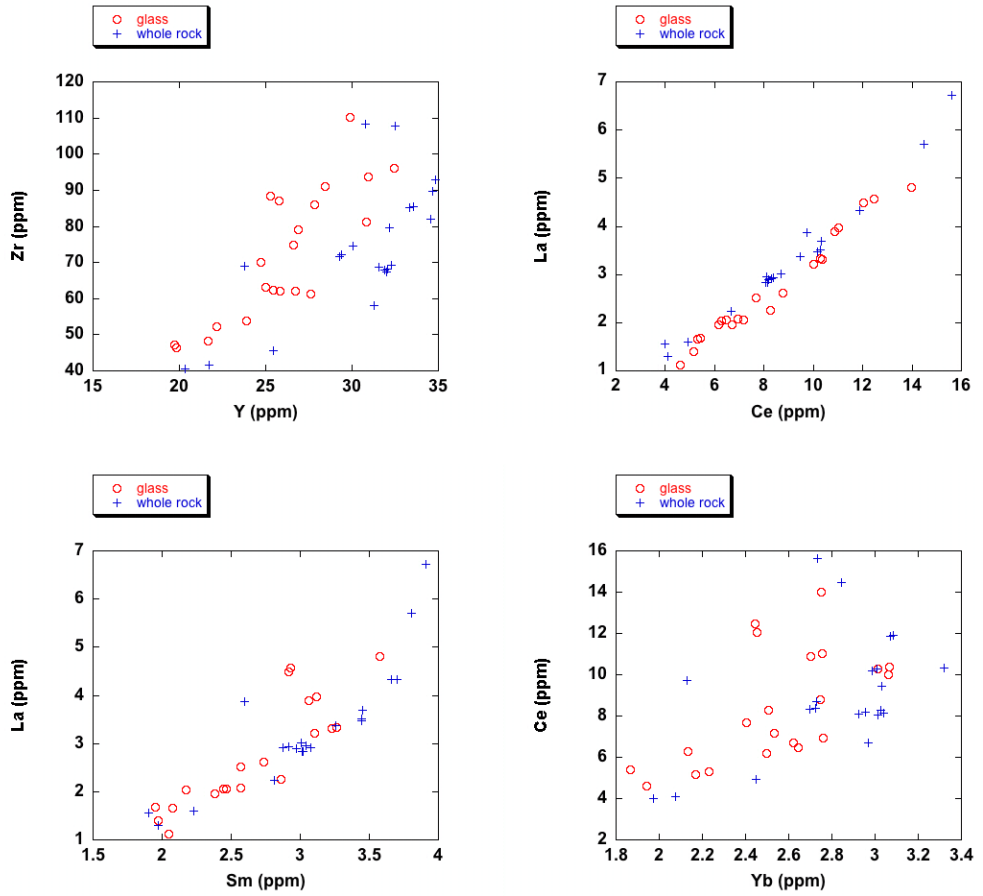

Figure 5-5. Trace element concentrations (in ppm) of volcanic glass samples (red) and whole rock samples (blue) for the Vance Seamounts. Whole rock trace element concentrations provided by D. Clague (personal communication).

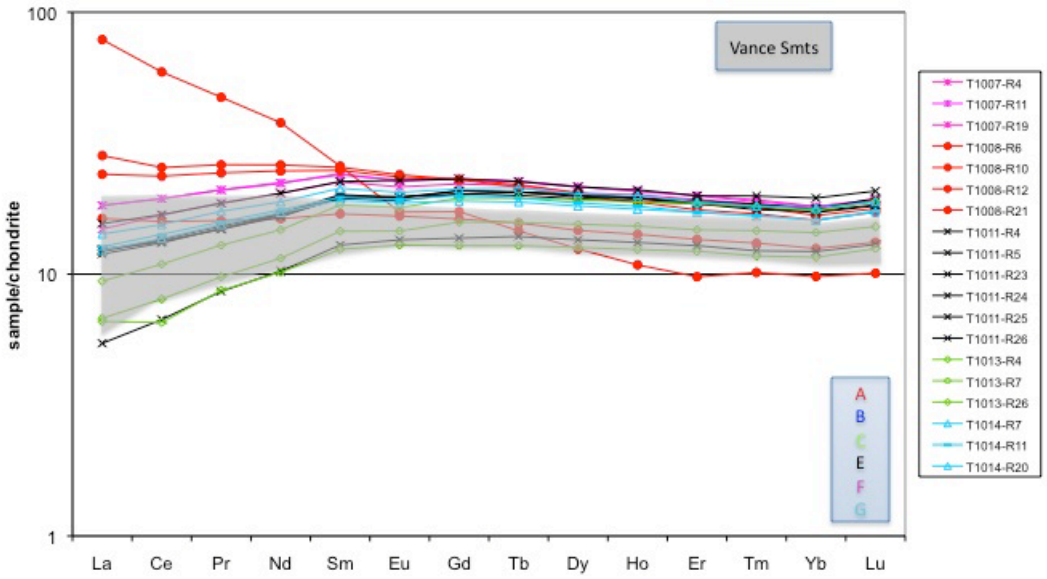

Figure 5-6. Chondrite normalized [*Sun and McDonough*, 1989] rare earth element patterns for Vance Seamount whole rock samples. Chondrite normalized Vance glass patterns (light grey) provided for reference. Whole rock trace element concentrations provided by D. Clague (personal communication).

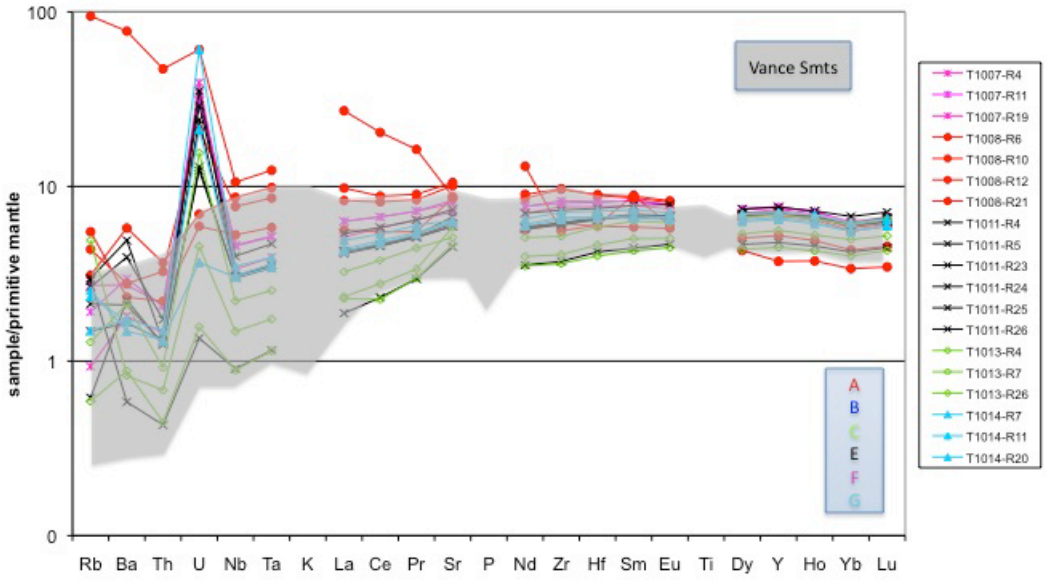

Figure 5-7. Primitive mantle normalized [*Sun and McDonough*, 1989] incompatible element patterns for Vance Seamount whole rock samples. Major element analysis for the whole rock samples has not been completed, hence the lack of data for K, Ti, and P. Primitive mantle normalized Vance glass patterns (light grey) provided for reference. Whole rock trace element concentrations provided by D. Clague (personal communication).

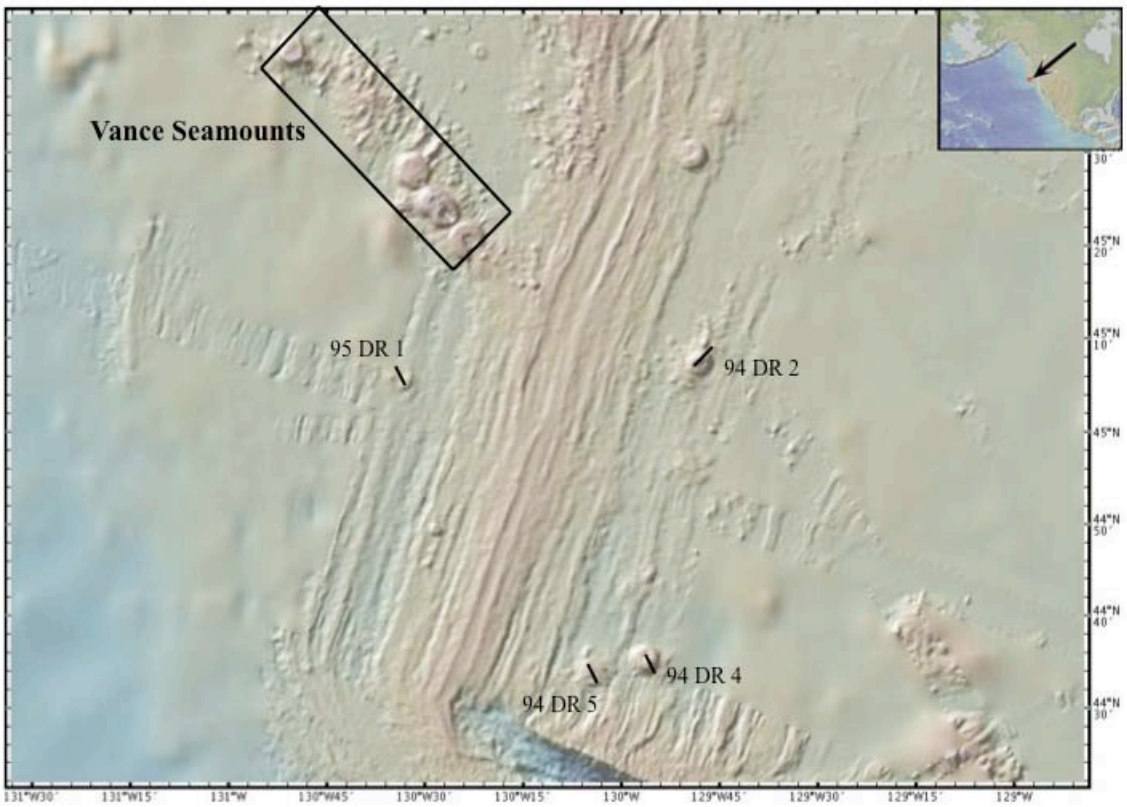

Figure 5-8. Bathymetric map of Vance Seamounts and "JdF Seamount" dredge locations. Warmer colors indicate higher elevations from the seafloor. Map created using the open source java application at www.geomapapp.org.

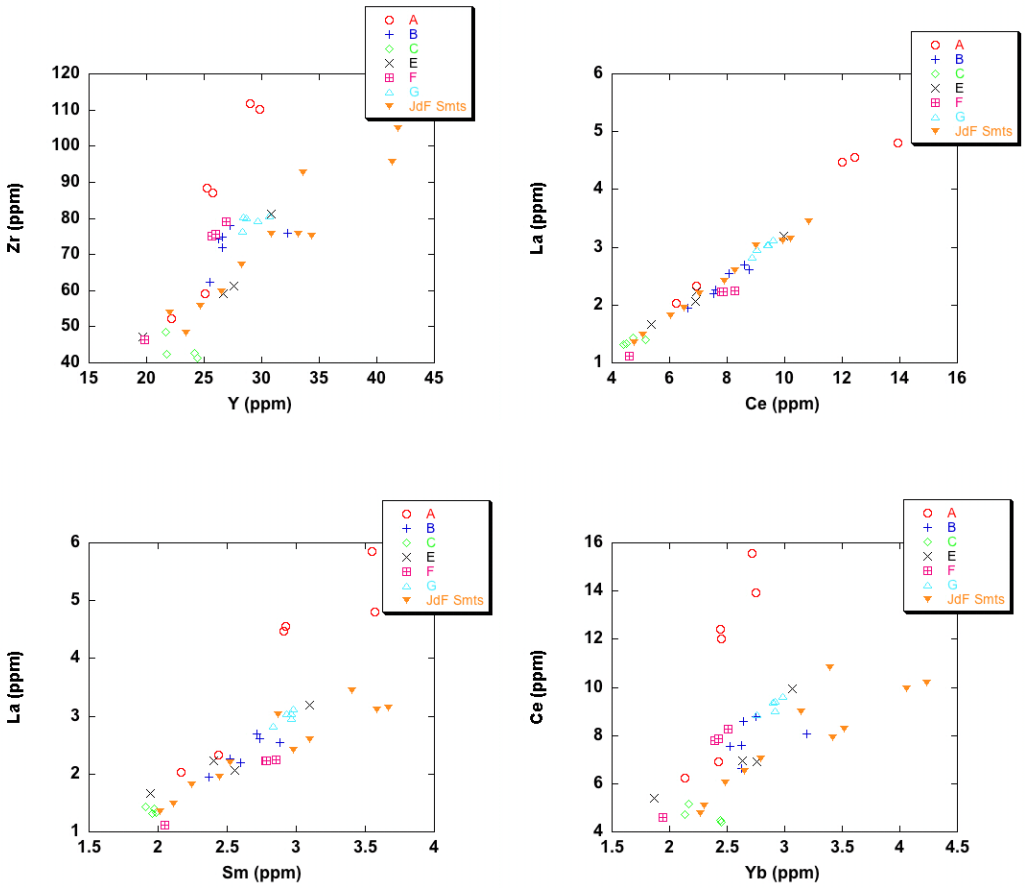

Figure 5-9. Trace element concentrations (in ppm) for Vance Seamounts and JdF Seamounts (in orange), see text for discussion.

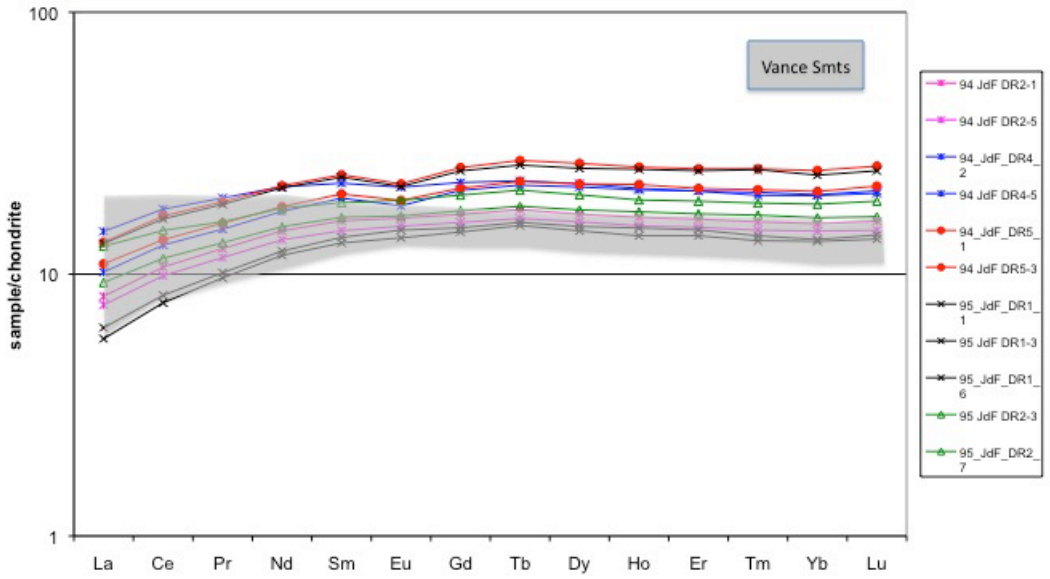

Figure 5-10. Chondrite normalized [*Sun and McDonough*, 1989] rare earth element patterns for JdF Seamount samples. Chondrite normalized Vance glass patterns (light grey) provided for reference.

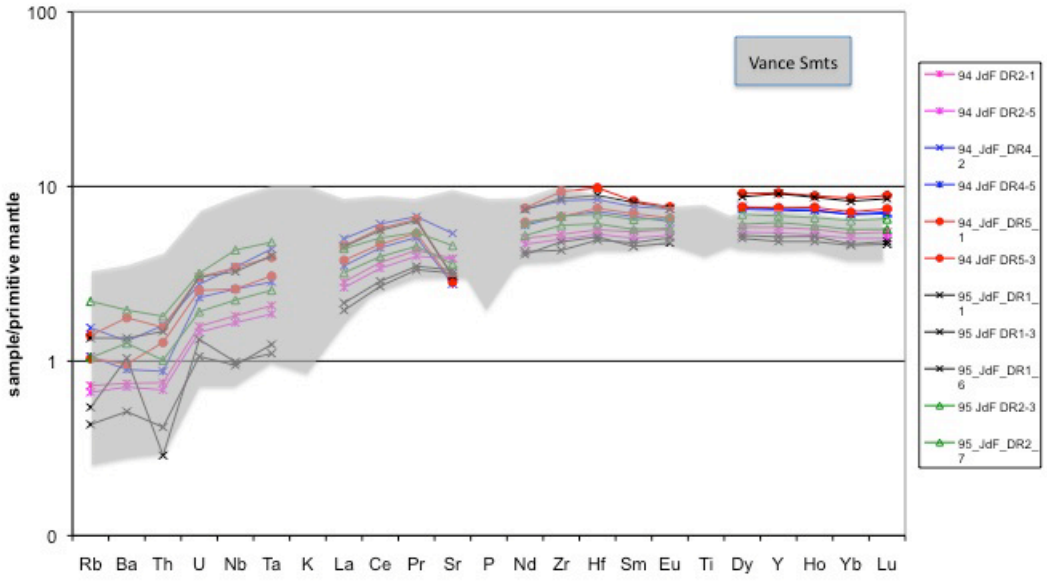

Figure 5-11. Primitive mantle normalized [*Sun and McDonough*, 1989] incompatible element patterns for JdF Seamount samples. Major element analysis for JdF Seamount lavas has not been completed, hence the lack of data for K, Ti, and P. Primitive mantle normalized Vance glass patterns (light grey) provided for reference.

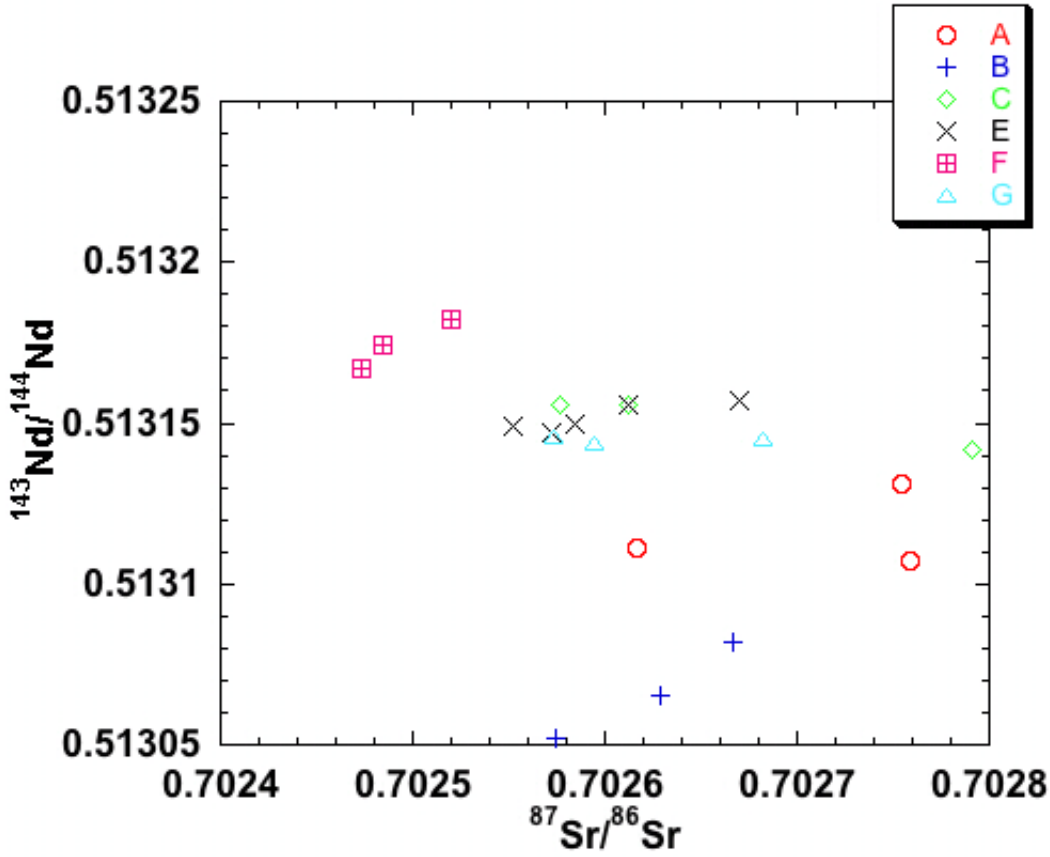

Figure 5-10. The $^{87}Sr/^{86}Sr$ versus $^{143}Nd/^{144}Nd$ for Vance Seamount lavas. Radiogenic isotope values from *Cornejo* [2008].

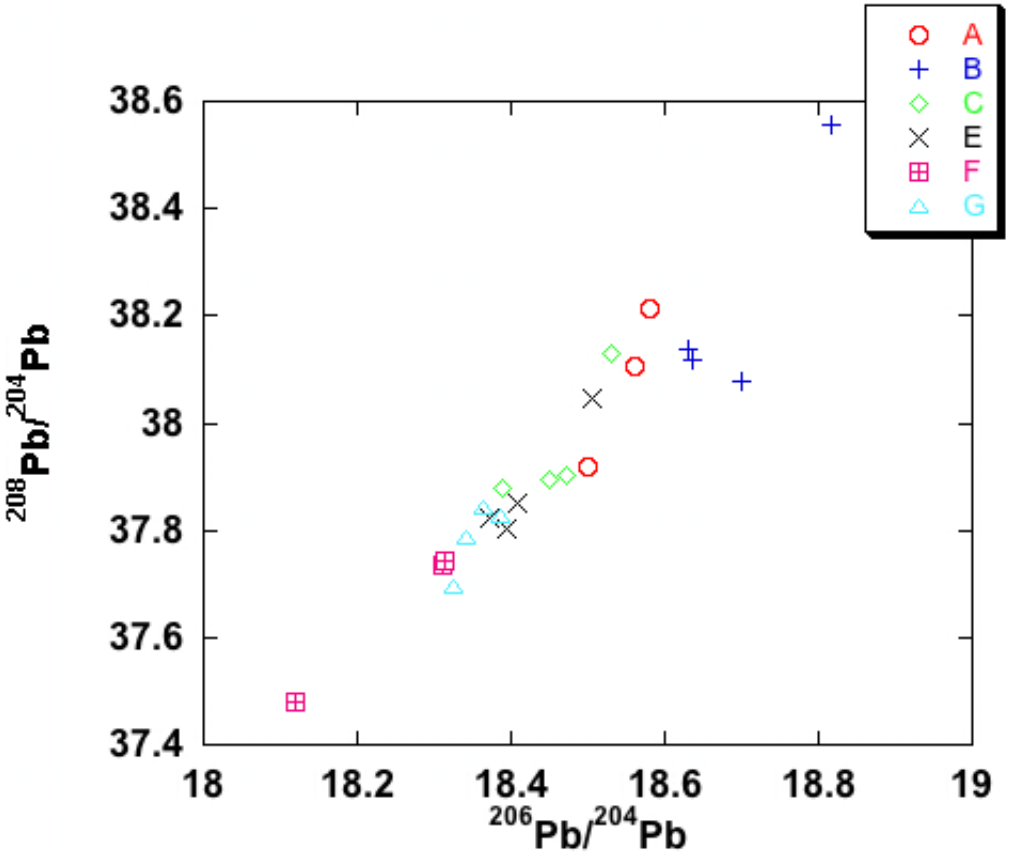

Figure 5-11. The $^{208}Pb/^{204}Pb$ versus $^{206}Pb/^{204}Pb$ for Vance Seamount lavas. Isotope data from *Cornejo* [2008].

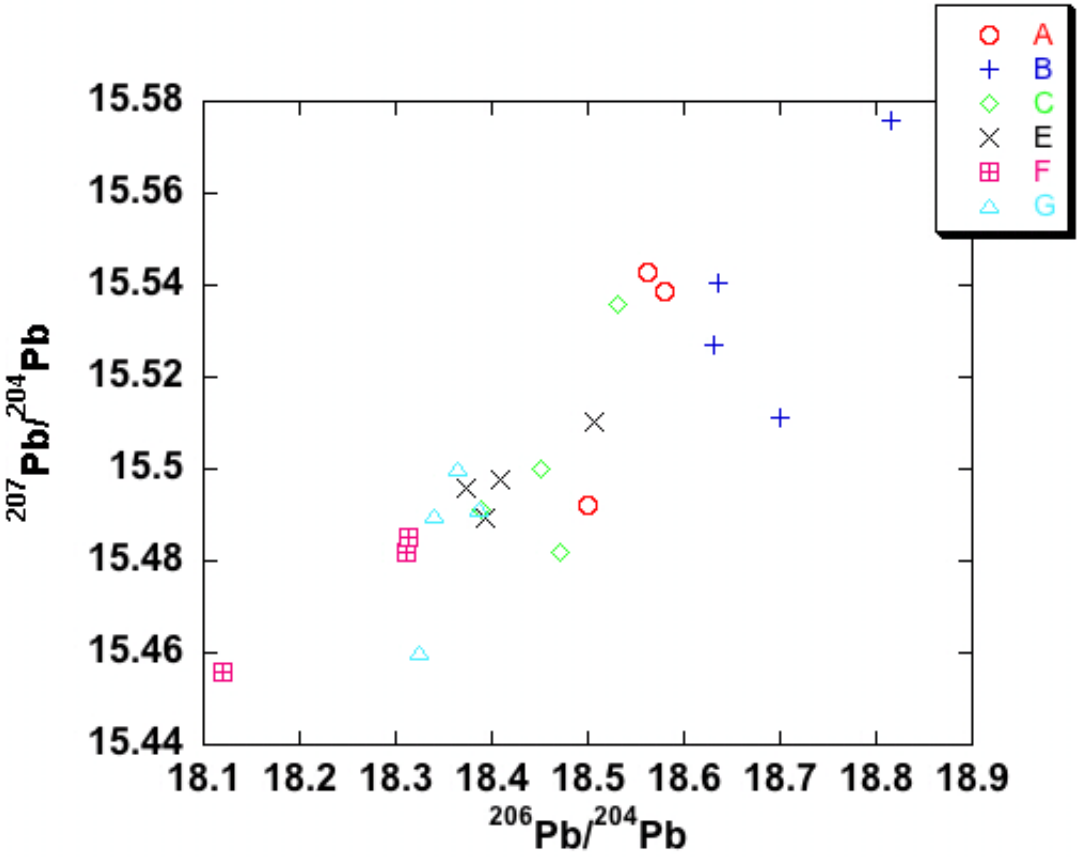

Figure 5-12. The $^{207}Pb/^{204}Pb$ versus $^{206}Pb/^{204}Pb$ for Vance Seamount lavas. Isotope data from *Cornejo* [2008].

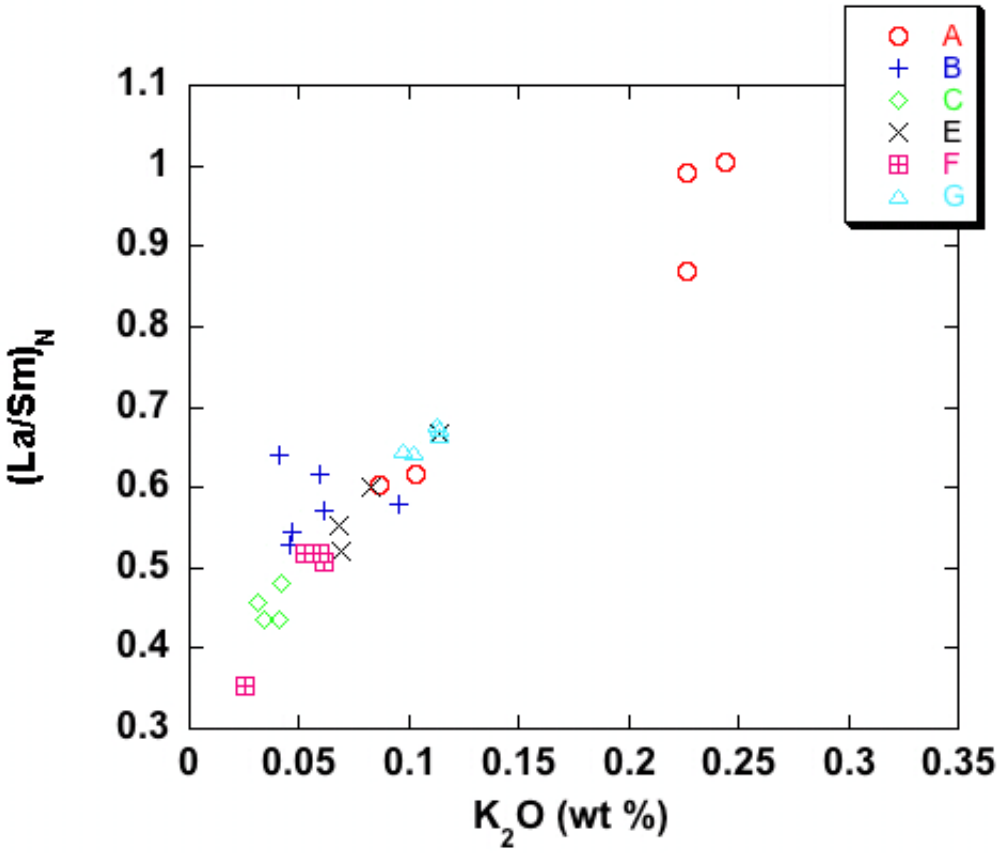

Figure 5-13. The $(La/Sm)_N$ versus K_2O for the Vance Seamounts lavas. Major element data provided by D. Clague (personal communication).

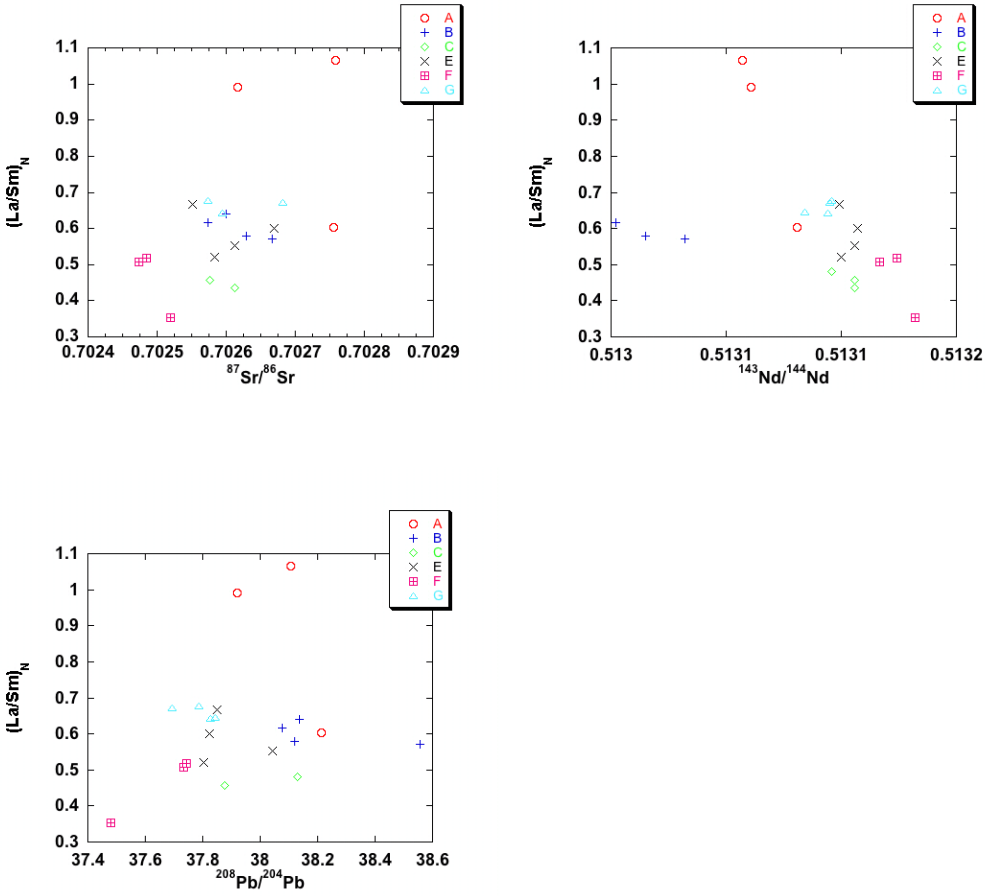

Figure 5-14. The $(La/Sm)_N$ versus $^{87}Sr/^{86}Sr$, $^{143}Nd/^{144}Nd$, and $^{208}Pb/^{204}Pb$ for Vance Seamount lavas. Isotope data from *Cornejo* [2008].

CHAPTER 6
DISCUSSION

Comparison with the Adjacent Southern Juan de Fuca Ridge

A large geochemical data set has been compiled to represent compositions of on-axis lavas along the Southern Juan de Fuca Ridge. Samples from the Southern Cleft Segment (S. Cleft) are primarily used for comparison as representative on-axis samples. It is one of the segments adjacent to the Vance Seamount chain and also represents one of the least complex segments on the JdFR, which is unaffected by "hotspot" melting, chemical anomalies, recent episodes of rift propagation, or enriched mantle sources [*Smith et al.*, 1994]. The large number of chemical analyses that comprises the "southern JdFR" data set includes samples from the Vance, northern Cleft, and southern Cleft segments of the Juan de Fuca Ridge. This data set, which includes major element, trace element, and radiogenic isotope analyses, is from a number of sources, including *Smith et al.* [1994], *Stakes et al.* [2006], and M. R. Perfit, personal communication. Isotopic data also include analyses completed by *Eaby et al.* [1984], *Hegner and Tatsumoto* [1987], *Ito et al.* [1987], and *White et al.* [1987].

The Vance Seamount lavas are more primitive and span a much smaller chemical range (MgO 6.9-9.5 wt. %, average 7.89 wt. %, median 8.32 wt. %, n=71) than S. Cleft lavas (MgO 3.76-8.54 wt. %, average 6.41 wt. %, median 6.68 wt. % n=227). Vance Seamount basalts are more depleted in TiO_2 and FeO* and the Vance A samples are more enriched in K_2O at similar MgO values than the adjacent ridge basalts (Figure 6-1). Additionally, Vance Seamount lavas show different major element trends than the S. Cleft lavas. The Vance A, B, and F lavas also have higher Na_2O contents compared to the S. Cleft lavas at the same MgO content, while lavas from Vance C and E have lower Na_2O. Vance B lavas also have distinctly lower CaO values at similar MgO contents in comparison to the ridge lavas.

Incompatible trace elements are in general less abundant in the seamount samples than in the S. Cleft samples at similar MgO contents (Figures 6-2 and 6-3). Most of the Vance seamount lavas have REE patterns and mantle-normalized patterns similar to the more mafic axial samples. Although there is overlap between the patterns of the Vance lavas and the ridge lavas, many of the seamount samples cluster at the more depleted end of the spectrum, with some samples showing a stronger depletion in the LREEs than the adjacent ridge lavas. The low abundances and restricted range of the seamount lavas are also very evident when comparing incompatible trace elements from the two suites (Figure 6-4). The exception is Sr, an alkaline earth element that is moderately compatible in plagioclase but incompatible in olivine and pyroxenes. Variations in Sr abundances in axial samples are consistent with the behavior of Sr during fractional crystallization (i.e. little change in concentration), but lavas from Vance A and B have higher concentrations at high MgO values, suggesting slightly enriched sources were involved in the formation of these lavas. The seamount lavas show a much larger range in incompatible trace element ratios than basalts from the adjacent ridge; the seamount $(La/Sm)_N$, $(Ce/Yb)_N$, and Zr/Y range from 0.35-1.07, 0.50-1.59, and 1.69-3.86 respectively, compared to 0.53-0.96, 0.69-1.09, and 2.42-3.96 for the S. Cleft samples. However, a majority of the seamount lavas have highly depleted compositions (e.g. $Zr/Y<2.5$, Figure 6-4).

Isotopic compositions of the Vance Seamount samples [*Cornejo,* 2008] are plotted along with samples from the Southern Juan de Fuca Ridge in Figure 6-5. Many of the seamount samples have Nd and Sr compositions similar to the SJdFR lavas, but some samples from Vance A and B have more radiogenic Sr and less radiogenic Nd than the ridge lavas that is indicative of their derivation from a more enriched (or less depleted) mantle source(s). Pb isotopic ratios of the Vance Seamounts also overlap with compositions from the SJdFR, but the ridge samples

have a much more restricted range in values than the seamount samples. The Vance Seamounts range from both less radiogenic to more radiogenic than the adjacent ridge. Variations in $^{143}Nd/^{144}Nd$ versus $(Ce/Yb)_N$ (Figure 6-6), indicate that the Vance Seamount lavas have REE source values that are typical for this region in the Pacific and most of the lavas sampled do not have isotopic compositions that differ significantly from ridge lavas. However, lavas from Vance A and Vance B have values that suggest slightly different, more incompatible element and isotopically enriched sources.

In summary, lavas from the Vance Seamounts are more geochemically diverse than JdF ridge samples and in that way differ significantly from their on-axis counterparts. The Vance lavas are more primitive than and are more incompatible element depleted, with the exception of lavas from Vance A (that are slightly enriched), than lavas from the adjacent ridge. They also have a greater range in isotopic compositions compared to the relatively restricted range of compositions from the ridge. This geochemical diversity suggests that the mantle underling the Vance Seamounts is heterogeneous on a relatively small scale (e.g. significant variation in geochemistry between and within seamounts) but the extent of this heterogeneity is somewhat masked by mixing of melts as they rise to the surface. It is likely that this inherent heterogeneity preserved in the seamount samples also exists beneath the SJdF ridge but is obscured due to the pooling and efficient mixing of large amounts of different magmas in sub-axial magma bodies. The Southern Juan de Fuca Ridge and the Vance Seamounts share similar mantle source material, but the diversity in small-scale source characteristics (i.e. trace element composition) is not homogenized during formation of seamount lavas as it is with the ridge lavas. The more evolved and homogeneous lava compositions from on-axis are more influenced by fractional

crystallization and mixing that likely occurs in long-lived magma chambers that exist in the uppermost crust beneath the SJdF ridge crest.

Comparison with Other Near-Ridge Seamounts

Other near-ridge seamounts in the northeast Pacific have similar geochemical characteristics to those of the Vance Seamounts. The Heck and Heckle Seamounts on the western flanks of the Endeavor segment of the JdFR are comprised of very primitive lavas (Mg# 60-69) that overlap with the more primitive compositions of the Vance lavas. The Heck and Heckle lavas also have lower TiO_2 and FeO*, higher CaO, and similar Na_2O at similar MgO compared to adjacent West Valley Ridge basalts. They have very depleted incompatible trace element compositions (Zr/Y 1.9-2.4) and have LREE-depleted chondrite-normalized REE patterns ($[La/Sm]_N$ 0.65-0.77) that also overlap with those of depleted lavas of the Vance Seamounts, although some samples from the Vance Seamounts are even more depleted (Figure 6-7). Heck and Heckle lavas show a much more restricted range of trace element compositions and isotopic ratios than the adjacent ridge and the Vance Seamounts. Samples from Heck and Heckle have less radiogenic isotopic signatures than the West Valley Ridge, and these signatures are similar to the most "depleted" (less radiogenic $^{87}Sr/^{86}Sr$ and Pb ratios; more radiogenic $^{143}Nd/^{144}Nd$) of the Vance Seamount lavas from Vance F (Figure 6-8) [data from *Leybourne and Van Wagoner*, 1991; *Van Wagoner and Leybourne*, 1991; *Cousens et al.*, 1996].

The President Jackson Seamounts are also primitive in composition (Mg# to 69.5) with lower TiO_2 and FeO*, and higher CaO and Na_2O at similar MgO contents compared to adjacent Gorda Ridge lavas. Incompatible elements range from very depleted to slightly depleted [K_2O 0.07-0.24 wt. %, $(La/Sm)_N$ 0.54-0.86], exhibiting much less variation than the Vance Seamount samples. The President Jackson Seamounts, like some lavas from the Vance Seamounts, are more enriched in Sr (123-171 ppm) than the adjacent axial lavas. The chondrite normalized REE

patterns show LREE depletions, but no patterns show the strong LREE depletions that are typical of lavas from Vance C. Lavas from the President Jackson Seamounts are in general more heterogeneous than lavas from the Gorda Ridge, similar to the relationship observed between the Vance Seamounts and the Southern Juan de Fuca Ridge. The isotopic ratios are characteristic of a slightly more enriched source (more radiogenic $^{87}Sr/^{86}Sr$ and Pb ratios; less radiogenic $^{143}Nd/^{144}Nd$) than the Gorda Ridge and are similar to the more "enriched" lavas from Vance A [*Davis and Clague*, 2000].

Seamounts along fast-spreading ridges, like those along the northern East Pacific Rise have been better studied than those in the NE Pacific. The Lamont Seamounts, adjacent to the EPR around 10°N, share many characteristics common to near-ridge seamount chains in the NE Pacific. Lavas from this chain are also very primitive (Mg# to 71) and have the distinctive lower TiO_2 and higher CaO at similar MgO when compared to lavas from the EPR. These lavas also have variable Na_2O, some lavas having higher concentrations at similar MgO than the EPR. The Lamont Seamounts have low incompatible element concentrations and LREE depleted trace element patterns (La 0.96-3.77 ppm; $(La/Sm)_N$ 0.26-0.57) relative to the basalts found on-axis. The Lamont Seamounts overlap with the most depleted to slightly depleted samples of the Vance Seamounts, with some Lamont samples being more depleted in the most incompatible trace elements than the Vance Seamounts. Although EMORB compositions have been found at other near-ridge seamounts near the EPR [*Batiza and Vanko,* 1984; *Allan et al.*, 1987; *Niu and Batiza*, 1997], there are no enriched trace element compositions found at the Lamont Seamounts that compare to the enriched compositions of the Vance A lavas. Like the Vance Seamounts, the isotopic compositions range from more radiogenic to less radiogenic than the adjacent EPR. In particular, the range in Pb isotopic values from the Lamont Seamounts is significantly greater

than that found on the EPR, Juan de Fuca, and Gorda Ridges [*Fornari et al.*, 1988a]. Overall, near-ridge seamounts are comprised of basaltic lavas that are similar, more depleted, or more enriched (or include the entire range), with respect to incompatible trace elements and isotopic compositions, than comparable MORB on adjacent ridges. In general, lava compositions are more heterogeneous (i.e. have distinct major and trace element compositions and include a large range of major and trace elements at a given MgO value) than on-axis lavas.

The "JdFR Seamounts" discussed in this thesis are similar to the Vance Seamounts and the slightly less depleted samples trend toward those of the President Jackson Seamounts. None of the lavas analyzed from the JdFR Seamounts have compositions trending toward EMORB, like those from Vance A. Trace element concentrations of the JdFR Seamounts are similar to concentrations found in other near-axis seamount chains, indicating that they are not unusual compositions for near-ridge seamount chains. However, the Vance Seamounts are much more compositionally diverse than the other seamount chains, with the "depleted" lavas of the Vance Chain resembling the Heck and Heckle Seamount compositions and the more "enriched" lavas resembling those of the President Jackson Seamounts (with respect to both trace elements and isotopic ratios). This supports the idea that the mantle beneath the Vance Seamounts is compositionally heterogeneous on a relatively small scale, but that the seamounts and the adjacent ridge do share common source materials. The enriched mantle sources of Vance A and B are unusual for Southern Juan de Fuca axial lavas, but compositions (both trace element and isotopic) for Vance A are similar to those of the President Jackson Seamounts. This suggests that the more enriched mantle component (typical of Vance A) that is present in the mantle beneath the Gorda Ridge is also present in the mantle below the Juan de Fuca Ridge. The Vance B lavas have similar (although form a distinct group) major and trace element compositions to the other

Vance Seamount lavas. However, their isotopic composition indicates a different source that the other seamounts, as well as a different source than the adjacent Southern Juan de Fuca Ridge.

A larger isotopic data set from the entire Juan de Fuca ("All JdF") is included in relation to the Vance Seamounts in Figure 6-9. This data set is a large compilation of isotopic data from the Cleft, Vance, Cobb, CoAxial, Explorer, and Endeavour Ridges, along with samples from Axial, Rouge, and Eickelberg Seamounts and the Southwest Rift Zone [M. R. Perfit, personal communication, *Stakes et al.*, 2006, *Chadwick et al.*, 2005; *Smith et al.*, 1994, *Desonie and Duncan*, 1990; *Rhodes*, 1990; *Hegner and Tatsumoto*, 1987, *Ito et al.*, 1987, and *Eaby et al.*, 1984]. The Vance B samples are not anomalous in relation to the enlarged data set. Samples from Axial Seamount plot with isotopic values closest to the Vance B lavas. The mantle source of the Vance B lavas may not be evident along the Southern Juan de Fuca Ridge, but appears to be present in the larger Juan de Fuca area.

Petrogenesis of Vance Seamount Lavas

Major element analyses indicate that lavas from the Vance Seamount Chain primarily are primitive (high MgO), subalkaline MORB. Variations in K_2O (0.02-0.31 wt. %) between the seamounts indicate a range in compositions from very depleted to slightly enriched MORB. Trace element data indicate that Vance Seamount lavas have strongly depleted to slightly enriched light rare earth element patterns [$(La/Sm)_N$ 0.35-1.07]. This data together with variable isotopic ratios [*Cornejo*, 2008] indicate that multiple sources may have been involved in the petrogenesis of the Vance Seamount lavas. These include typical MOR depleted mantle sources (characterized by having less radiogenic $^{87}Sr/^{86}Sr$ and $^{206}Pb/^{204}Pb$ and more radiogenic $^{143}Nd/^{144}Nd$) to a more enriched mantle source (with more radiogenic $^{87}Sr/^{86}Sr$ and $^{206}Pb/^{204}Pb$ and less radiogenic $^{143}Nd/^{144}Nd$). The observed variations in major, trace, and isotope geochemistry are present between seamounts in the chain and also to some extent within

individual seamounts. Some of the intra-seamount variations are consistent with fractional crystallization where as inter-seamount elemental and isotopic variations indicate that different extents of partial melting, and/or multiple parental compositions must have been involved in the petrogenesis of magmas that formed the seamounts.

In order to better constrain and evaluate the origins of the range of compositions found in the seamount lavas geochemical modeling was utilized to test various petrogenetic hypotheses including the composition of the mantle source, the style and extent of melting of that source, style and extent of crystallization of the melt, and mixing with other melts [*Langmuir et al.*, 1992].

Fractional Crystallization

Major element modeling

The computer program PETROLOG 2.1 [*Ariskin*, 1999; *Danyushevsky*, 2001] was used to model fractional crystallization for Vance Seamount lavas. This program uses mineral-melt equilibrium equations to calculate compositions of crystals and residual melts for small increments of fractional crystallization, which result in model liquid lines of descent (LLD). Users can define various starting conditions, such as water content, parental composition, mineral assemblage, pressure, and oxygen fugacity.

Individual seamounts tend to have lavas that form distinct trends on major element diagrams suggesting they are cogenetic and may have the same or similar parental magmas. For this reason, representative parental melts were chosen from each seamount to better approximate the variations in the data. In this case the parental melts were estimated to have the composition of the most primitive sample (highest wt. % MgO) recovered from each seamount; they include samples T1008-R23 (A), T1012-R08 (B), T1013-R17 (C), T1011-R2 (E), T1007-R1 (F), and T1014-R13 (G) (Table B-1). In the calculations, olivine, plagioclase, and clinopyroxene were

chosen as potential crystallizing phases [*Ford et al.,* 1983; *Weaver,* 1990; *Langmuir,* 1990; *Ariskin et al.,* 1986] based on well known phase relations in MORB [*Langmuir et al*., 1992]. Olivine and plagioclase are present as microphenocrysts in the Vance lavas and clinopyroxene appears rarely as a microphenocryst phase in some samples [*Cornejo*, 2008; *Finney,* 1989]. The pressure of crystallization was set at 1 kbar to approximate pressures within the shallow crust, typical for crustal magma bodies of MORs [*Langmuir et al.,* 1992] and the oxidation state was set at the QFM fO_2 buffer [*Borisov and Shapkin,* 1990]. Crystal-liquid equilibrium calculations were made after each 0.01 wt. % of the mineral phases were subtracted from the melt, and the calculations were terminated once the system reached 50% crystallization. Terminating the calculations at 50% crystallization was chosen because even the most evolved Vance Seamount lavas have relatively high MgO values indicating a lack of extensive fractional crystallization in the various suites. Also, the Vance Seamount lavas are petrographically simple, many samples having very small amounts, if any, of microphenocrysts and large amounts of glass [*Cornejo,* 2008; *Finney*, 1989]. Different starting conditions which included variations in water content, oxidation state, and pressure were also used to model LLDs, but did not closely resemble the observed major element variations and are therefore not plotted or discussed in relation to the petrogenesis. The most successful fractional crystallization models are plotted along with major element data in Figure 6-10. Figure 6-11 illustrates the changes in phase proportions with temperature in a typical model. In general the phase relations, order of crystallization, and temperatures are similar in most of the successful models with temperatures of initial crystallization beginning at 1238°C with plagioclase as a liquidus phase, followed by olivine after approximately 2% crystallization at 1236°C. Clinopyroxene begins to appear at 1164°C after about 44% crystallization.

In general, the LLDs predicted by the fractional crystallization calculations suggest only 20-25% crystallization is required to match the entire range of MgO values of the Vance Seamounts, but the models do not provide a good match with many of the other major elements. The variations in Al_2O_3 and K_2O are the most poorly predicted from the models. For example, Vance A lavas clearly show more enrichment in K_2O than any of the predicted models can account for and must be affected by some other process besides fractionation. Vance B and Vance C lavas tend to follow fractional crystallization patterns the best, with some scatter. Lavas from Vance A and Vance F consistently do not follow any of the predicted fractional crystallization trends.

The variation seen in the major elements in the entire chain clearly cannot be explained by fractional crystallization of a single parent-nor would they be expected to. However, with the possible exceptions of Vance B and C, lavas from individual seamounts do not follow simple fractional crystallization trends and thus are unlikely to be related to one another by crystallization from the same parental melt composition. The possible relation of the Vance B and C lavas through fractional crystallization can be further constrained by modeling trace element abundances in the Vance Seamount lavas.

Trace element models

Variations in trace element abundances were modeled using the Rayleigh fractionation equation (which assumes perfect fractionation of crystals and liquid), phase proportions predicted by the major element models, and published trace element partition coefficients (Kds), which are presented in Table 6-1. The concentration of a hypothetical residual melt (C_l) was calculated using successive increments of 5% crystallization of the phases and proportions determined by the major element models for a total of 50% crystallization using the Rayleigh fractionation equation ($C_l=C_0*F^{D-1}$). The initial compositions of trace elements (C_0) were those

of “parent” samples used for major element modeling. The proportions of olivine, plagioclase, and clinopyroxene for each step of crystallization were determined from the PETROLOG results and the bulk distribution coefficient (D) varied based on these mineral proportions (e.g. $D=(x(ol)*Kd_{Zr\ in\ ol})+(x(plag)*Kd_{Zr\ in\ plag})+(x(cpx)*Kd_{Zr\ in\ cpx})$; where x(mineral)=the proportion of crystals of a particular mineral after each 5% increment). The fraction of melt remaining (F) was a constant 0.95. The behavior of Cr, Zr, Y, Sr, and La were modeled for three of the major element fractional crystallization starting compositions. These starting compositions were those of T1012-R08 (B), T1013-R17 (C), and T1011-R2 (E). La, Zr and Y (all very incompatible with respect to MORB phases) concentrations are expected to increase with decreasing (more evolved) MgO contents whereas Cr (compatible in clinopyroxene) and Sr (moderately compatible in plagioclase) are both compatible elements in MORB mineral phases and will have the opposite behavior when cpx and plag begin to crystallize.

The resulting modeled trace element variations are presented in Figure 6-12. While the major element models seemed to fit the lavas from Vance B and C fairly well, fractional crystallization of the presumed parents cannot explain the variations in trace element data for these two seamounts. The calculated LLDs for Cr and Sr fit the data very poorly, although the analytical error for Sr is ±3% and ±5% for Cr, which may explain some of the variation. The high concentrations of Sr in some of the Vance A and B lavas cannot be explained by fractional crystallization, as they follow a different trend than that predicted by fractional crystallization. Lavas from the S. Cleft, however, do follow the trends predicted by the fractional crystallization models (i.e. the concentrations of Sr remain relatively constant with decreasing MgO) (Figure 6-4). The Vance A lavas are too enriched in the most incompatible elements compared to the calculated LLDs and are anomalous compared to the other seamount lavas. The enrichment in

incompatible elements for the Vance A lavas must be inherent to the source and cannot be produced by even extensive amounts of fractional crystallization.

Several parents with similar compositions for each seamount may be required to produce some of the observed variation in trace elements. However, simple models of fractional crystallization do not adequately explain the observed variation in major and trace elements for the Vance Seamounts indicating that other processes must be involved.

Partial Melting

If the Vance Seamount lavas cannot be explained by fractional crystallization, perhaps different extents of partial melting of a similar source can better explain the observed elemental variations. Incompatible trace elements are extremely sensitive to partial melting; the more incompatible the element is, the more sensitive it is to small degrees of partial melting. In melts that have undergone very small extents of melting, there will be a strong enrichment in the most incompatible elements (e.g. the LREE) with respect to the less incompatible elements (e.g. HREE). As the degree of melting increases, the enrichment of the most incompatible to less incompatible elements will become less defined.

Fornari et al. [1988a] and *Leybourne and Van Wagoner* [1991] modeled the effects of partially melting a variety of primitive mantle sources to better constrain the petrogenesis of the Lamont and Heck and Heckle Seamounts. Both used equilibrium batch melting models with similar melting fractions of a depleted lherzolite source. Their results are plotted with the Vance Seamount lavas in Figure 6-13. The lines indicate the modeled partial melting (PM) trends for a depleted lherzolite [*Leybourne and Van Wagoner*, 1991] and a garnet lherzolite with 5% garnet [*Fornari et al.*, 1988a]. The partial melting trends are distinct from those expected from fractional crystallization (Figure 6-13). It is clear that the samples from the Heck and Heckle, Lamont, and Vance Seamounts do not follow fractional crystallization trends, as the lavas from

the Southern Cleft segment do. The Heck and Heckle Seamounts approximate 15-20% partial melting of a depleted lherzolite source, while the Lamont Seamounts approximate 10-20+% partial melting of a garnet lherzolite. The Vance Seamounts are consistent with 5-20% partial melting of a garnet lherzolite. Most of the Vance Seamount lavas (Vance B through G) can be explained by approximately 10-20% partial melting, while the Vance A samples require significantly less (~ 5%) partial melting to explain their more enriched characteristics.

Is it plausible that garnet could be present in the source material for the Vance Seamounts, since it implies that melting of the mantle source for the Vance Seamounts lavas must have began at depths (at least ~80 km) where garnet is stable? Several authors have used residual peridotites (which have been depleted in components that form MOR basalts) to model the effect of partial melting on the source mantle material of typical MORB [*Frey et al.,* 1985; *Hellebrand et al.,* 2002]. Results show that in many cases the trace element geochemistry of the previously melted residues require initial melting in the presence of garnet, followed by subsequent melting in the spinel peridotite field. Other authors have hypothesized the presence of pyroxenite and garnet pyroxenite veins in peridotites, which result in residual major and trace element compositions consistent with melting of these veins [*Frey et al.,* 1985; *Takazawa et al.,* 2000]. *Beattie* [1993] also suggests that MORB must be produced by melting initiated at depths where garnet is stable, due to the fact that the (^{230}Th/^{238}U) of MORB is greater than 1. Values greater than 1 imply that Th is more incompatible than U in MORB petrogenesis, yet experimental results from melting spinel peridotite indicate that partition coefficients for olivine and pyroxene in this ultramafic rock type are smaller for U than for Th (i.e. U is more incompatible when melting spinel peridotite). However, when garnet peridotite is melted, Th behaves more incompatibly than U and the observed ^{232}Th excess in MORB can be produced. Trace element

patterns for the Vance seamounts are consistent with a slight influence of garnet in the concentrations of the HREEs. The depletion of the HREEs relative to the light and middle rare earth elements, while subtle, is evident in the Vance A lavas (crossing patterns of more LREE enriched samples of Vance A, Figure 5-3). These samples are also enriched in the most incompatible trace elements, suggesting an enriched source material, consistent with the veined mantle model of enriched pyroxenite/garnet pyroxenite veins distributed in a depleted peridotite matrix [*Cousens*, 1996a]. While further investigation needs to be carried out in regards to the presence of garnet in the source material for the Vance Seamount lavas, the possibility of at least some melts initiating at depths within the garnet stability field cannot be ruled out.

Elemental variations present in the Vance B through G lavas may not however be simply explained by variable extents of partial melting of a single source. The final parental melt compositions determined by partial melting are highly dependent upon the initial source composition. If the true source material were more depleted than the modeled source compositions, smaller amounts of partial melting would be required to produce the variation in the Vance Seamounts. Alternatively, greater extents of melting of a more enriched source could produce the Vance A lavas. Also, the variation in the Vance Seamount lavas could be produced by more constant extents of melting (versus the 5-20% required by the *Fornari et al*. [1988a] PM model) of sources with compositions that fall close to the partial melting trend.

Small amounts of partial melting of a source that is more enriched in incompatible elements is consistent with the observed incompatible element concentrations (e.g. K_2O, La, Zr) of lavas from Vance A. All of the Vance A lavas also have distinct isotopic values [*Cornejo*, 2008] that suggest a slightly more enriched source material. The correlation of slightly enriched trace element concentrations with distinct isotopic compositions suggests that the Vance A lavas

may not have formed from a lower degree of partial melting of a source that is similar to the other Vance Seamount lavas (which has similar trace element concentrations), but may result from melting of a distinct source (with distinct trace element concentrations). Different extents of partial melting may be the determining factor in the differences *between* the two distinct groups of lavas found on this seamount. The trends of the four more enriched lavas (high K_2O, high LIL, LREE, Zr, Sr) are consistent with lower degrees of partial melting of a source enriched in incompatible trace elements. As the extent of partial melting increases, the concentrations of incompatible elements become more diluted, thus resulting in the lower concentrations present in the two more depleted lavas from Vance A.

Isotopic evidence clearly suggests that there are multiple sources for the Vance Seamounts (i.e. there is significant variation in isotopic values between each seamount and within seamounts; Figures 5-12 to 5-14). Results of major and trace element modeling also suggest that multiple parental compositions (even within an individual seamount) may be required to produce the variation seen in the Vance Seamount lavas. The trend of the Vance Seamount lavas observed in Figure 6-13 may consequently be the result of different sources (or parental compositions) melting to similar extents or the result of mixing between melts from distinct sources. The next section will evaluate the role of mixing in producing the variations observed in the Vance Seamounts.

Mixing and Source Characteristics

In conjunction with trace elements, radiogenic isotopes are a good indicator of source characteristics because the processes of fractional crystallization and partial melting do not affect their compositions. The isotopic ratios of Sr, Pb and Nd are the result of ancient differences in the Rb/Sr, U/Pb, Th/Pb, and Sm/Nd ratios that have developed independently over time. Thus, the radiogenic isotope ratios are unique to a source material within the mantle (particularly at

MOR where crustal contaminants are rare) and are not obscured by shallow level processes that create variability in major and trace elements. However, melt-induced mixing of magmas can affect isotopic ratios.

Cornejo [2008] shows that lavas recovered from the Vance Seamounts have isotopic compositions that range from very depleted (less radiogenic $^{87}Sr/^{86}Sr$ and Pb ratios; more radiogenic $^{143}Nd/^{144}Nd$) to slightly enriched (more radiogenic $^{87}Sr/^{86}Sr$ and Pb ratios; less radiogenic $^{143}Nd/^{144}Nd$) mantle signatures (Figures 5-12 to 5-14). Vance Seamount lava isotopes exhibit a general mixing trend between the more depleted Vance F lavas and the more enriched Vance A lavas.

To evaluate the role of mixing between mantle isotopic sources, two-component mixing calculations were performed between several of the compositional end members. It is important to note that the true sources of the enriched and depleted end members for the Vance Seamount lavas may have isotopic values that are respectively more enriched and more depleted than the observed values, but *Cornejo* [2008] approximates the "depleted" end member as select lavas from Vance F and the "enriched" end member as select lavas from Vance A. Based on this observation, three samples were chosen from Vance F: T1007-R2, T1007-R16, and T1007-R17. Along with having low $^{87}Sr/^{86}Sr$ and Pb ratios and high $^{143}Nd/^{144}Nd$, these samples have very high MgO (8.75-9.33 wt. %) and low concentrations of incompatible trace elements. In particular, T1007-R2 is one of the most primitive samples collected and has the lowest abundances of incompatible trace elements. Two samples were chosen from Vance A: T1008-R20 and T1008-R23. These samples have some of the highest $^{87}Sr/^{86}Sr$ and Pb ratios and low $^{143}Nd/^{144}Nd$. Sample T1008-R23 has some of the lowest MgO (7.25 wt. %) and the highest incompatible trace element abundances (e.g. La = 5.85 ppm) of the Vance Seamount lavas. The

mixing curve [*Vollmer,* 1976; *Langmuir et al.,* 1978] was determined using the isotopic ratios [*Cornejo,* 2008] and elemental abundances (this study) from the selected end member lavas. Four potential mixing models are presented in Figure 6-14. Mix 1 is between T1008-R23 and T1007-R2, Mix 2 is between T1008-R23 and T1007-R16, Mix 3 is between T1008-R20 and T1007-R17, and Mix 4 is between T1008-R20 and T1007-R16.

The Vance Seamount lavas fall along the mixing trends predicted by the four models, with the exception of lavas from Vance B. It is clear that multiple sources for each end member with similar mantle isotopic signatures are required to produce the observed variation. Samples from Vance C, E, and G plot closer the Vance F lavas suggesting that a larger contribution of the "depleted" end member to the mix would result in the observed isotopic values. The Vance B lavas have $^{143}Nd/^{144}Nd$ values that are very different than lavas from the other seamounts in the chain, thus making them plot far from the calculated mixing trends in Figure 6-14. Mixing calculations were not done for Pb isotopes, because the error for these measurements was very high (see Appendix A). However, the Vance lavas seem to follow a mixing trend between the Vance A and Vance F end members in the Pb-Pb plots as well (Figures 5-13 and 5-14). Lavas from Vance B plot closer to these general mixing trends in Pb-Pb plots, but still do not fall close enough to (i.e. are not within error of) any of the other lavas from the Vance Seamounts, suggesting that the source of these lavas is very different than that of the other seamounts.

To look at this trend in a regional context, *Cornejo* [2008] compares isotopic ratios from the Vance Seamounts relative to mantle reservoirs (Figure 6-15). The Vance Seamount lavas fall along a mixing trend between the DM (depleted mantle: the dominant component in MORB sources) and HIMU (high μ, or $^{238}U/^{204}Pb$) mantle reservoirs. The HIMU mantle source is characterized by more radiogenic $^{87}Sr/^{86}Sr$ and Pb ratios and less radiogenic $^{143}Nd/^{144}Nd$ than the

DM. Lavas from Vance A and Vance B have isotopic ratios that are more similar to HIMU values, suggesting a larger contribution of enriched HIMU-like material to these lavas than the Vance C, E, F, and G lavas. The enriched veins (or plums) in the model of the NE Pacific upper mantle proposed by *Cousens,* [1996a] are characterized by more enriched isotopic compositions typical of HIMU along with enriched trace element compositions. Thus, the isotopic geochemistry of the Vance Seamount lavas is consistent with variable mixing of the enriched vein material (typical of Vance A) and the depleted matrix (typical of Vance F).

However, multiple source compositions of these two end members are required to produce the observed variation in isotopic values recovered from the Vance Seamounts (Figure 6-14). It follows that each of these similar, but distinct source compositions not only has a unique isotopic ratio that has developed independently over time, but also unique concentrations of major and trace elements. If we consider the plot of $(Ce/Yb)_N$ versus Ce (Figure 6-13), it is clear that while the isotopes indicate mixing of Vance A and F, trace element variations are not simply explained by mixing of these two end members. Instead, different degrees of partial melting may be affecting the compositions of these unique sources. For example, the source for the Vance C lavas may have initially had trace element concentrations that are similar to the Vance F lavas, but were melted to a greater extent than the Vance F lavas, which produces the observed trace element variation. The Vance C lavas also presumably contain at least a small portion of more enriched lava (typical of Vance A), which may also produce the observed variation in incompatible elements within Vance C (i.e. some lavas from Vance C are slightly more enriched in incompatible trace elements at similar MgO contents, see Figure 5-2 and 6-12). This process is more consistent with some of the observed major and trace element variation than that of fractional crystallization.

For some seamounts (e.g. Vance E and G) differing extents of partial melting followed by small degrees of fractional crystallization seem likely to be involved in producing the major and trace element trends observed. The alternative is that similar extents of melting of multiple compositions (variably depleted or enriched in trace elements) are producing the trend seen in Figure 6-13. Lavas from Vance A are consistent with melting of a source that contains a higher proportion of enriched mantle material (HIMU-like). Vance B lavas have major and trace element compositions that are similar to the rest of the Vance Seamounts, but isotopic compositions that are more similar to compositions from Axial Seamount that lies just north of the Vance chain.

Geochemical modeling of major, trace and isotopic values of the samples collected from the Vance Seamounts indicate that there are complex magmatic processes operating in the formation of lavas from this seamount chain. The very primitive nature and the simple mineralogy of the lavas along with major and trace element modeling argue against fractional crystallization as a dominant process controlling the elemental variations observed in the Vance Seamounts. There is also no physical evidence of magma mixing evident in the seamount lavas; i.e. there are no zoned or resorbed phenocrysts and no xenocrysts present in the lava samples [*Cornejo,* 2008; *Finney,* 1989]. These observations support the model that magmas from near-ridge seamounts do not reside, cool, and fractionate in crustal magma chambers for extended periods of time [*Fornari et al.,* 1988a; *Clague et al.,* 2000]. Variable sources along with different extents of melting of these sources better explains the observed geochemistry of the Vance Seamounts. The variability within individual seamounts may be explained by ineffective mixing (due to the lack of time spent in a magma chamber) of chemically distinct melt pulses resulting from variable extents of melting of a mantle with “enriched” veins in a “depleted” matrix. This

results in chemically distinct major, trace, and isotopic trends both within and between seamounts.

Implications for the Formation of Near-Ridge Seamounts

Geochemical analysis of basalts from the Vance Seamount Chain and nearby off-axis seamounts provides valuable insights into the sources and processes that function at near-ridge seamounts versus those along the ridge axis. The Vance Seamounts likely formed from different degrees of partial melting of a depleted mantle source with variable amounts ("veins") of enriched mantle material (perhaps with garnet?), which then experienced small amounts of low pressure fractional crystallization, finally erupting on the seafloor. Because of short residence time in magma chambers, the seamount lavas essentially rise directly from the mantle with minor amounts of fractionation or mixing, thus giving rise to the variability in major, trace, and isotopic compositions observed between and within individual seamounts in the Vance Chain.

Davis and Karsten [1986] proposed that near-ridge seamounts are the consequence of preferential melting low-temperature, enriched mantle heterogeneities in advance of the migrating ridge axis. This hypothesis requires that the seamount lavas progress from enriched to depleted compositions as you move toward the ridge. The Vance Seamounts do not show this systematic progression, nor do the Heck and Heckle, President Jackson, or Lamont Seamount Chains [*Davis and Clague*, 2000; *Leybourne and Van Wagoner*, 1991; *Fornari et al.*, 1988a]. The data from the Vance Seamounts (and other near-ridge seamounts) supports the hypothesis that the seamounts are the result of a long-lived thermal anomaly that is present in the asthenosphere adjacent to the ridge.

Some authors [*Cousens*, 1996a; *Leybourne and Van Wagoner*, 1991; *Allan et al.*, 1989] have suggested that the direction of regional mantle flow has implications for the extent of enrichment observed at near-ridge seamounts. If the mantle (with imbedded enriched veins in a

depleted matrix) first passes below the ridge, it will be depleted of its more fertile components, leaving behind a mantle depleted of enriched components. Subsequent melting at a near-ridge seamount would then be derived from this already depleted mantle, resulting in lava compositions reflecting this type of mantle source. In the NE Pacific, along the Juan de Fuca Ridge, the mantle flows from east to west, from the Juan de Fuca Plate to the Pacific Plate [*Cousens,* 1996a]. It follows that lavas from the Vance Seamounts should have depleted lava compositions. This does not seem to be the case for the Vance Seamounts. The depleted Heck and Heckle Seamount lavas may be consistent with this hypothesis, but the more varied and enriched compositions of the Vance and President Jackson Seamounts indicate that the seamounts are not tapping regions of the mantle that have been previously melted at the ridge. Three of the JdFR Seamounts discussed in this thesis are located on the Juan de Fuca Plate, while one of the seamounts along with the Vance Seamount Chain are located on the Pacific Plate. There are no systematic differences between the trace element concentrations of the seamounts located on the east and west sides of the JdFR. Instead, the melting anomaly forming the Vance Seamounts may be the result of deeper melting, tapping mantle sources that have not been previously melted beneath the ridge [*Desonie and Duncan,* 1990]. The observation that the Vance Seamounts may have been produced from different extents of melting of a mantle source that contains garnet also supports the idea that deeper melting (or at least some melts originating at depth) may result in the geochemistry found at these seamounts. The similarity of isotopic values from Vance B to those of Axial Seamount, an expression of the Cobb Hotspot on the Juan de Fuca Ridge, suggests that at least the Vance B lavas may result from deeper melting, although perhaps not as deep as mantle plumes are proposed to originate.

It is clear that near-ridge seamounts are much more useful in revealing the heterogeneity present in the upper mantle than the ridge. The origin and formation of near-ridge seamounts is a question that remains open to further investigation. More data from the Vance Seamounts as well as further investigation into the degree and style of partial melting that these samples undergo would be useful in constraining the origin of the Vance Seamount lavas (particularly those from Vance A and B).

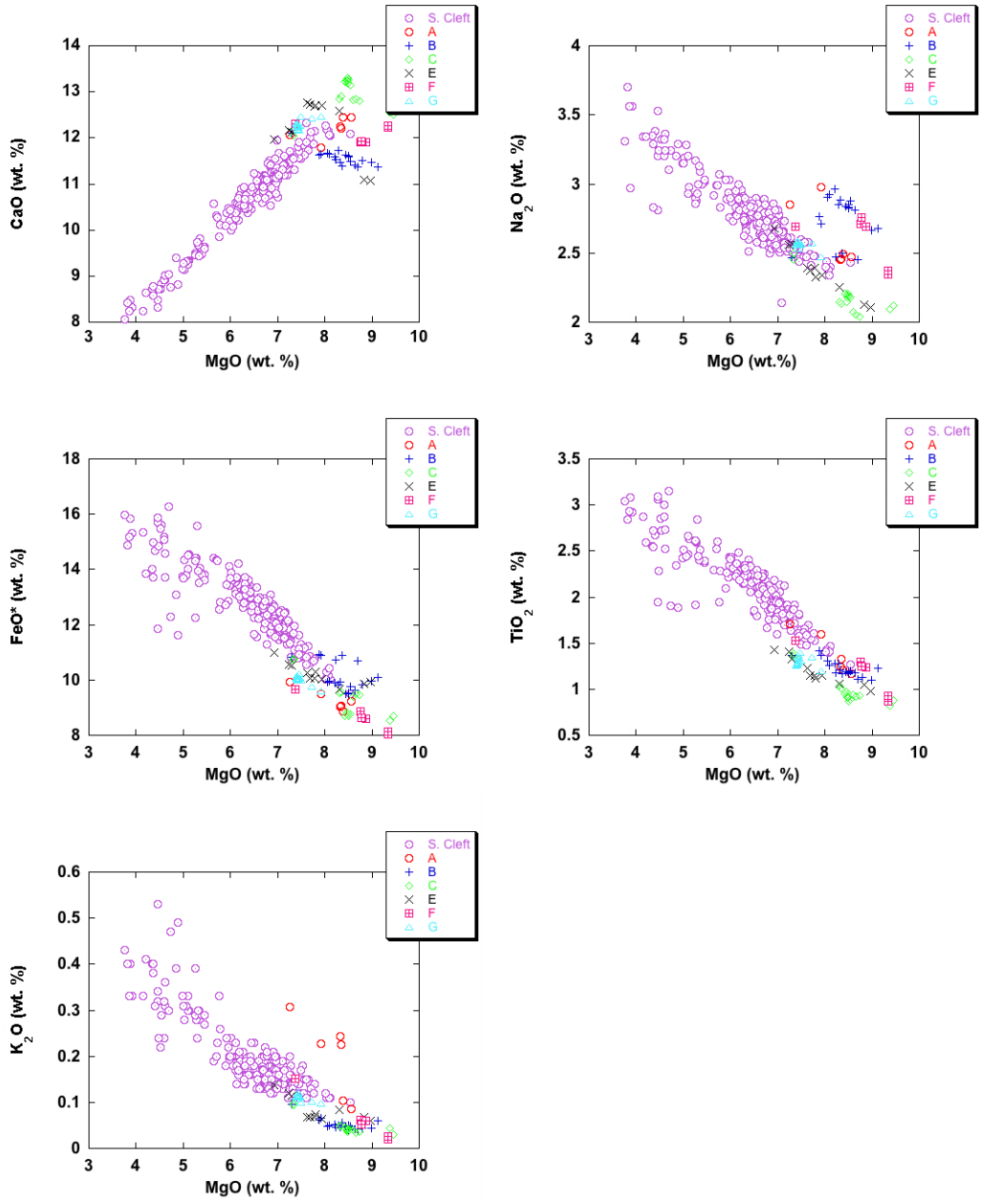

Figure 6-1. Select major elements from the Vance Seamounts (D. Clague, personal communication) and representative on-axis lavas from the Southern Cleft (S. Cleft) Segment of the Juan de Fuca Ridge (see text for data sources).

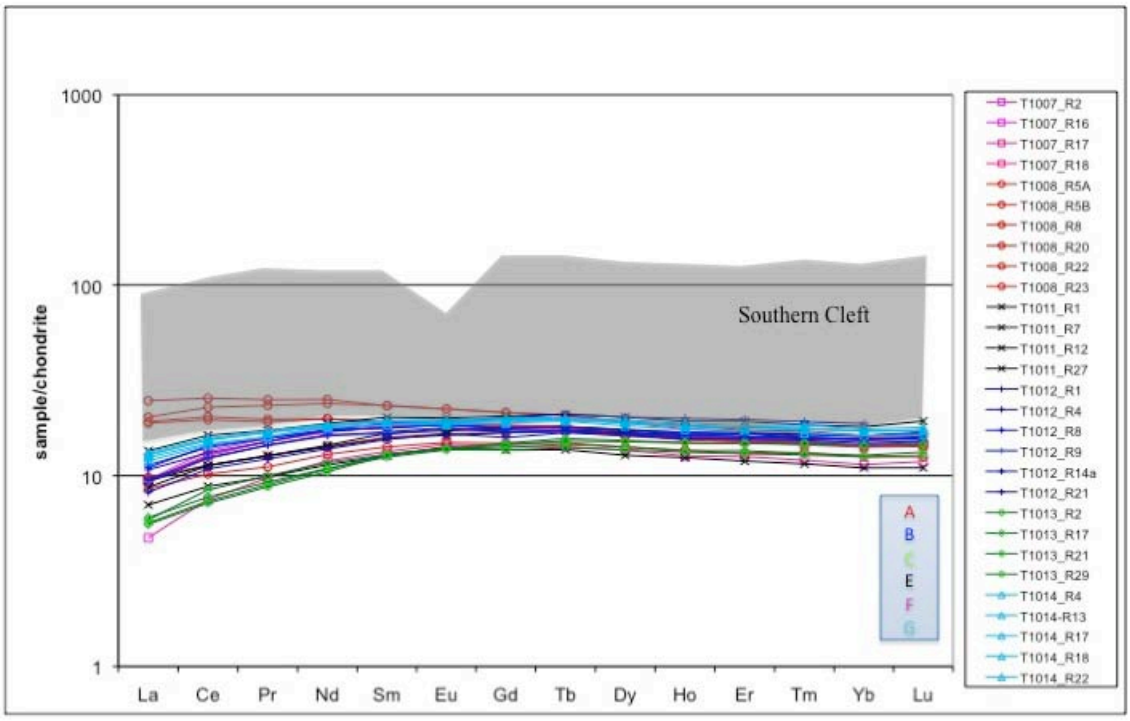

Figure 6-2. Chondrite normalized [*Sun and McDonough*, 1989] rare earth element patterns for Vance Seamounts with representative on-axis field from the Southern Cleft (S. Cleft) Segment of the Juan de Fuca Ridge (see text for data sources).

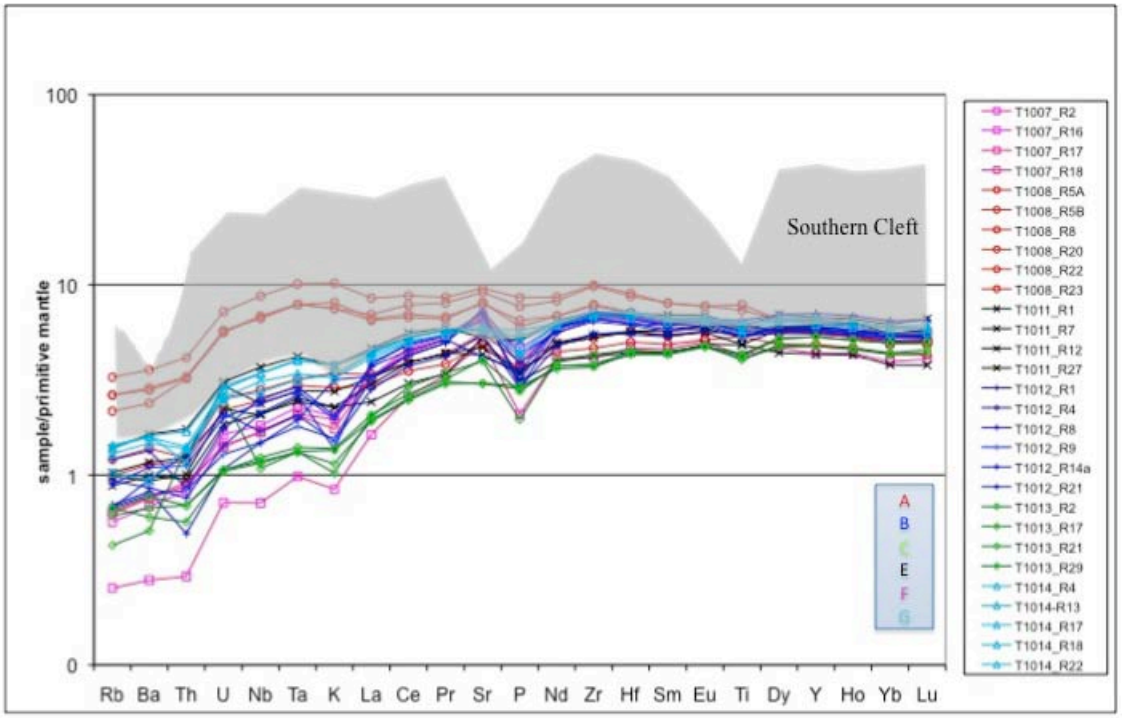

Figure 6-3. Primitive mantle normalized [*Sun and McDonough*, 1989] trace element patterns for Vance Seamounts with representative on-axis field from the Southern Cleft (S. Cleft) Segment of the Juan de Fuca Ridge (see text for data sources).

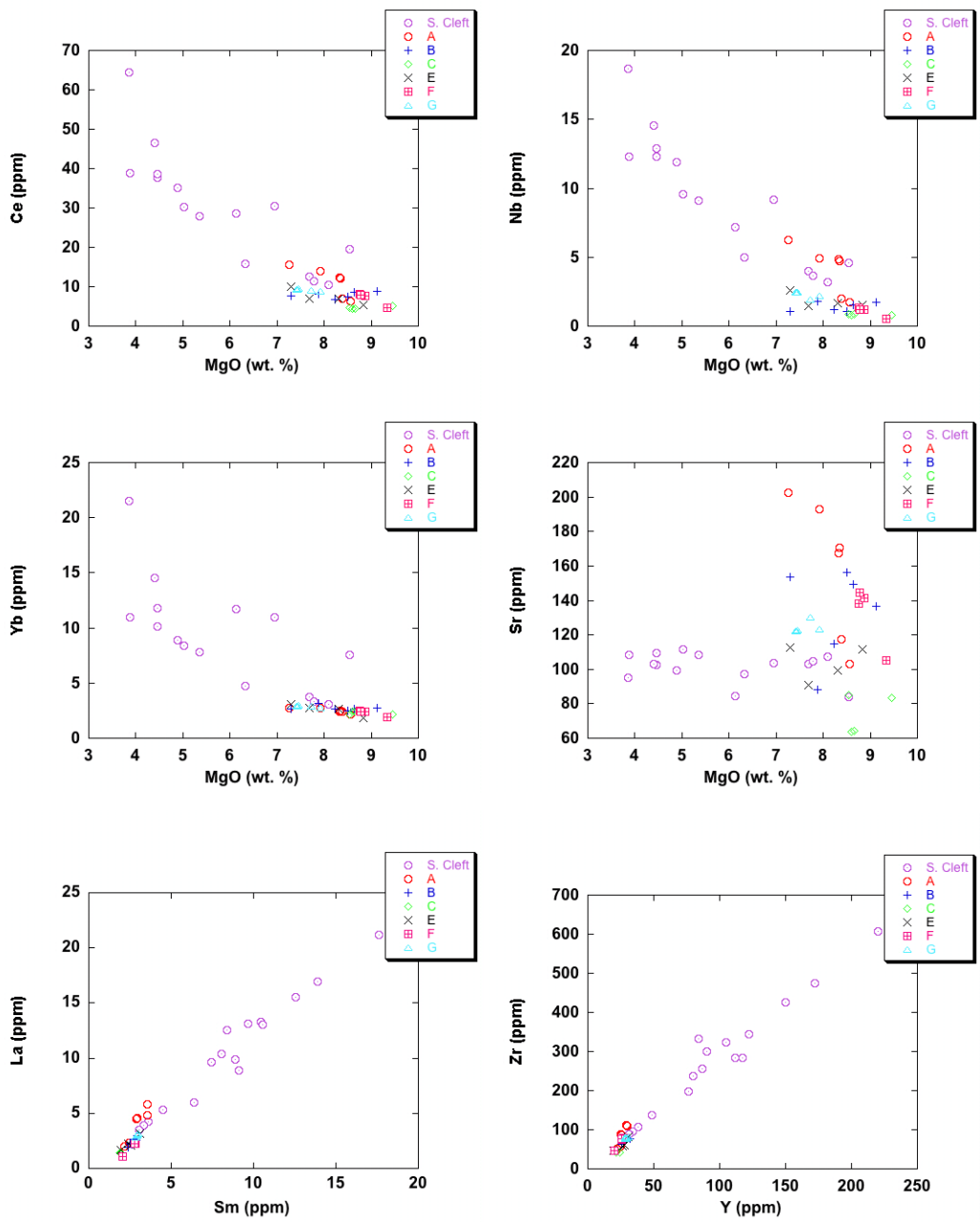

Figure 6-4. Select trace element concentrations of the Vance Seamounts and representative on-axis lavas from the Southern Cleft (S. Cleft) Segment of the Juan de Fuca Ridge (see text for data sources). Major element data provided by D. Clague (personal communication).

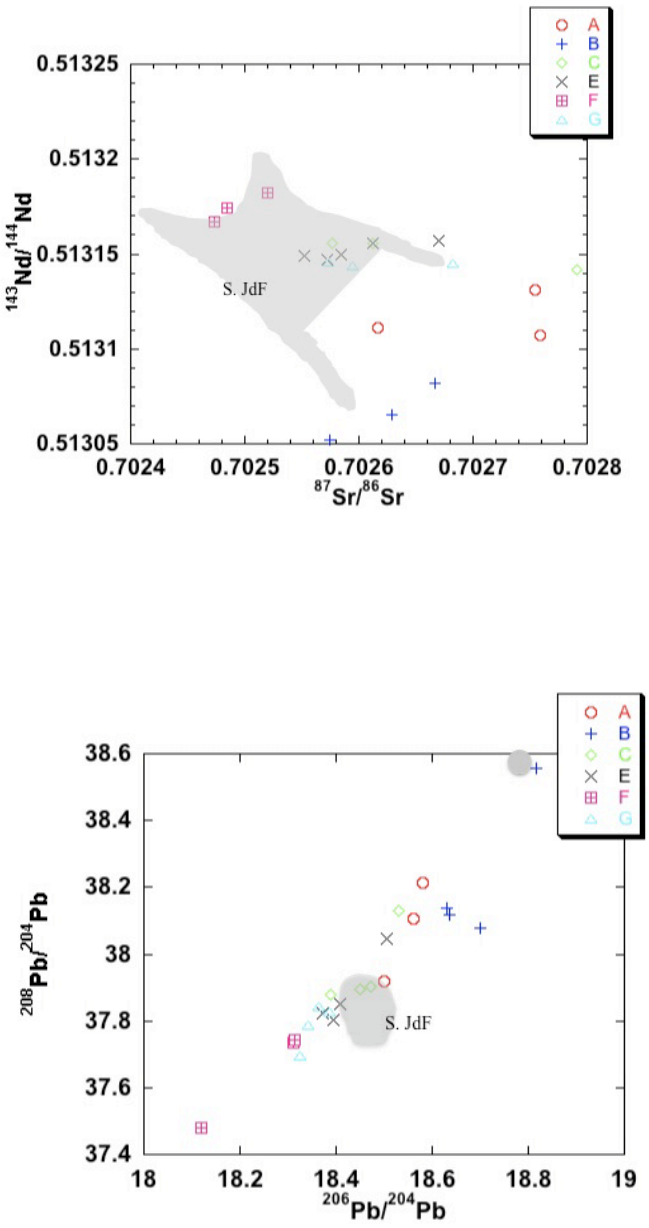

Figure 6-5. Isotopic ratios for the Vance Seamounts [*Cornejo,* 2008] plotted with representative on-axis lavas from the Southern Juan de Fuca Ridge (see text for data sources).

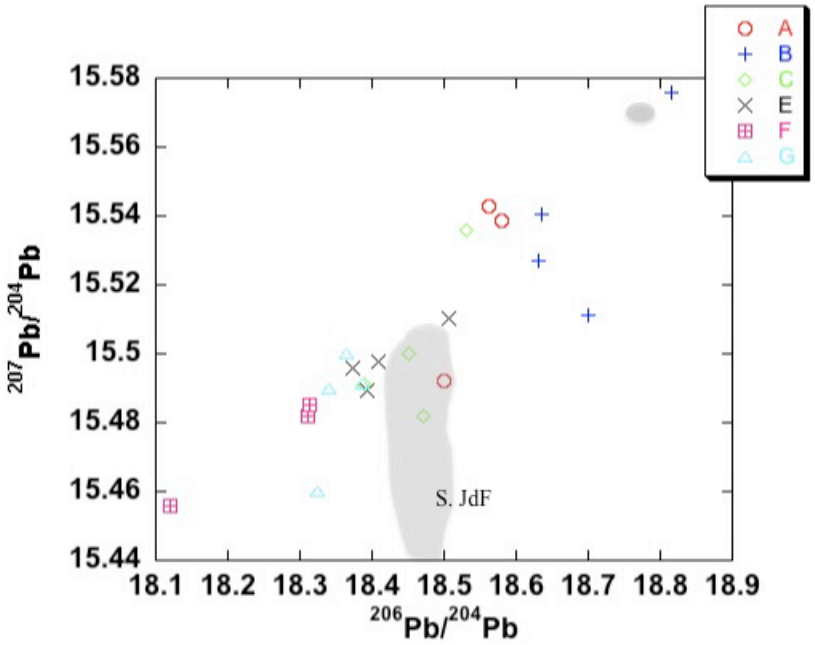

Figure 6-5. Continued.

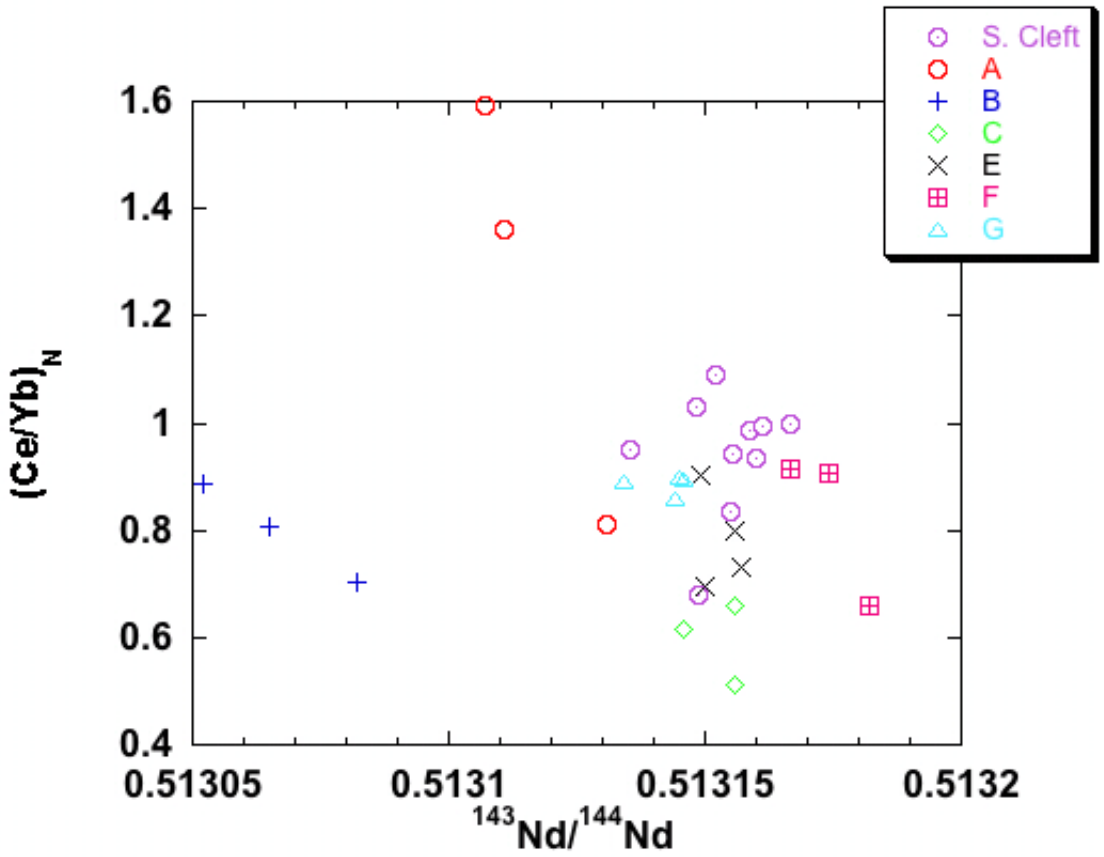

Figure 6-6. Chondrite normalized [*Sun and McDonough*, 1989] $(Ce/Yb)_N$ versus $^{143}Nd/^{144}Nd$ [*Cornejo*, 2008] for the Vance Seamounts and lavas from the Southern Cleft Segement (S. Cleft) of the Juan de Fuca Ridge (see text for data sources).

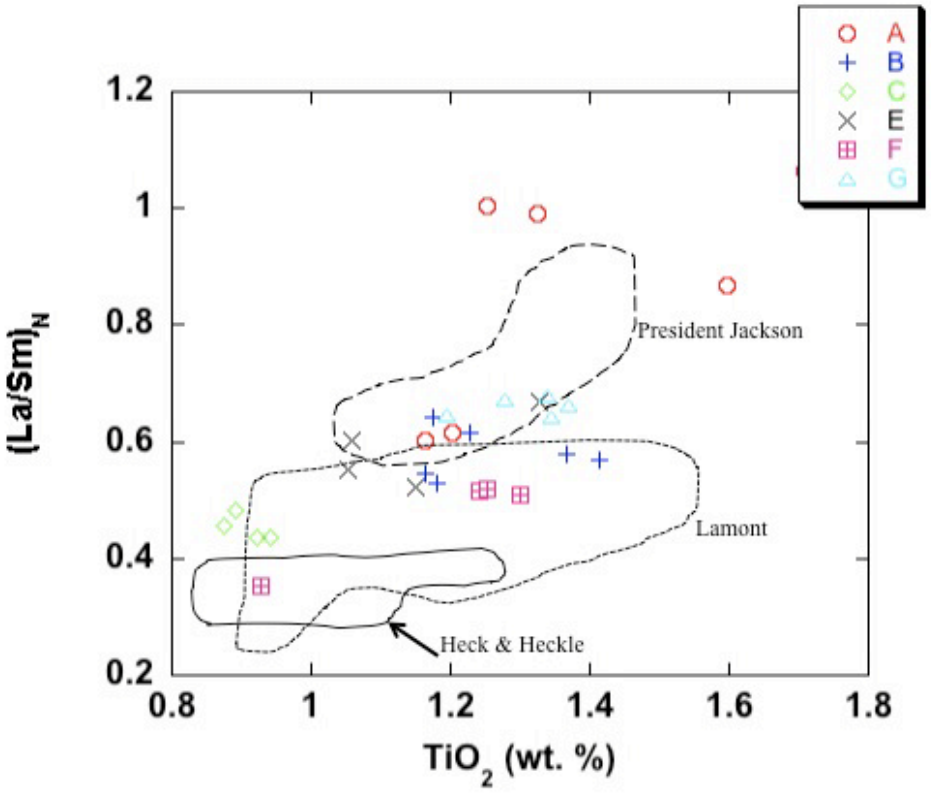

Figure 6-7. Chondrite normalized [*Sun and McDonough*, 1989] $(La/Sm)_N$ versus TiO_2 (D. Clague, personal communication) for the Vance Seamounts and lavas from the Heck and Heckle [*Leybourne and Van Wagoner*, 1991], President Jackson [*Davis and Clague*, 2000], and Lamont Seamounts [*Fornari et al.*, 1988a].

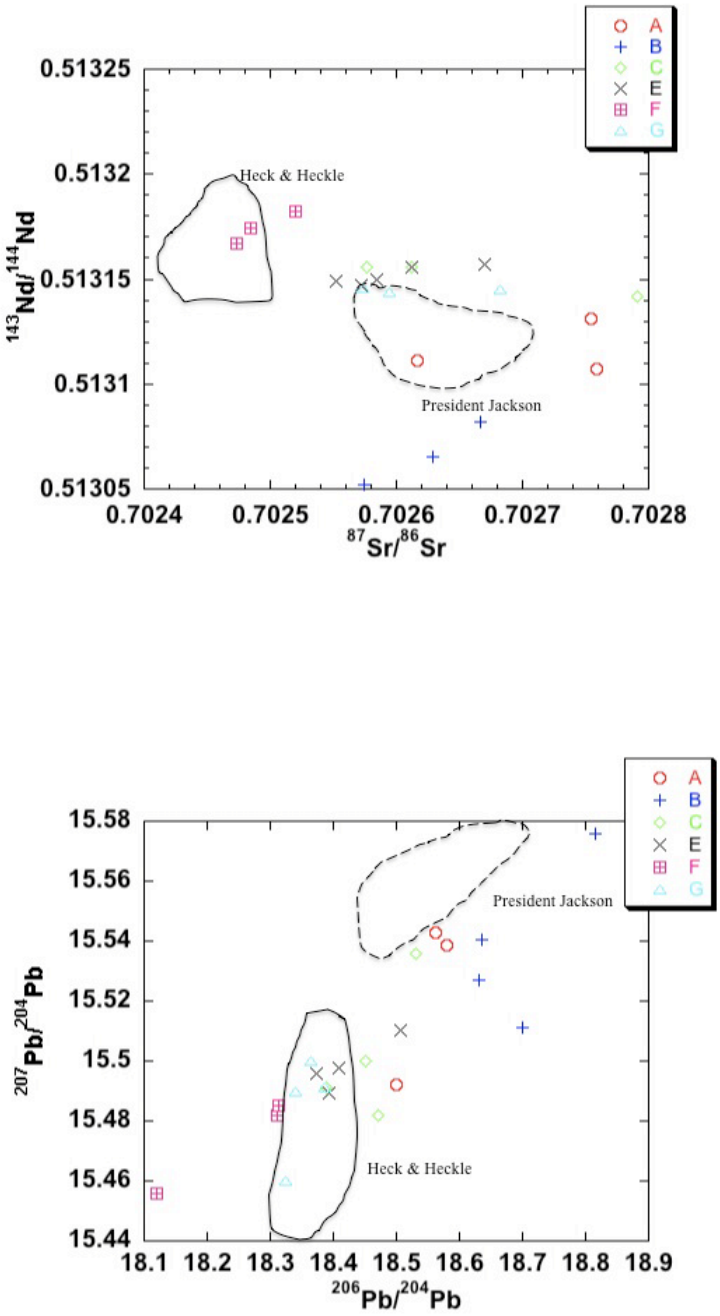

Figure 6-8. Select isotopic ratios of the Vance Seamounts [*Cornejo*, 2008] and lavas from the Heck and Heckle [*Leybourne and Van Wagoner*, 1991] and President Jackson Seamounts [*Davis and Clague*, 2000].

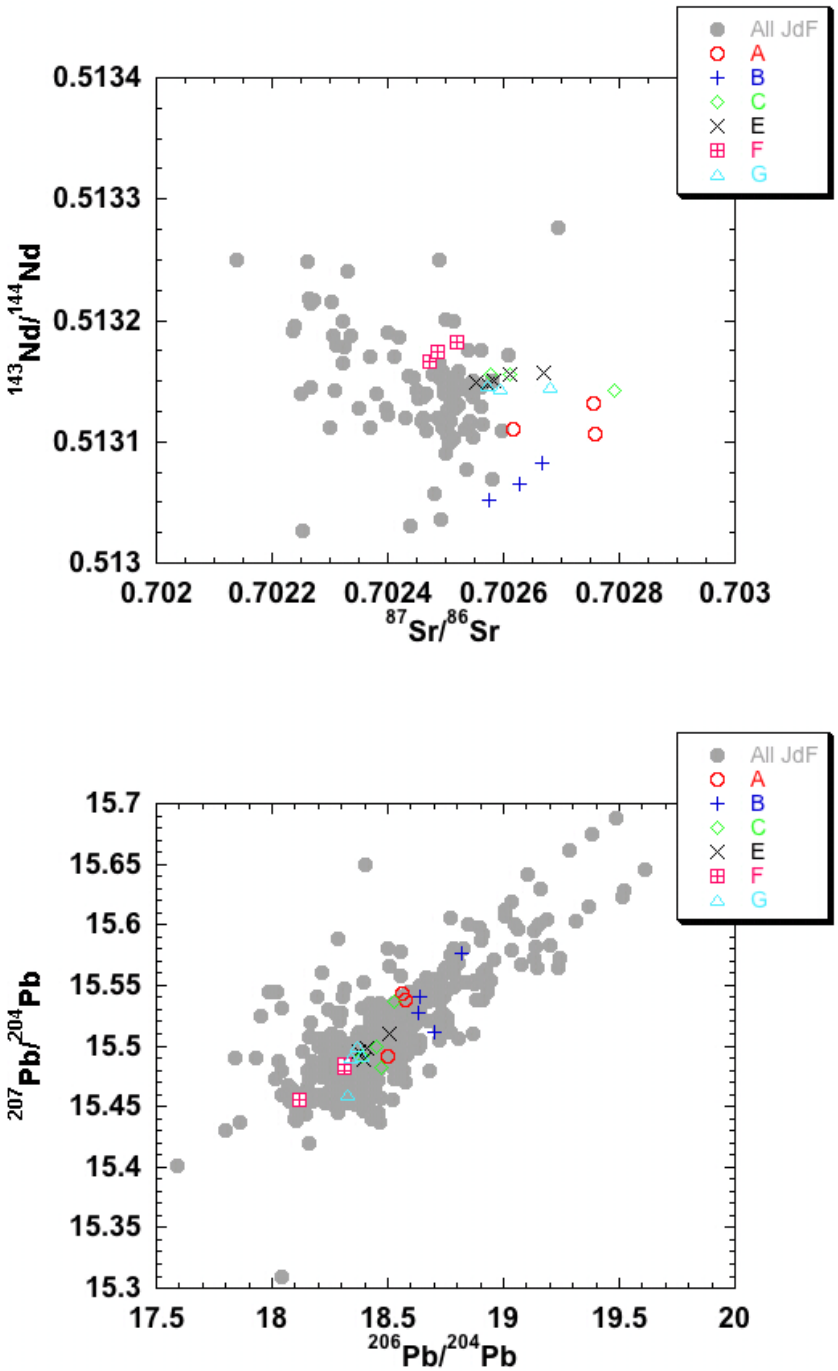

Figure 6-9. Select isotopic ratios from the Vance Seamounts [*Cornejo*, 2008] and samples from the large Juan de Fuca data set (see text for data sources).

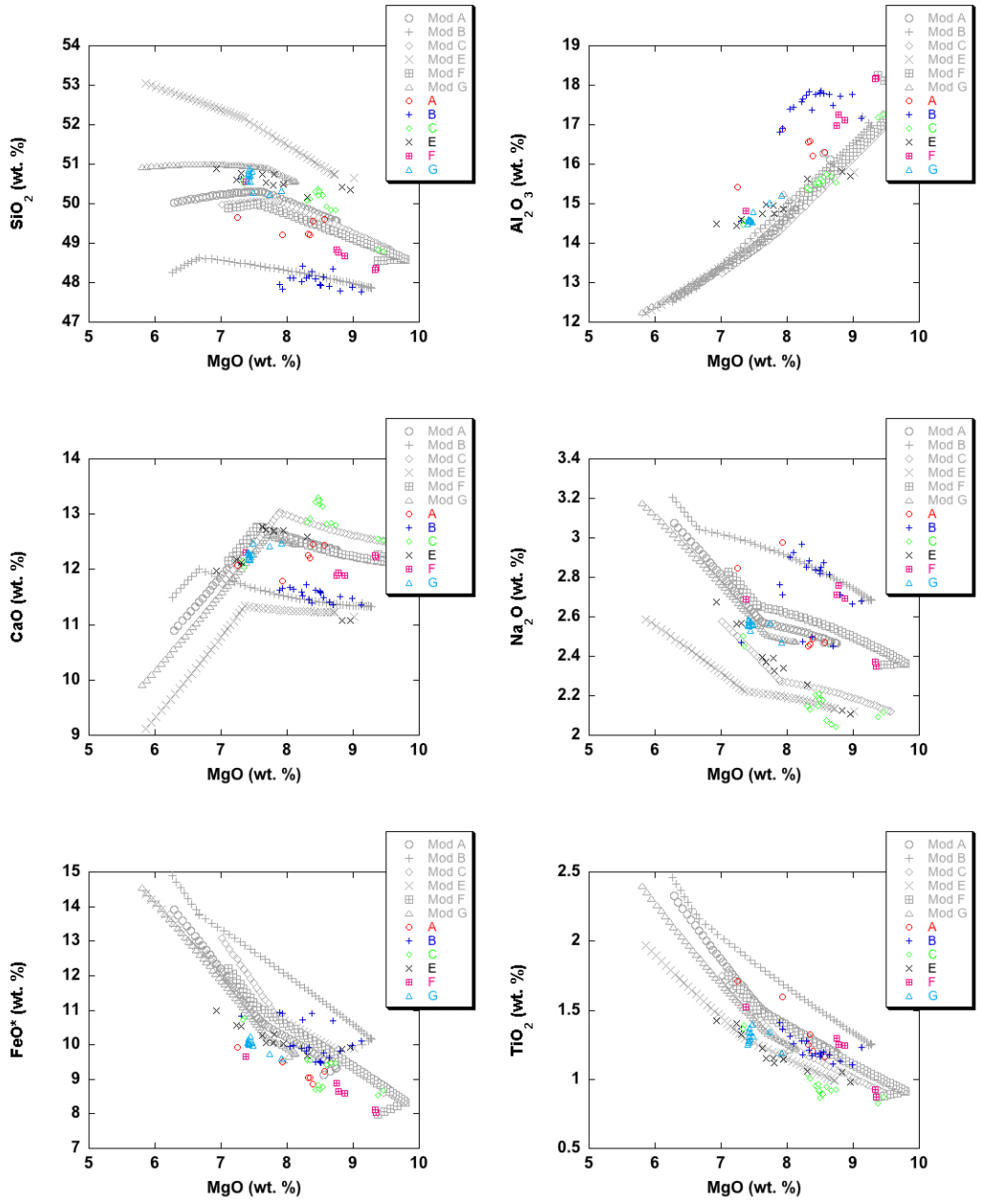

Figure 6-10. Liquid lines of descent (LLDs) for select major elements as calculated using the program PETROLOG. LLDs are labeled "Model A (Mod A)" through "Model G (Mod G)" and have starting compositions respective to the designated seamount. Major element data provided by D. Clague (personal communication).

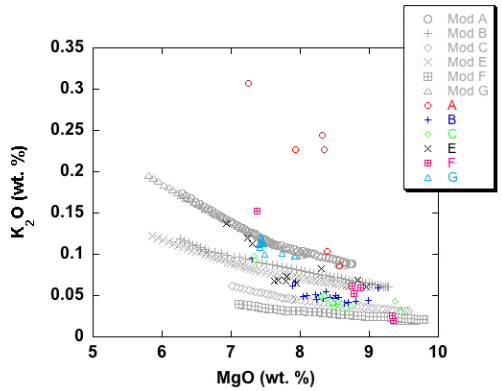

Figure 6-10. Continued.

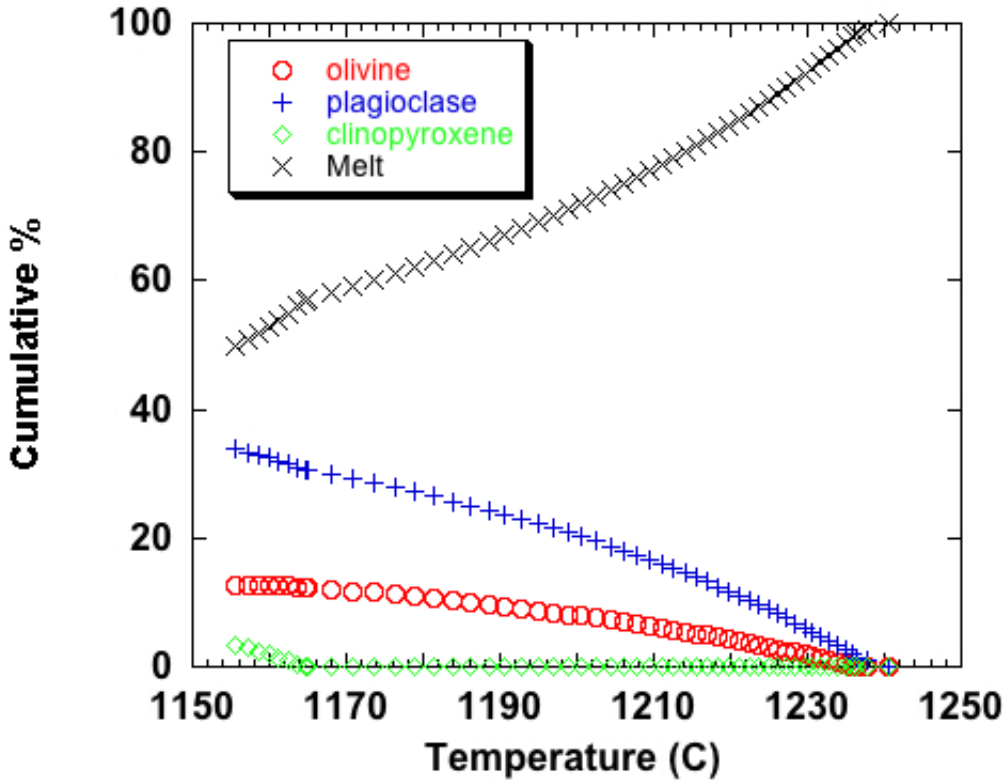

Figure 6-11. Cumulative percentage of phases plotted against melt temperature (°C). This figure illustrates the changing mineral assemblage as the modeled parent composition cools. Model assumes QFM and 1 kbar of pressure.

Table 6-1. Mineral/melt partition coefficients (Kds) used for trace element modeling.

Element	Mineral	Rock Type	Kd	Reference
Sr	olivine	basalt	0.014	1
	clinopyroxene	basalt	0.06	1
	plagioclase	basalt	1.83	1
Y	olivine	basalt	0.01	1
	clinopyroxene	basalt	0.9	1
	plagioclase	basalt	0.03	1
Zr	olivine	basalt	0.012	1
	clinopyroxene	basalt	0.1	1
	plagioclase	basalt	0.048	1
La	olivine	basalt	0.0067	2
	clinopyroxene	basalt	0.056	2
	plagioclase	basalt	0.19	2
Cr	olivine	basalt	0.7	1
	clinopyroxene	basalt	34	1
	plagioclase	basalt	0	1

Reference (1): Compilation of *Arth* [1976]; *Pearce and Norry* [1979]; *Green et al.* [1989]; *Schock* [1979]; *Fujimaki et al.* [1984]; *Dostal et al.* [1983]; *Henderson* [1982]; *Leeman and Lindstrom* [1978]; *Lindstrom and Weill* [1978]; *Green and Pearson* [1987]. Reference (2): *Fujimaki et al.* [1984].

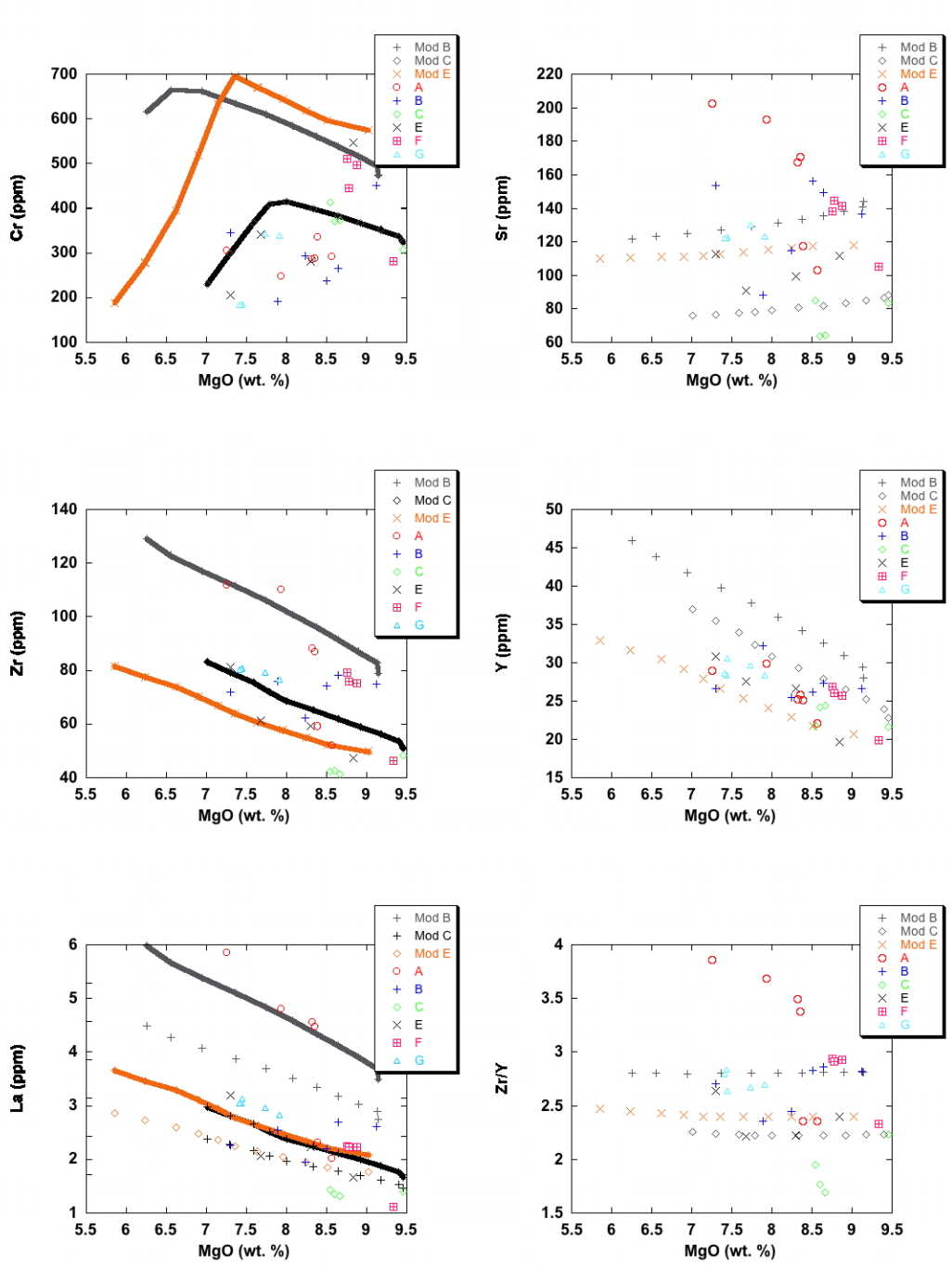

Figure 6-12. Liquid lines of descent (LLDs) for representative trace elements calculated using PETROLOG results and the Rayleigh fractionation equation.

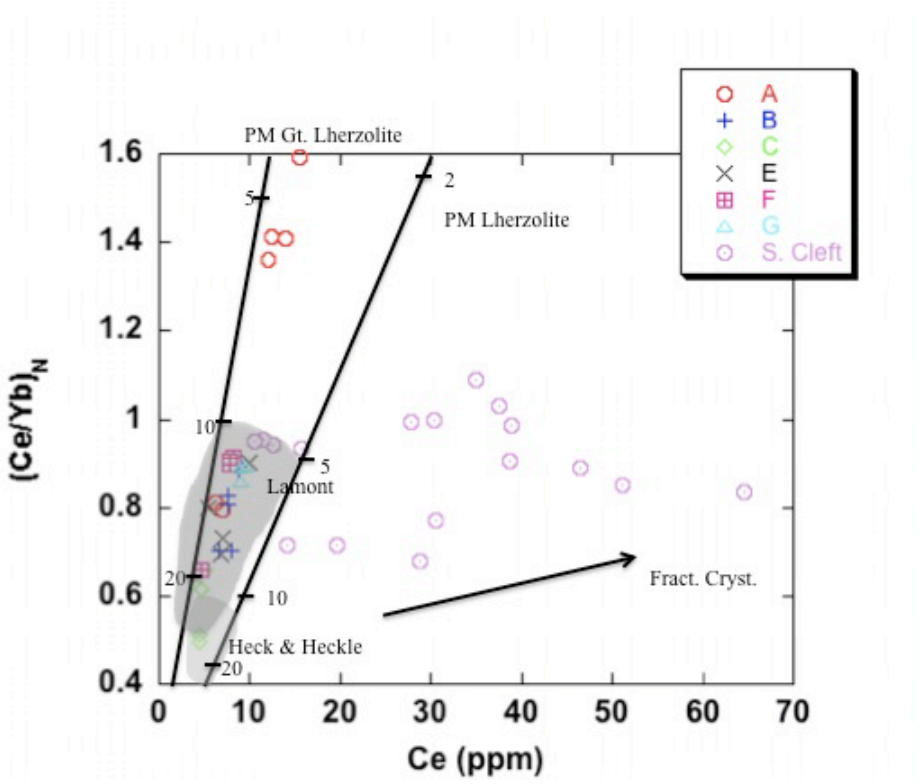

Figure 6-13. Chondrite normalized $(Ce/Yb)_N$ versus Ce (ppm) for the Vance Seamount lavas. Lines with tick marks represent concentrations of partial melting models at various extents (5%, 10%, 20% etc.) for a depleted lherzolite [*Leybourne and Van Wagoner*, 1991] and a 5% garnet lherzolite [*Fornari et al.*, 1988a]. Also indicated is the trend of fractional crystallization, which the S. Cleft lavas follow. The light gray filed represents lavas from the Heck and Heckle Seamounts and the dark gray field represents lavas from the Lamont Seamounts.

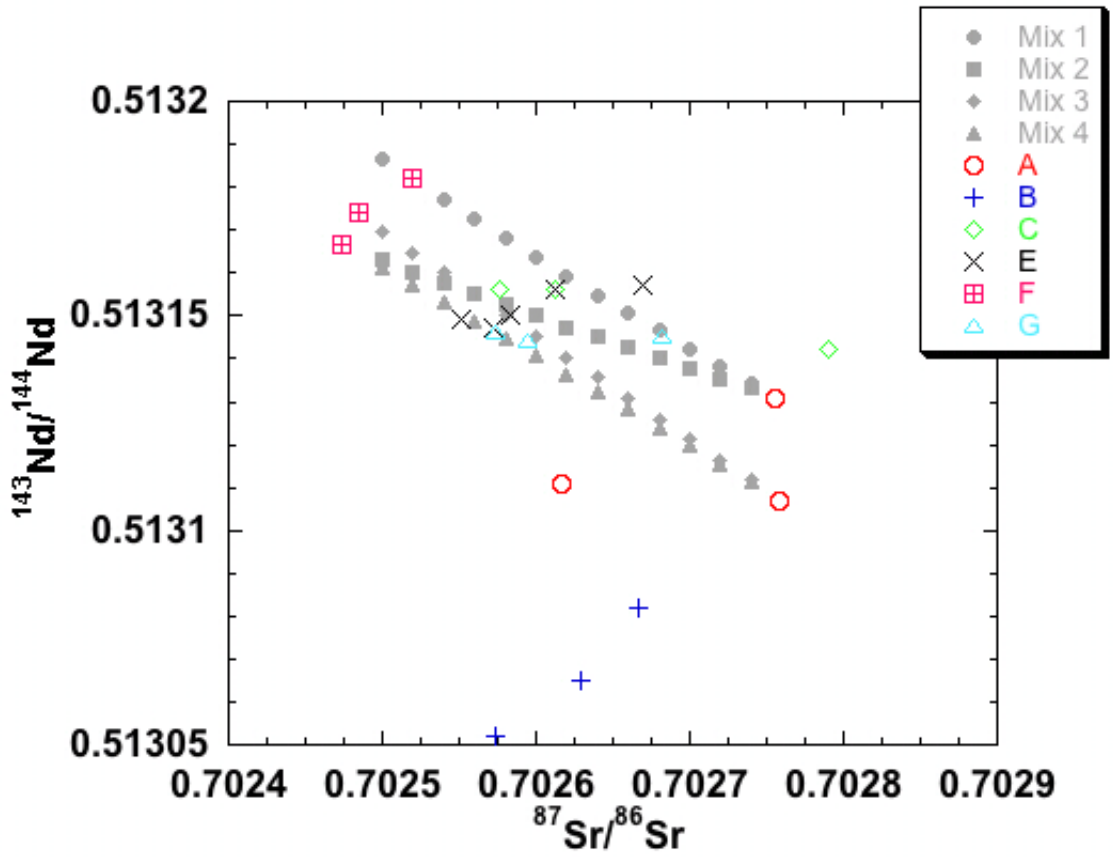

Figure 6-14. Mixing models calculated using a two component mixing equation [*Vollmer*, 1976; *Langmuir et al.*, 1978] plotted with isotope data for the Vance Seamounts [*Cornejo*, 2008]. Potential mixing lines plotted in grey; Mix 1: T1008-R23 and T1007-R2, Mix 2: T1008-R23 and T1007-R16, Mix 3: T1008-R20 and T1007-R17, Mix 4: T1008-R20 and T1007-R16.

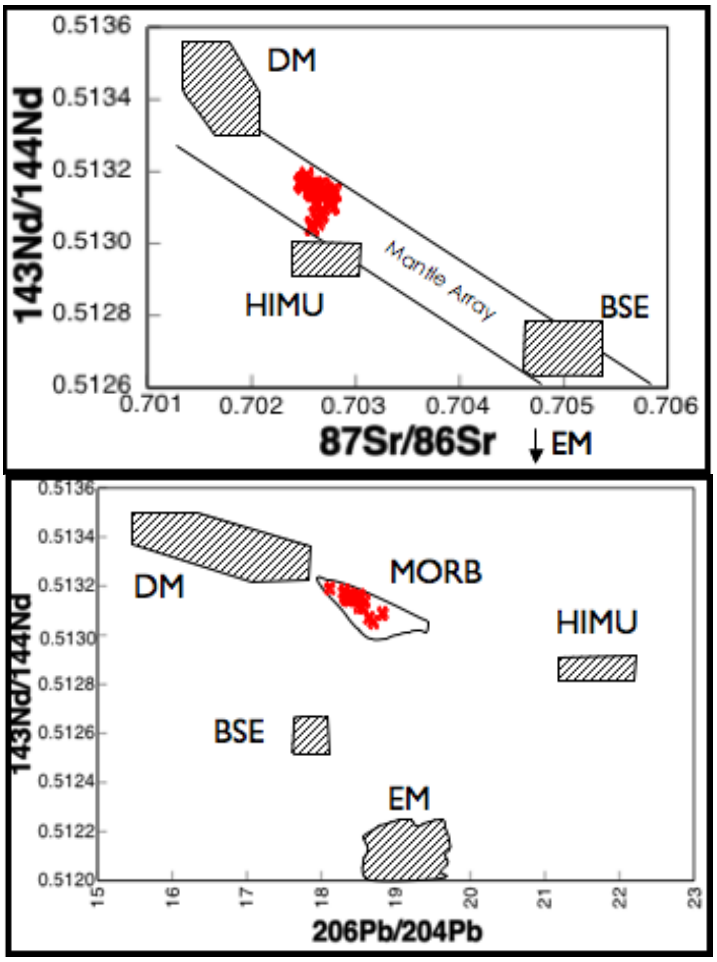

Figure 6-15. The $^{87}Sr/^{86}Sr$ versus $^{143}Nd/^{144}Nd$ and $^{143}Nd/^{144}Nd$ versus $^{206}Pb/^{204}Pb$ showing the Vance Seamount lava compositions (in red) [*Cornejo*, 2008] in reference to the mantle components of Zindler and Hart (1986) (lined boxes), modified from Rollinson (1993). BSE, bulk silicate earth; DM, depleted mantle; EM, enriched mantle; MORB, mid-ocean ridge basalt (as compiled by Saunders *et al.*, 1988). Figure courtesy E. Cornejo [2008].

CHAPTER 7
CONCLUSIONS

The Vance Seamounts have significant geochemical differences in lava composition as compared to the ridge axis, as compared to each other, and in some cases, within individual seamounts. Similar relationships in geochemical variation and their relationship to axial lavas are observed at other near-ridge seamounts.

This diversity is not consistent with extensive amounts of fractional crystallization This supports the hypothesis that near-ridge seamount lavas don't reside, cool, and fractionate long in crustal magma chambers, as is the case with axial lavas.

Melt-induced mixing of depleted (Vance F) and enriched (Vance A) end members produces isotopic variety, except Vance B. Multiple source compositions of these two end members (with unique major and trace element compositions) are most likely required to produce observed variations in between seamounts in the Vance Chain. Isotopic sources for Vance B may be related to sources from Axial Seamount.

Differing extents of partial melting (in conjunction with mixing) of these multiple sources (at depths within the garnet stability field) OR similar extents of melting of different, but similar sources (with variably enriched or depleted in trace elements) can produce trends in trace element data.

Observations from the Vance Seamounts support the model proposed by *Cousens* [1996a] that the upper mantle in the NE Pacific is composed of variable amounts of enriched (HIMU-like) veins (similar to Vance A lavas) within a depleted peridotite matrix (similar to Vance F lavas). The variability *within* individual seamounts may be explained by ineffective mixing of chemically distinct melt pulses resulting from variable extents of melting of a veined upper mantle.

Variability of lavas from the Vance Seamounts supports observations from other authors [e.g. *Fornari et al.,* 1988a; *Leybourne and Van Wagoner,* 1991; *Davis and Clague*, 2000] that the mantle is heterogeneous on a small scale and that these heterogeneities are more easily observed at near-ridge seamounts than at the ridge axis.

It is clear that the lavas from the Vance Seamounts have a complex petrogenetic history.

Investigation into near-ridge seamount chains has indicated that they can be important indicators of dynamics in the mantle. The controls on formation and location of near-ridge seamounts (including their depth of origin) are questions that still remain open to investigation.

APPENDIX A
ACCURACY AND PRECISION

E2 ICP-MS Analytical Protocol

The following dissolution and analytic procedure for trace element analysis was refined by George Kamenov at the University of Florida (UFL) and references the class 1000 clean lab facility and Element II ICP-MS at UFL.

DISSOLUTON PHASE 1

1. 4-5 standards of similar chemical composition to the Vance samples were chosen (e.g., for MORB analysis we chose four certified rock standards [AGV-1, BHVO-1, BIR-1 and BCR-2] and two in-house MORB standards [ENDV and 2392-9]).
2. A tall (6 ml) hex-cap Savillex teflon vial was cleaned and labeled for each sample and standard, including a blank.
3. In the balance room, 1 drop of 4x water was added to a labeled vial (only necessary for rock powders) and the balance was zeroed. Then 40-50 mg of the sample/standard rock powder or glass chips was weighed into the vial. The sample weight was recorded precisely. The process was repeated for the remaining samples, standards, and blank.
4. In the hood, 1 mL trace-metal or optima grade concentrated *HF and 2 mL trace metal optima grade concentrated *HNO_3 was added to each vial. Each vial was then tightly capped.
5. Vials were heated in the oven in the outer room at 100ºC for 24-48 hours. Once each sample was in solution, they were removed from the oven and allowed to cool.
6. Once cool, each sample was dried down (evaporated) on the hot plate (set to no higher than 3.0) by first carefully swirling the sample to collect drops from the sides and lid. Each vial was then placed onto a hot plate for 12-24 hours.

DISSOLUTION PHASE 2

1. 4mL 5% HNO_3 spiked with Re and Rh was added (recording the acid weight) to each vial. The vials were capped and tightened. Non-spiked 5% HNO_3 was added to the blank.

2. The vials were heated on the hot plate at 3.0 overnight.

DILUTION FOR ANALYSIS

1. 200 mL of solution was transferred from each sample vial into an autosampler tube (the weight of sample solution transferred was precisely recorded).

2. 4 mL of 5% HNO_3 spiked with Re and Rh was added to each tube. For the blank, 4 mL of non-spiked 5% HNO_3 was used. This resulted in final dilution around 2000x.

ANALYSIS BY ICP-MS USING THE ELEMENT II

1. The samples and standards were arranged in the autosampler. According to this arrangement, the sequence file was compiled in the sequence editor program.

2. The Method file, Tune file, Internal standard file, weights, and dilutions were each entered accordingly.

3. 1 minute uptake time and 2 minutes wash time per sample were set.

4. All selected elements were analyzed in Medium Resolution mode; 4 runs and 4 passes per analyses (total 16 measurements per isotope). The specific isotopes used were: Li7, B11, Sc45, Ti49, V51, Cr52, Co59, Ni60, Cu63, Zn66, Ga69, Rb85, Sr88, Y89, Zr90, Nb93, Rh103, Cs133, Ba138, La139, Ce140, Pr141, Nd143, Sm149, Eu153, Gd157, Tb159, Dy163, Ho165, Er166,

Tm169, Yb172, Lu175, Hf178, Ta181, Re185, Pb208, Th232, U238. All isotopes lighter than Ba were normalized to Rh, while all isotopes heavier than Ba were normalized to Re.

5. In addition, a drift monitor was run every 5-6 samples. (e.g., we chose 2392-9 to be our drift monitor).

6. Data was normalized ON and OFF line, first in the Results Editor by checking the calibration curves, then using Microsoft Excel using drift corrections. If a total of 4 drift monitors were used (DC1, DC2, DC3, DC4), the first two, middle two, and last two drift correctors for each element were subtracted from each other (DC1and2, DC2and3, DC3and4). The total number of samples measured between each set of drift correctors was noted (N1and2, N2and3, N3and4). The correction applied to each element measured for the first set of samples between DC1 and DC2 (Corrected value=Old value*[1- [DC1and2*[position of sample between drift correctors /N1and2]]) is be different than the middle set of samples between DC2 and DC3 (Corrected value=Old value*[1-DC1and2]*[1-[DC2and3*[position of sample between drift correctors/N2and3]]]), and the last set of samples between DC3 and DC4 (Corrected value=Old value*[1-DC1and2]*[1-DC2and3]*[1- [DC3and4]*[position of sample between drift correctors /N3and4]]]).

Precision and Accuracy

By monitoring the measured concentrations of sample standards, in particular the in-house standard 2392-9 over several different runs on the Element 2, accuracy and precision for the data was evaluated. The accepted trace element concentrations for 2392-9 correlate well (with an R^2 value of 0.997) with the concentrations measured from 2006 to November 2007 on the Element 2 (Figure A-1). If we compare the measured values from each run to the accepted value for 2392-9, we can determine how close the measurements on the Element 2 are to actual values (Table A-1). Accuracy is within ±2% for Sc, V, Sr, Sm, and Hf; within ±3% for Co, Ni,

Ga, Dy, and Er; within ±5% for Cu, Nb, La, Eu, Tb, Ho, Tm, Yb, and U; and within ±10% for Cr, Zn, Rb, Y, Zr, Ba, Ce, Pr, Nd, Gd, Lu, and Th. There is large variability between the measured Pb values in the Vance samples analyzed and the accepted values for the standards; thus it was excluded from the data set in this study. It was determined that the variability in Pb values was not due to natural variability in the samples, but due to the low concentrations of Pb which was consequently diluted during sample preparation. This dilution resulted in extremely low abundances that were easily contaminated or masked by the 2392-9 signal.

Precision for each element measured was also calculated from the multiple analyses of 2392-9 as an unknown. The average and standard deviation of these multiple analyses is used to determine a percent error for each element and is presented in Table A-2. Precision is better than ±2 relative percent for Sc, V, Co, Cu, Sm, Gd, Tb, Er, and Yb; better than ±3% for Ni, Ga, Sr, Eu, Dy, Ho, Tm, Lu, and Hf; better than ±5% for Cr, Zn, Y, Zr, Nd, Nb, La, and Ce; and better than ±10% for Rb, Pr, Ta, Th, and U.

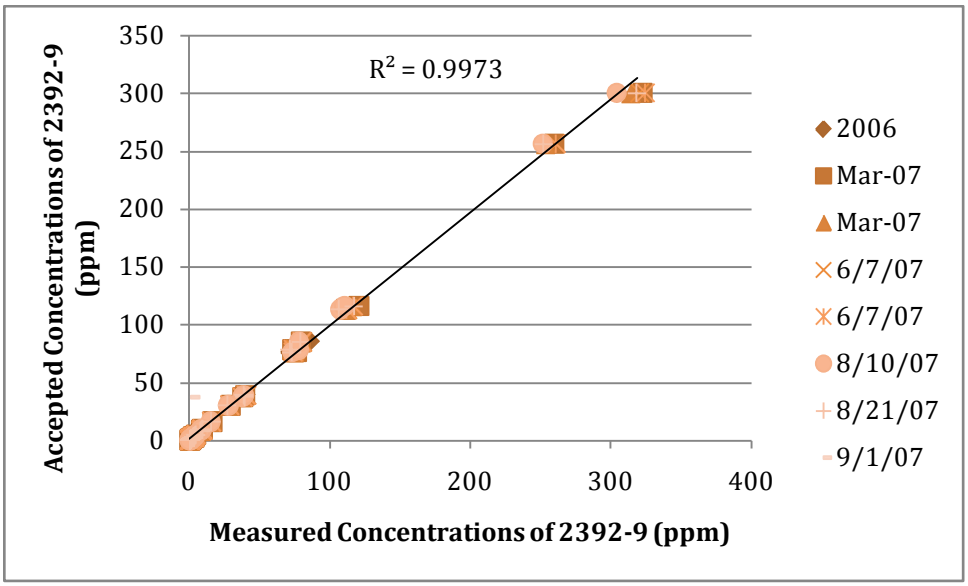

Figure A-1. Measured versus accepted concentrations of the in-house standard 2392-9 in ppm used for evaluation of accuracy and precsion of trace element analyses. Several analyses of the standard from 2006 to 2007 correlate well with the accepted values, with an R^2 value of 0.997.

Table A-1. Percent errors (i.e. accuracy of the measurements) for the in-house standard 2392-9 for each trace element in 8 different runs from 2006 to 2007. Percent error is calculated by (|measured value- true value|/true value)*100.

	2006 % error	Mar-07 % error	Mar-07 % error	7-Jun % error	7-Jun % error	10-Aug % error	21-Aug % error	1-Nov % error	AVG	STDEV
Sc	1.066	0.712	0.691	0.865	1.074	0.176	4.085	0.011	1.085	1.272
V	1.216	1.234	1.168	1.949	1.646	1.941	1.579	0.269	1.375	0.545
Cr	1.481	7.301	4.533	6.706	7.963	1.161	6.095	10.900	5.767	3.287
Co	2.271	1.034	0.793	3.595	2.623	1.470	0.990	4.124	2.112	1.260
Ni	0.772	1.789	2.115	0.614	1.207	5.371	5.806	2.251	2.491	2.004
Cu	5.708	0.095	2.138	2.757	3.202	3.967	4.310	4.664	3.355	1.733
Zn	3.437	6.824	7.642	4.404	5.986	1.221	8.965	9.853	6.042	2.902
Ga	1.837	1.209	1.334	2.545	2.262	6.982	2.407	4.541	2.890	1.948
Rb	2.925	7.865	10.488	4.569	4.589	14.401	7.314	12.795	8.118	4.135
Sr	0.886	3.815	0.251	0.021	0.314	4.961	0.823	3.919	1.874	2.002
Y	2.381	3.025	5.662	5.231	5.805	8.973	11.682	6.232	6.124	3.018
Zr	0.853	6.858	6.556	5.311	6.127	8.798	6.983	7.892	6.172	2.395
Nb	1.391	0.845	1.644	3.379	4.571	10.323	5.505	9.932	4.699	3.714
Ba	4.093	0.613	4.004	7.259	5.926	1.436	0.519	30.129	6.747	9.760
La	3.300	6.474	5.734	4.510	1.427	11.207	5.840	1.201	4.962	3.213
Ce	1.280	5.300	3.688	5.486	3.566	12.393	6.836	6.015	5.571	3.260
Pr	6.750	5.555	5.641	5.576	3.834	11.499	7.125	9.120	6.888	2.411
Nd	0.429	4.427	5.175	4.280	3.128	8.898	7.957	6.150	5.055	2.686
Sm	0.400	1.848	0.659	1.861	0.613	2.560	3.437	2.069	1.681	1.062
Eu	0.707	1.276	1.547	2.931	1.432	6.346	5.124	5.813	3.147	2.276
Gd	2.928	5.197	5.237	4.874	3.730	7.855	6.489	7.528	5.480	1.729
Tb	2.781	5.060	5.358	2.375	2.121	5.831	6.355	4.412	4.287	1.649
Dy	6.368	3.456	2.344	0.707	0.199	5.212	3.476	1.846	2.951	2.122
Ho	0.366	3.651	5.052	3.136	1.624	7.354	6.189	5.124	4.062	2.333
Er	5.312	1.704	2.738	1.474	0.023	5.052	4.395	2.405	2.888	1.878
Tm	1.996	2.955	4.322	4.504	4.936	8.533	6.244	5.051	4.818	1.989
Yb	4.739	1.962	2.247	1.684	2.203	5.992	4.012	2.426	3.158	1.565
Lu	6.190	5.786	5.998	5.960	6.492	11.800	9.762	5.573	7.195	2.295
Hf	0.368	0.240	1.599	0.594	1.208	7.584	0.740	2.204	1.817	2.422
Ta	3.532	5.103	6.125	14.163	8.066	21.944	11.600	18.606	11.142	6.663
^{208}Pb	83.992	211.265	2.000	56.950	72.828	49.180	8.940	19.960	63.139	66.808
^{232}Th	8.947	5.061	2.667	6.931	3.929	3.775	8.533	0.375	5.027	2.958
^{238}U	4.846	7.486	6.040	3.526	2.064	7.640	3.580	4.140	4.915	1.991

Table A-2. Concentrations of the in-house standard 2392-9 for each trace element analyzed by the Element 2 ICP-MS and the analytical precision as represented by the percent error.

	2392-9 True Values (ppm)	2006 (ppm)	Mar-07 (ppm)	Mar-07 (ppm)	7-Jun (ppm)	7-Jun (ppm)	10-Aug (ppm)	21-Aug (ppm)	1-Nov (ppm)	AVG	STDEV	% error
Sc	37.4	37.00	37.67	37.14	37.72	37.80	37.47	38.93	37.81	37.692	0.584	1.55
V	256	252.89	259.16	253.01	260.99	260.21	251.03	251.96	256.69	255.742	4.004	1.57
Cr	300	304.44	321.90	313.60	320.12	323.89	303.48	318.29	332.70	317.302	9.860	3.11
Co	39	39.89	39.40	39.31	40.40	40.02	38.43	38.61	40.61	39.584	0.792	2.00
Ni	113	112.13	110.98	110.61	112.31	111.64	106.93	106.44	110.46	110.185	2.264	2.05
Cu	76	71.66	75.93	74.38	73.90	73.57	72.99	72.72	72.46	73.450	1.317	1.79
Zn	78.4	75.71	73.05	72.41	74.95	73.71	77.44	71.37	70.68	73.663	2.275	3.09
Ga	16	15.71	16.19	15.79	15.59	15.64	14.88	15.61	15.27	15.586	0.382	2.45
Rb	0.91	0.94	0.84	0.81	0.87	0.87	0.78	0.84	0.79	0.843	0.050	5.92
Sr	116	117.03	120.43	115.71	116.02	116.36	110.25	116.95	120.55	116.662	3.208	2.75
Y	30.15	29.43	29.24	28.44	28.57	28.40	27.44	26.63	28.27	28.304	0.910	3.21
Zr	85	85.73	79.17	79.43	80.49	79.79	77.52	79.06	78.29	79.935	2.506	3.14
Nb	2.2	2.23	2.22	2.16	2.13	2.10	1.97	2.08	1.98	2.109	0.097	4.60
Ba	8	7.67	7.95	7.68	8.58	8.47	7.89	8.04	5.59	7.734	0.928	12.00
La	3	3.099	2.806	2.828	2.865	2.957	2.66	2.82	2.96	2.876	0.130	4.54
Ce	9.58	9.703	9.072	9.227	9.054	9.238	8.39	8.93	9.00	9.077	0.366	4.03
Pr	1.64	1.751	1.549	1.547	1.549	1.577	1.45	1.52	1.49	1.555	0.089	5.69
Nd	8.86	8.898	8.468	8.401	8.481	8.583	8.07	8.16	8.32	8.422	0.257	3.06
Sm	2.9	2.888	2.954	2.881	2.846	2.918	2.83	2.80	2.84	2.869	0.051	1.77
Eu	1.1	1.092	1.086	1.083	1.068	1.084	1.03	1.04	1.04	1.065	0.025	2.35
Gd	4.08	3.961	3.868	3.866	3.881	3.928	3.76	3.82	3.77	3.856	0.071	1.83
Tb	0.74	0.719	0.703	0.700	0.722	0.724	0.70	0.69	0.71	0.708	0.012	1.72
Dy	4.7	4.401	4.538	4.590	4.667	4.709	4.46	4.54	4.61	4.564	0.103	2.26
Ho	1.03	1.0338	0.9924	0.9780	0.998	1.013	0.95	0.97	0.98	0.989	0.026	2.61
Er	2.89	2.7365	2.8407	2.8109	2.847	2.889	2.74	2.76	2.82	2.807	0.054	1.93
Tm	0.45	0.4410	0.4367	0.4306	0.430	0.428	0.41	0.42	0.43	0.428	0.009	2.09
Yb	2.84	2.7054	2.7843	2.7762	2.792	2.777	2.67	2.73	2.77	2.750	0.044	1.62
Lu	0.45	0.4221	0.4240	0.4230	0.423	0.421	0.40	0.41	0.42	0.418	0.010	2.47
Hf	2.18	2.1720	2.1852	2.1452	2.167	2.206	2.01	2.16	2.13	2.148	0.059	2.73

Table A-2. Continued.

	2392-9 True Values (ppm)	2006 (ppm)	Mar-07 (ppm)	Mar-07 (ppm)	7-Jun (ppm)	7-Jun (ppm)	10-Aug (ppm)	21-Aug (ppm)	1-Nov (ppm)	AVG	STDEV	% error
Ta	0.16	0.1543	0.1518	0.1502	0.137	0.147	0.12	0.14	0.13	0.142	0.011	7.50
^{208}Pb	0.2	0.3680	0.6225	0.1960	0.314	0.346	0.10	0.22	0.24	0.301	0.156	52.05
^{232}Th	0.12	0.109	0.126	0.123	0.112	0.115	0.12	0.11	0.12	0.116	0.006	5.33
^{238}U	0.05	0.048	0.054	0.053	0.048	0.051	0.05	0.05	0.05	0.049	0.003	5.57

Notes: Noted are the accepted or "true" values for the standard as well as the values measured over 8 different runs by using 2392-9 as an unknown. All values are in ppm. The relative percent error (i.e. precision of the measurements) is determined by dividing the standard deviation by the average and then multiplying by 100 for each element. AVG- average; STDEV- standard deviation.

APPENDIX B
MAJOR, TRACE, AND ISOTOPIC DATA

Table B-1. Major element geochemistry of lavas collected from the Vance Seamounts during the Vance Seamount Expedition.

Sample	T1007-R01	T1007-R02	T1007-R06	T1007-R16	T1007-R17	T1007-R18	T1008-R05A
Longitude	-130.37	-130.38	-130.38	-130.39	-130.40	-130.40	-130.84
Latitude	45.32	45.32	45.33	45.34	45.34	45.34	45.66
Depth	2311.77	2267.68	2093.38	2187.56	2107.05	2071.45	1916.94
SiO_2	48.37	48.33	50.55	48.84	48.68	48.78	49.20
TiO_2	0.87	0.93	1.52	1.30	1.24	1.25	1.32
Al_2O_3	18.19	18.16	14.81	16.97	17.13	17.26	16.57
FeO*	8.03	8.13	9.66	8.88	8.60	8.65	9.05
MnO	0.15	0.14	0.19	0.14	0.14	0.16	0.16
MgO	9.34	9.33	7.37	8.75	8.88	8.78	8.35
CaO	12.23	12.26	12.31	11.90	11.90	11.94	12.20
Na_2O	2.35	2.37	2.69	2.71	2.69	2.76	2.46
K_2O	0.02	0.03	0.15	0.06	0.06	0.05	0.23
P_2O_5	0.05	0.05	0.13	0.10	0.08	0.09	0.13
S	0.09	0.09	0.11	0.10	0.10	0.10	0.10
Cl	0.00	0.00	0.01	0.00	0.00	0.01	0.03
Total	99.70	99.80	99.51	99.76	99.50	99.81	99.82
Mg#	69.75	69.47	60.22	66.15	67.17	66.82	64.65
K/Ti	0.03	0.04	0.14	0.07	0.07	0.06	0.24

Notes: Each sample number is composed of the *Tiburon* dive followed by the sequence in which the sample was collected during the dive. Latitude and Longitude are given in degrees, Depth is given in meters below sea level. Natural glasses were analyzed for major element concentrations (presented as weight % oxides) using an electron microprobe. FeO*, all iron as FeO; Mg#, $Mg/(Mg + Fe^{2+})$, where Fe^{2+} is 0.9 Fe total.

Table B-1. Continued.

Sample	T1008-R05B	T1008-R08	T1008-R20	T1008-R22	T1008-R23	T1011-R01	T1011-R02
Longitude	-130.84	-130.84	-130.83	-130.84	-130.84	-130.44	-130.44
Latitude	45.66	45.66	45.67	45.68	45.68	45.39	45.39
Depth	1916.94	1791.60	1705.93	1775.98	1792.41	2310.31	2294.34
SiO_2	49.23	49.20	49.65	49.57	49.59	50.43	50.34
TiO_2	1.25	1.60	1.71	1.20	1.16	1.05	0.98
Al_2O_3	16.55	16.88	15.43	16.22	16.30	15.81	15.70
FeO*	9.04	9.50	9.93	8.87	9.24	9.87	9.93
MnO	0.15	0.16	0.18	0.16	0.17	0.16	0.19
MgO	8.32	7.93	7.25	8.39	8.57	8.84	8.96
CaO	12.25	11.78	12.07	12.45	12.44	11.08	11.07
Na_2O	2.45	2.98	2.85	2.49	2.47	2.13	2.11
K_2O	0.24	0.23	0.31	0.10	0.09	0.07	0.06
P_2O_5	0.14	0.17	0.18	0.09	0.08	0.07	0.06
S	0.10	0.10	0.11	0.09	0.09	0.09	0.09
Cl	0.03	0.02	0.01	0.02	0.01	0.00	0.00
Total	99.78	100.54	99.67	99.65	100.22	99.59	99.50
Mg#	64.58	62.32	59.15	65.20	64.76	63.96	64.14
K/Ti	0.27	0.20	0.25	0.12	0.10	0.09	0.09

Sample	T1011-R03	T1011-R05	T1011-R06	T1011-R07	T1011-R12	T1011-R13	T1011-R20
Longitude	-130.44	-130.44	-130.44	-130.44	-130.44	-130.44	-130.44
Latitude	45.40	45.40	45.40	45.40	45.40	45.40	45.41
Depth	2151.56	2102.15	2062.81	2042.00	1797.70	1786.92	1766.05
SiO_2	50.60	50.74	50.88	50.77	50.54	50.46	50.75
TiO_2	1.40	1.12	1.43	1.33	1.15	1.15	1.22
Al_2O_3	14.45	14.74	14.48	14.60	14.98	14.95	14.75
FeO*	10.57	10.29	10.99	10.54	10.06	10.06	10.26
MnO	0.19	0.19	0.19	0.21	0.18	0.18	0.16
MgO	7.23	7.81	6.93	7.31	7.68	7.79	7.63
CaO	12.17	12.70	11.97	12.12	12.72	12.68	12.77
Na_2O	2.56	2.32	2.68	2.57	2.37	2.39	2.39
K_2O	0.12	0.07	0.14	0.11	0.07	0.07	0.07
P_2O_5	0.11	0.08	0.12	0.11	0.07	0.08	0.08
S	0.12	0.12	0.12	0.12	0.11	0.12	0.12
Cl	0.01	0.01	0.01	0.01	0.02	0.01	0.01
Total	99.54	100.19	99.92	99.78	99.95	99.95	100.22
Mg#	57.56	60.06	55.56	57.89	60.19	60.54	59.57
K/Ti	0.12	0.09	0.13	0.12	0.08	0.08	0.08

Table B-1. Continued.

Sample	T1011-R27	T1011-R28	T1012-R01	T1012-R02	T1012-R04	T1012-R05	T1012-R06
Longitude	-130.45	-130.45	-130.69	-130.69	-130.69	-130.68	-130.68
Latitude	45.41	45.41	45.64	45.64	45.64	45.64	45.64
Depth	1554.61	1547.76	2162.70	2162.40	2151.10	2128.20	2209.20
SiO_2	50.18	50.50	47.95	47.83	48.41	48.34	48.29
TiO_2	1.06	1.15	1.41	1.36	1.18	1.11	1.17
Al_2O_3	15.64	14.87	16.82	16.91	17.65	17.49	17.38
FeO*	9.68	10.03	10.94	10.90	10.73	10.71	10.90
MnO	0.16	0.18	0.18	0.19	0.18	0.18	0.18
MgO	8.30	7.94	7.89	7.93	8.24	8.70	8.38
CaO	12.60	12.71	11.63	11.65	11.53	11.36	11.39
Na_2O	2.25	2.34	2.76	2.71	2.48	2.45	2.50
K_2O	0.08	0.06	0.06	0.07	0.05	0.04	0.06
P_2O_5	0.08	0.07	0.08	0.08	0.06	0.05	0.06
S	0.10	0.11	0.11	0.11	0.11	0.11	0.11
Cl	0.02	0.01	0.00	0.00	0.00	0.00	0.00
Total	100.15	99.96	99.83	99.75	100.62	100.55	100.42
Mg#	62.97	61.09	58.83	59.05	60.35	61.68	60.36
K/Ti	0.11	0.08	0.06	0.07	0.05	0.05	0.07

Sample	T1012-R07	T1012-R08	T1012-R09	T1012-R10	T1012-R11	T1012-R12	T1012-R13
Longitude	-130.68	-130.68	-130.67	-130.67	-130.67	-130.67	-130.67
Latitude	45.64	45.64	45.64	45.64	45.64	45.64	45.64
Depth	2273.00	2257.60	2162.50	2082.60	2088.70	2047.20	2037.00
SiO_2	48.12	47.78	47.96	47.92	47.93	48.13	47.78
TiO_2	1.28	1.23	1.16	1.18	1.19	1.25	1.13
Al_2O_3	17.75	17.17	17.82	17.86	17.80	17.44	17.72
FeO*	9.81	10.10	9.54	9.48	9.49	9.97	9.82
MnO	0.17	0.19	0.16	0.16	0.17	0.16	0.16
MgO	8.30	9.13	8.51	8.51	8.50	8.09	8.80
CaO	11.72	11.37	11.62	11.58	11.60	11.65	11.51
Na_2O	2.85	2.68	2.83	2.85	2.82	2.92	2.71
K_2O	0.05	0.06	0.05	0.05	0.04	0.05	0.04
P_2O_5	0.07	0.08	0.06	0.05	0.07	0.09	0.05
S	0.11	0.10	0.09	0.10	0.10	0.11	0.10
Cl	0.00	0.01	0.00	0.00	0.00	0.00	0.00
Total	100.22	99.89	99.79	99.75	99.71	99.87	99.83
Mg#	62.62	64.17	63.88	64.02	63.97	61.67	63.99
K/Ti	0.05	0.07	0.06	0.06	0.05	0.06	0.05

Table B-1. Continued.

Sample	T1012-R14A	T1012-R14B	T1012-R17	T1012-R18	T1012-R20	T1012-R21	T1012-R22
Longitude	-130.67	-130.67	-130.66	-130.66	-130.66	-130.66	-130.66
Latitude	45.64	45.64	45.63	45.63	45.63	45.63	45.63
Depth	1976.00	1976.00	1961.50	1975.40	1965.00	1988.00	1969.10
SiO_2	47.92	47.89	48.10	48.02	48.12	50.63	48.16
TiO_2	1.18	1.10	1.19	1.28	1.31	1.37	1.21
Al_2O_3	17.77	17.76	17.76	17.59	17.40	14.55	17.84
FeO*	9.64	9.97	9.50	9.89	9.94	10.82	9.92
MnO	0.16	0.17	0.16	0.17	0.17	0.19	0.18
MgO	8.64	8.99	8.44	8.22	8.05	7.30	8.33
CaO	11.42	11.48	11.63	11.59	11.67	12.11	11.46
Na_2O	2.81	2.66	2.84	2.97	2.90	2.47	2.88
K_2O	0.04	0.04	0.05	0.05	0.05	0.10	0.05
P_2O_5	0.07	0.07	0.07	0.08	0.09	0.09	0.08
S	0.10	0.10	0.10	0.10	0.10	0.13	0.10
Cl	0.00	0.00	0.00	0.00	0.00	0.02	0.00
Total	99.74	100.24	99.83	99.96	99.79	99.78	100.22
Mg#	64.00	64.14	63.78	62.23	61.61	57.21	62.47
K/Ti	0.05	0.06	0.06	0.06	0.05	0.10	0.05

Sample	T1012-R23	T1013-R02	T1013-R14	T1013-R17	T1013-R18	T1013-R19	T1013-R20
Longitude	-130.66	-130.51	-130.51	-130.52	-130.52	-130.52	-130.52
Latitude	45.63	45.45	45.45	45.45	45.45	45.45	45.45
Depth	1974.20	2060.30	1924.00	1830.20	1906.70	1897.70	1887.90
SiO_2	48.14	49.93	50.52	48.79	50.60	50.31	50.26
TiO_2	1.20	0.94	1.39	0.87	1.36	0.95	0.87
Al_2O_3	17.79	15.74	14.56	17.26	14.47	15.52	15.64
FeO*	9.77	9.41	10.77	8.68	10.73	8.71	8.70
MnO	0.16	0.16	0.18	0.15	0.19	0.16	0.15
MgO	8.55	8.60	7.34	9.45	7.34	8.44	8.51
CaO	11.49	12.82	12.05	12.52	12.16	13.23	13.26
Na_2O	2.88	2.07	2.45	2.12	2.50	2.20	2.19
K_2O	0.05	0.04	0.09	0.03	0.10	0.04	0.04
P_2O_5	0.06	0.06	0.11	0.04	0.09	0.05	0.05
S	0.10	0.11	0.14	0.09	0.13	0.09	0.09
Cl	0.00	0.01	0.02	0.00	0.02	0.00	0.00
Total	100.18	99.90	99.63	100.02	99.68	99.70	99.75
Mg#	63.45	64.42	57.47	68.33	57.55	65.75	65.98
K/Ti	0.06	0.06	0.09	0.05	0.10	0.06	0.07

Table B-1. Continued.

Sample	T1013-R21	T1013-R22	T1013-R23	T1013-R24	T1013-R25	T1013-R27	T1013-R29
Longitude	-130.52	-130.52	-130.52	-130.52	-130.52	-130.52	-130.53
Latitude	45.45	45.46	45.46	45.46	45.46	45.46	45.46
Depth	1893.20	1866.20	1866.10	1857.80	1856.90	1824.30	1836.00
SiO_2	50.21	50.37	50.35	50.30	50.22	50.06	49.83
TiO_2	0.89	0.94	0.91	0.92	0.97	1.04	0.92
Al_2O_3	15.57	15.54	15.54	15.49	15.53	15.39	15.70
FeO*	8.78	8.79	8.74	8.80	8.83	9.54	9.48
MnO	0.17	0.16	0.16	0.17	0.15	0.19	0.17
MgO	8.54	8.48	8.49	8.49	8.47	8.31	8.66
CaO	13.14	13.31	13.19	13.24	13.25	12.85	12.84
Na_2O	2.18	2.19	2.18	2.21	2.15	2.15	2.06
K_2O	0.04	0.04	0.04	0.04	0.04	0.05	0.03
P_2O_5	0.06	0.06	0.06	0.05	0.07	0.07	0.06
S	0.10	0.10	0.10	0.10	0.09	0.11	0.11
Cl	0.00	0.00	0.00	0.00	0.00	0.01	0.02
Total	99.68	99.97	99.76	99.81	99.76	99.77	99.89
Mg#	65.86	65.66	65.83	65.66	65.54	63.31	64.43
K/Ti	0.06	0.06	0.06	0.06	0.06	0.06	0.05
Sample	T1013-R30	T1013-R30	T1013-R31	T1014-R04	T1014-R08	T1014-R10	T1014-R13
Longitude	-130.53	-130.53	-130.53	-130.33	-130.34	-130.34	-130.34
Latitude	45.46	45.46	45.46	45.29	45.29	45.29	45.29
Depth	1807.30	1807.30	1831.20	2357.60	2379.50	2366.00	2361.40
SiO_2	50.11	48.83	49.85	50.71	50.74	50.83	50.32
TiO_2	1.00	0.82	0.93	1.34	1.27	1.35	1.19
Al_2O_3	15.35	17.18	15.53	14.58	14.60	14.56	15.20
FeO*	9.56	8.53	9.47	10.23	10.16	10.05	9.61
MnO	0.16	0.15	0.17	0.17	0.18	0.18	0.18
MgO	8.35	9.38	8.73	7.45	7.42	7.42	7.92
CaO	12.91	12.55	12.80	12.18	12.19	12.31	12.47
Na_2O	2.13	2.10	2.04	2.58	2.59	2.58	2.47
K_2O	0.05	0.04	0.04	0.11	0.11	0.11	0.10
P_2O_5	0.07	0.06	0.05	0.12	0.10	0.11	0.09
S	0.11	0.09	0.11	0.11	0.12	0.11	0.11
Cl	0.02	0.00	0.02	0.00	0.01	0.00	0.01
Total	99.83	99.72	99.74	99.58	99.48	99.60	99.68
Mg#	63.39	68.53	64.65	59.07	59.14	59.42	62.02
K/Ti	0.07	0.07	0.05	0.12	0.12	0.11	0.11

Table B-1. Continued.

Sample	T1014-R15	T1014-R16	T1014-R17	T1014-R18	T1014-R19	T1014-R22
Longitude	-130.35	-130.35	-130.35	-130.35	-130.35	-130.35
Latitude	45.29	45.29	45.29	45.29	45.29	45.29
Depth	2326.10	2319.70	2322.40	2310.50	2286.80	2298.10
SiO_2	50.28	50.82	50.88	50.22	50.71	50.76
TiO_2	1.31	1.39	1.37	1.34	1.31	1.28
Al_2O_3	14.79	14.54	14.56	15.03	14.56	14.57
FeO*	9.98	10.07	10.04	9.75	10.12	10.00
MnO	0.17	0.19	0.17	0.16	0.18	0.20
MgO	7.49	7.47	7.43	7.74	7.43	7.42
CaO	12.47	12.27	12.22	12.42	12.26	12.26
Na_2O	2.57	2.56	2.57	2.57	2.56	2.56
K_2O	0.10	0.11	0.11	0.10	0.12	0.11
P_2O_5	0.11	0.12	0.13	0.10	0.10	0.11
S	0.12	0.11	0.12	0.11	0.11	0.11
Cl	0.01	0.01	0.01	0.00	0.01	0.00
Total	99.40	99.67	99.60	99.54	99.46	99.38
Mg#	59.80	59.52	59.48	61.13	59.26	59.50
K/Ti	0.11	0.11	0.12	0.10	0.13	0.12

Sample	T1014-R23	T1014-R24
Longitude	-130.35	-130.35
Latitude	45.29	45.29
Depth	2288.50	2284.30
SiO_2	50.59	50.56
TiO_2	1.25	1.29
Al_2O_3	14.49	14.57
FeO*	10.05	10.07
MnO	0.18	0.20
MgO	7.40	7.44
CaO	12.30	12.26
Na_2O	2.56	2.53
K_2O	0.11	0.12
P_2O_5	0.10	0.10
S	0.11	0.11
Cl	0.00	0.00
Total	99.14	99.23
Mg#	59.36	59.43
K/Ti	0.12	0.12

Table B-2. Trace element geochemistry of select lavas analyzed in this study.

Sample	DR1-A1	DR1-D1	DR2-H	DR2-I	DR5-B	DR5-F	DR14-1	DR15-1
Li								
B								
Sc	42.59	42.97	39.82	38.69	38.99	37.88	35.98	32.73
Ti	13530.75	13674.13	10907.95	11039.61	13234.45	12771.21	9637.95	11305.63
V	285.74	278.85	257.22	242.36	256.22	250.67	230.57	223.21
Cr	271.98	270.63	319.26	305.37	318.88	312.97	361.84	312.98
Co	38.09	37.10	39.37	37.12	36.78	36.68	37.96	37.17
Ni	56.71	56.69	60.91	55.62	72.84	69.48	73.33	115.00
Cu	82.50	78.64	77.29	73.33	67.42	68.61	78.86	69.52
Zn	79.70	78.28	74.96	72.88	73.73	71.36	71.16	71.43
Ga	16.92	16.84	15.97	15.87	16.50	16.47	17.39	15.35
Rb	0.93	1.00	1.35	1.05	1.75	1.72	0.37	0.68
Sr	131.63	130.79	86.79	74.97	142.17	138.64	71.65	97.24
Y	32.43	30.95	26.71	25.00	28.44	27.83	23.88	24.73
Zr	96.18	93.59	62.11	63.21	91.06	86.02	53.85	69.94
Nb	2.44	2.28	1.26	1.28	4.46	4.32	0.84	1.71
Cs								
Ba	11.23	11.51	8.34	6.73	21.18	20.48	5.48	7.16
La	3.32	3.33	2.07	1.96	3.97	3.88	1.66	2.52
Ce	10.36	10.28	6.46	6.17	11.01	10.88	5.29	7.68
Pr	1.82	1.80	1.21	1.17	1.84	1.79	1.03	1.40
Nd	9.89	9.88	7.16	7.00	9.73	9.59	6.31	8.07
Sm	3.23	3.27	2.46	2.38	3.12	3.07	2.08	2.57
Eu	1.20	1.18	0.95	0.90	1.16	1.13	0.82	0.97
Gd	4.38	4.35	3.65	3.49	4.16	4.08	3.18	3.71
Tb	0.79	0.80	0.68	0.66	0.76	0.73	0.60	0.70
Dy	5.21	5.16	4.38	4.19	4.77	4.71	3.78	4.22
Ho	1.07	1.08	0.93	0.90	1.00	0.96	0.82	0.90
Er	3.11	3.12	2.68	2.57	2.85	2.81	2.34	2.55
Tm	0.48	0.47	0.42	0.39	0.43	0.43	0.36	0.39
Yb	3.07	3.01	2.64	2.50	2.76	2.70	2.23	2.40
Lu	0.47	0.47	0.41	0.38	0.42	0.41	0.34	0.38
Hf	2.53	2.50	1.84	1.89	2.48	2.35	1.55	2.00
Ta	0.20	0.19	0.14	0.13	0.34	0.33	0.08	0.16
^{208}Pb	0.27	0.27	0.13	0.09	0.25	0.26	0.04	0.10
^{232}Th	0.15	0.15	0.09	0.09	0.28	0.28	0.07	0.13
^{238}U	0.07	0.07	0.06	0.05	0.11	0.11	0.04	0.05

Notes: Natural glasses were analyzed for trace element concentrations (presented in ppm) using an Element II ICP-MS. Blanks indicate elements that were not analyzed.

Table B-2. Continued.

Sample	DR16-6	T1007-R2	T1007-R16	T1007-R17	T1007-R18	T1008-R5A	T1008-R5B	T1008-R8
Li				4.04	4.13			
B								
Sc	39.53	27.43	33.45	38.48	39.47	35.13	34.78	35.62
Ti	11060.90	8499	12169	11067.45	11520.74	12464	12359	15421
V	275.11	171.0	214.4	204.17	205.65	237.1	232.3	244.4
Cr	315.27	281.0	510.1	495.99	445.58	286.9	285.9	248.2
Co	43.34	44.6	44.8	44.38	42.34	40.1	41.3	39.7
Ni	54.63	197.0	241.6	238.11	190.38	122.1	123.7	123.5
Cu	76.03	80.3	73.3	74.05	74.64	75.6	74.7	67.0
Zn	74.25	61.9	66.4	63.94	63.88	70.2	69.3	73.3
Ga	16.23	15.0	15.9	15.49	15.88	16.7	16.6	18.1
Rb	0.67	0.16	0.36	0.41	0.40	1.67	1.67	1.38
Sr	78.45	105	138	141.49	144.60	171	167	193
Y	25.82	19.9	26.9	25.68	25.99	25.8	25.3	29.9
Zr	62.14	46.3	79.1	75.17	75.70	87.0	88.3	110.1
Nb	1.35	0.5	1.3	1.21	1.19	4.7	4.9	4.9
Cs				0.01	0.01			
Ba	9.64	1.96	4.78	5.35	5.26	19.51	20.09	16.67
La	2.05	1.12	2.25	2.22	2.24	4.47	4.56	4.80
Ce	7.17	4.60	8.27	7.80	7.86	12.01	12.43	13.94
Pr	1.21	0.92	1.49	1.43	1.45	1.82	1.88	2.22
Nd	7.15	5.58	8.18	7.92	7.95	9.27	9.27	11.15
Sm	2.44	2.05	2.86	2.78	2.78	2.91	2.92	3.57
Eu	0.91	0.85	1.09	1.06	1.08	1.10	1.09	1.30
Gd	3.53	2.95	3.77	3.63	3.67	3.73	3.79	4.40
Tb	0.67	0.53	0.67	0.66	0.67	0.66	0.68	0.77
Dy	4.33	3.45	4.30	4.17	4.24	4.22	4.31	4.86
Ho	0.92	0.72	0.92	0.88	0.89	0.87	0.90	1.04
Er	2.68	2.08	2.57	2.49	2.52	2.51	2.61	2.86
Tm	0.41	0.31	0.39	0.37	0.38	0.38	0.38	0.44
Yb	2.53	1.94	2.51	2.39	2.43	2.45	2.44	2.75
Lu	0.39	0.30	0.38	0.36	0.37	0.36	0.38	0.43
Hf	1.80	1.44	2.10	2.03	2.08	2.20	2.22	2.69
Ta	0.10	0.04	0.09	0.09	0.08	0.32	0.32	0.32
^{208}Pb	0.63	0.018	0.167	0.170	0.189	0.303	0.328	0.396
^{232}Th	0.17	0.025	0.070	0.077	0.075	0.275	0.279	0.273
^{238}U	0.05	0.015	0.034	0.029	0.030	0.121	0.120	0.118

Table B-2. Continued.

Sample	T1008-R20	T1008-R22	T1008-R23	T1011-R1	T1011-R7	T1011-R12	T1011-R27	T1012-R1
Li	4.87	4.41					4.52	5.95
B								3.82
Sc	47.09	44.63	32.15	33.19	43.05	43.90	47.98	45.52
Ti	16813.21	9939.61	9511	9828	13107	11316	9542.04	12743.80
V	261.43	232.95	197.6	181.8	299.4	277.3	263.54	308.09
Cr	304.94	335.37	291.4	545.6	205.5	342.0	281.80	190.76
Co	38.19	40.63	36.2	51.5	42.4	42.3	40.77	44.12
Ni	79.69	88.07	84.0	288.4	54.0	58.0	83.22	54.89
Cu	72.83	81.69	77.5	84.7	75.4	83.5	77.88	84.83
Zn	73.30	69.38	62.5	77.9	81.8	77.3	72.20	79.95
Ga	17.72	16.24	14.2	15.7	17.3	16.7	16.24	16.79
Rb	2.07	0.77	0.63	0.56	0.88	0.62	0.65	0.76
Sr	202.38	117.17	103	112	113	91	99.24	88.39
Y	28.98	25.12	22.1	19.7	30.8	27.6	26.68	32.23
Zr	111.74	59.16	52.1	47.3	81.2	61.2	59.23	75.99
Nb	6.23	1.99	1.8	1.5	2.6	1.5	1.69	1.81
Cs	0.02	0.01					0.01	0.02
Ba	24.88	9.62	7.93	6.93	11.46	6.51	8.14	9.36
La	5.85	2.32	2.02	1.67	3.20	2.06	2.23	2.55
Ce	15.56	6.93	6.25	5.38	9.95	6.90	6.94	8.06
Pr	2.37	1.20	1.06	0.94	1.64	1.21	1.21	1.43
Nd	11.69	6.66	6.04	5.32	8.76	6.74	6.59	8.10
Sm	3.55	2.44	2.17	1.94	3.09	2.56	2.40	2.88
Eu	1.29	0.96	0.87	0.82	1.16	1.00	0.95	1.11
Gd	4.40	3.45	3.05	2.80	4.22	3.64	3.46	4.12
Tb	0.77	0.64	0.56	0.51	0.78	0.67	0.65	0.79
Dy	4.82	4.10	3.60	3.25	5.15	4.44	4.28	5.15
Ho	1.00	0.88	0.77	0.70	1.09	0.95	0.92	1.13
Er	2.80	2.51	2.17	1.97	3.19	2.74	2.65	3.26
Tm	0.42	0.39	0.34	0.29	0.47	0.42	0.41	0.49
Yb	2.71	2.43	2.13	1.87	3.07	2.76	2.64	3.19
Lu	0.41	0.37	0.32	0.28	0.49	0.42	0.40	0.48
Hf	2.79	1.75	1.55	1.36	2.18	1.76	1.76	2.17
Ta	0.41	0.13	0.12	0.10	0.17	0.10	0.11	0.12
^{208}Pb	0.498	0.112	0.060	0.047	0.214	0.096	0.104	0.052
^{232}Th	0.352	0.104	0.100	0.081	0.149	0.086	0.105	0.103
^{238}U	0.152	0.053	0.046	0.039	0.065	0.047	0.062	0.044

Table B-2. Continued.

Sample	T1012-R4	T1012-R8	T1012-R9	T1012-R14A	T1012-R21	T1013-R2	T1013-R17	T1013-R21
Li			4.27	4.30	4.21	4.81		3.83
B				3.27	1.83			
Sc	36.26	35.25	41.37	37.43	37.20	46.45	33.46	48.62
Ti	10431	11413	10628.92	11950.40	11521.10	7444.96	8650	6024.47
V	196.4	198.4	190.17	216.19	197.85	252.61	210.1	230.01
Cr	292.3	450.0	237.97	264.50	344.92	371.59	307.1	412.05
Co	50.8	54.1	43.29	46.80	50.89	41.73	45.2	40.50
Ni	209.9	314.3	145.83	167.97	220.99	86.02	151.2	87.99
Cu	85.9	82.8	73.83	80.69	87.48	88.65	87.1	89.12
Zn	75.2	75.7	66.34	72.88	71.79	70.36	65.1	63.73
Ga	16.2	15.6	16.27	16.82	15.95	15.65	15.0	15.31
Rb	0.42	0.57	0.43	0.59	0.44	0.43	0.27	0.42
Sr	115	137	156.47	149.38	153.47	63.63	84	85.16
Y	25.5	26.6	26.22	27.29	26.59	24.16	21.7	21.72
Zr	62.3	74.9	74.20	78.11	71.96	42.67	48.4	42.37
Nb	1.2	1.7	1.06	1.51	1.05	0.82	0.8	0.88
Cs			0.01	0.01	0.01	0.01		0.01
Ba	6.62	7.66	5.52	5.99	5.71	4.20	3.56	5.39
La	1.94	2.61	2.19	2.69	2.26	1.34	1.39	1.43
Ce	6.64	8.77	7.54	8.59	7.61	4.50	5.16	4.73
Pr	1.16	1.50	1.37	1.49	1.38	0.85	0.95	0.88
Nd	6.45	7.99	7.56	8.09	7.66	5.05	5.47	5.09
Sm	2.37	2.73	2.60	2.71	2.52	1.99	1.97	1.91
Eu	0.96	1.07	1.03	1.07	1.03	0.80	0.81	0.79
Gd	3.25	3.63	3.51	3.64	3.48	3.04	2.88	2.80
Tb	0.63	0.67	0.64	0.68	0.64	0.59	0.55	0.52
Dy	4.13	4.40	4.18	4.41	4.20	3.88	3.58	3.47
Ho	0.89	0.93	0.90	0.96	0.92	0.84	0.76	0.75
Er	2.59	2.75	2.56	2.76	2.66	2.45	2.24	2.15
Tm	0.40	0.41	0.39	0.40	0.40	0.37	0.33	0.33
Yb	2.62	2.75	2.53	2.64	2.62	2.44	2.17	2.13
Lu	0.40	0.43	0.39	0.41	0.39	0.37	0.34	0.32
Hf	1.70	1.94	1.95	2.06	1.90	1.38	1.41	1.34
Ta	0.08	0.11	0.07	0.11	0.08	0.05	0.05	0.06
^{208}Pb	0.099	0.238	0.245	0.126	0.153	-0.005	0.041	0.017
^{232}Th	0.109	0.095	0.071	0.095	0.064	0.048	0.117	0.059
^{238}U	0.044	0.042	0.027	0.042	0.030	0.022	0.054	0.022

Table B-2. Continued.

Sample	T1013-R29	T1014-R4	T1014-R13	T1014-R17	T1014-R18	T1014-R22	94JdF DR2-1	94JdF DR2-5
Li	4.36	5.39	4.51	5.31	5.28	5.21	4.04	4.60
B			15.46				397.67	597.70
Sc	47.59	53.07	42.18	52.93	43.71	52.90	42.35	39.95
Ti	7141.27	13211.04	12496.60	13621.48	13201.44	13126.77	10834.64	10015.38
V	251.77	295.58	279.41	296.37	280.53	293.03	281.09	265.41
Cr	372.93	186.36	339.09	184.61	343.96	184.59	358.80	358.72
Co	42.66	40.53	41.25	39.51	40.94	39.17	42.07	42.18
Ni	87.28	57.66	82.03	55.45	83.02	55.56	69.61	74.11
Cu	94.68	76.23	84.32	74.93	76.23	75.42	88.64	87.85
Zn	69.84	78.14	76.04	76.64	73.20	77.38	75.27	74.93
Ga	15.77	17.17	16.42	17.18	16.39	17.07	15.72	15.54
Rb	0.39	0.91	0.82	0.87	0.65	0.91	0.46	0.42
Sr	64.15	122.98	123.51	122.27	130.34	122.28	81.78	81.18
Y	24.42	30.64	28.33	28.39	29.65	28.63	26.50	24.65
Zr	41.26	80.80	76.46	80.49	79.22	80.09	59.60	55.72
Nb	0.84	2.44	2.21	2.45	1.94	2.44	1.29	1.18
Cs	0.01	0.01	0.01	0.01	0.01	0.01	0.01	0.01
Ba	4.70	11.25	10.26	11.24	6.59	11.05	5.21	4.96
La	1.32	3.13	2.83	3.05	2.95	3.05	1.95	1.81
Ce	4.39	9.62	8.86	9.43	9.03	9.40	6.51	6.03
Pr	0.83	1.63	1.52	1.60	1.51	1.61	1.19	1.10
Nd	4.89	8.67	8.34	8.46	8.51	8.49	6.83	6.31
Sm	1.96	2.98	2.83	2.96	2.97	2.93	2.44	2.24
Eu	0.80	1.14	1.07	1.12	1.09	1.11	0.95	0.88
Gd	2.98	4.13	3.88	4.05	3.94	4.01	3.47	3.24
Tb	0.57	0.75	0.72	0.73	0.74	0.73	0.66	0.61
Dy	3.83	4.96	4.64	4.87	4.84	4.79	4.30	4.02
Ho	0.84	1.06	0.99	1.03	1.02	1.03	0.93	0.87
Er	2.45	3.03	2.85	2.97	2.95	2.96	2.68	2.50
Tm	0.38	0.47	0.43	0.45	0.45	0.45	0.40	0.38
Yb	2.45	2.98	2.76	2.91	2.92	2.90	2.65	2.48
Lu	0.37	0.46	0.42	0.44	0.44	0.44	0.40	0.37
Hf	1.35	2.24	2.09	2.24	2.16	2.21	1.74	1.65
Ta	0.05	0.17	0.14	0.16	0.13	0.16	0.09	0.08
^{208}Pb	-0.001	0.084	0.099	0.190	0.238	0.163	-0.01	-0.02
^{232}Th	0.059	0.144	0.117	0.099	0.118	0.120	0.064	0.058
^{238}U	0.023	0.062	0.054	0.060	0.052	0.060	0.033	0.031

Table B-2. Continued.

Sample	94 JdF DR4-2	94 JdF DR4-5	94 JdF DR5-1	94 JdF DR5-3	95 JdF DR1-1	95 JdF DR1-3	95 JdF DR1-6
Li	5.56	6.16	6.31	16.27	9.52	12.22	5.92
B	12.44	24.30	7.96	219.89	2.63	30.75	1.98
Sc	42.07	42.76	43.30	42.95	42.61	38.95	39.04
Ti	14570.35	13024.29	13392.05	16260.11	16281.83	9424.31	9481.69
V	302.81	316.98	330.39	368.36	365.12	254.16	252.26
Cr	291.68	194.22	195.65	202.61	204.30	428.24	429.71
Co	40.01	41.68	43.20	43.19	44.73	41.26	40.99
Ni	82.06	53.10	52.70	54.52	54.46	103.19	99.25
Cu	70.71	69.96	68.93	62.23	61.49	81.60	79.90
Zn	85.18	88.16	82.84	96.57	93.92	80.94	76.50
Ga	16.56	16.52	16.71	18.03	17.95	14.75	15.08
Rb	0.98	0.67	0.66	0.89	0.86	0.35	0.28
Sr	113.56	58.36	59.96	64.56	64.71	67.25	70.18
Y	33.62	33.19	34.32	41.85	41.37	22.00	23.40
Zr	92.69	75.56	75.11	104.77	95.44	53.93	48.22
Nb	2.46	1.84	1.84	2.44	2.32	0.70	0.67
Cs	0.01	0.01	0.01	0.02	0.01	0.04	0.01
Ba	9.08	6.25	6.72	12.37	9.46	7.25	3.59
La	3.45	2.41	2.59	3.14	3.10	1.34	1.48
Ce	10.83	7.90	8.28	10.20	9.93	4.76	5.08
Pr	1.85	1.41	1.48	1.79	1.75	0.92	0.96
Nd	10.06	8.11	8.45	10.16	9.97	5.51	5.72
Sm	3.40	2.98	3.09	3.66	3.59	2.01	2.11
Eu	1.25	1.06	1.11	1.28	1.25	0.80	0.85
Gd	4.60	4.29	4.37	5.24	5.09	2.97	3.09
Tb	0.85	0.82	0.85	1.02	0.98	0.57	0.59
Dy	5.62	5.46	5.61	6.72	6.44	3.72	3.86
Ho	1.20	1.19	1.24	1.45	1.42	0.79	0.85
Er	3.43	3.44	3.51	4.18	4.11	2.32	2.44
Tm	0.51	0.52	0.54	0.64	0.64	0.34	0.36
Yb	3.39	3.42	3.52	4.23	4.06	2.27	2.30
Lu	0.52	0.53	0.55	0.66	0.63	0.35	0.36
Hf	2.60	2.22	2.31	3.03	2.75	1.59	1.52
Ta	0.18	0.12	0.13	0.16	0.16	0.05	0.05
^{208}Pb	0.21	-0.04	0.05	0.15	0.10	-0.06	-0.02
^{232}Th	0.136	0.074	0.109	0.133	0.125	0.024	0.036
^{238}U	0.058	0.049	0.053	0.063	0.063	0.028	0.022

Table B-3. Isotope geochemistry of select Vance Seamount samples.

Sample	$^{143}Nd/^{144}Nd$	$^{87}Sr/^{86}Sr$	$^{208}Pb/^{204}Pb$	$^{207}Pb/^{204}Pb$	$^{206}Pb/^{204}Pb$
T1008-R5A	0.513111	0.702617	37.920	15.492	18.500
T1008-R20	0.513107	0.702762	37.947	15.496	18.526
T1008-R23	0.513131	0.702759	38.214	15.538	18.580
T1012-R01	0.513082	0.702682	38.557	15.576	18.816
T1012-R08	0.513052	0.702575	38.040	15.500	18.678
T1012-R14A		0.702595			
T1012-R21	0.513060	0.702629	38.119	15.540	18.636
T1013-R2	0.513156	0.702607	37.157	15.409	17.728
T1013-R17	0.513156	0.702597	37.656	15.449	18.233
T1013-R18	0.513142	0.702787	37.975	15.540	18.509
T1013-R21	0.513146	0.703116	37.998	15.491	18.457
T1013-R30	0.513139	0.702915	37.904	15.482	18.471
T1011-R01	0.513156	0.702614	38.044	15.510	18.507
T1011-R07	0.513149	0.702551	37.850	15.498	18.409
T1011-R12	0.513152	0.702589	37.803	15.489	18.395
T1011-R20	0.513147	0.702578			
T1011-R27	0.513155	0.702685	37.823	15.496	18.373
T1007-R02	0.513181	0.702521	37.477	15.454	18.118
T1007-R16	0.513167	0.702477	37.734	15.482	18.311
T1007-R17	0.513174	0.702510	37.629	15.445	18.282
T1014-R4	0.513146	0.702576	37.563	15.418	18.262
T1014-R13	0.513134	0.703157	37.816	15.494	18.347
T1014-R18	0.513144	0.702595	37.665	15.442	18.350
T1014-R22	0.513145	0.702687	37.696	15.461	18.326

Notes: Natural glasses were analyzed for isotopic ratios using a thermal ionization mass spectrometer at Carleton University[*Cornejo,* 2008]. Blanks indicate ratios that were not determined.

LIST OF REFERENCES

Allan J. F., R. Batiza and P. F. Lonsdale, Petrology and chemistry of lavas from seamounts flanking the East Pacific Rise axis, 21 degrees N: Implications concerning the mantle source composition for both seamount and adjacent EPR lavas, *Seamounts, islands, and atolls, Geophysical Monograph 43***,** 255-282, 1987.

Allan, J. F., R. Batiza, M. R. Perfit, D. J. Fornari, and R. O. Sack, Petrology of lava from the Lamont Seamount chain and adjacent East Pacific Rise, 10ºN, *J. Petrol., 30,* 1,245-1,298, 1989.

Barr, S. M., Seamount chains near the crest of the Juan de Fuca Ridge, northeast Pacific Ocean, *Marine Geol., 17*, 1-19, 1974.

Batiza, R., Abundances, distribution, and sizes of volcanoes in the Pacific Ocean and implications for the origin of non-hotspot volcanoes, *Earth Plan. Sci. Letters, 60*, 195-206, 1982.

Batiza R., Seamounts and seamount chains of the eastern Pacific. In *The eastern Pacific Ocean and Hawaii* (eds. E. L. Winterer, D. M. Hussong and R. W. Decker), Geol. Soc. Am., Denver, CO, United States (USA), United States (USA), 1989.

Batiza, R., and D. Vanko, Volcanic development of small oceanic central volcanoes on the flanks of the East Pacific Rise inferred from narrow-beam echo-sounder surveys, *Mar. Geol., 54*, 53-90, 1983.

Batiza, R., and D. Vanko, Petrology of young seamounts, *J. Geophys. Res., 89*, 11,235-11,260, 1984.

Batiza R., T. L. Smith, and Y. Niu, Geological and petrologic evolution of seamounts near the EPR based on submersible and camera study, *Mar. Geophys. Res. 11***,** 169-236, 1989.

Batiza R., Y. Niu, and W. C. Zayac, Chemistry of seamounts near the East Pacific Rise; Implications for the geometry of subaxial mantle flow, *Geology (Boulder) 18***,** 1122-1125, 1990.

Beattie, P., Uranium-thorium disequilibria and portioning on melting of garnet peridotite, *Nature, 363,* 63-65, 1993.

Cande, S. C., and D. V. Kent, Revised calibration of the geomagnetic polarity timescale for the Late Cretaceous and Cenezoic, *J. Geophys. Res., 100*, 6,093-6,095, 1995.

Chadwick, D. J., M.R. Perfit, W.I. Ridley, I.R. Jonasson, G. Kamenov, W.W. Chadwick, Jr., R.W. Embley, P. Le Roux, and M.C. Smith, Magmatic effects of the Cobb Hotspot on the Juan de Fuca Ridge, *J. Geophys. Res., 110*, B03101, doi:10.1029/2003JB002767, 2004.

Clague, D. A., J. R. Reynolds, and A. S. Davis, Near-ridge seamount chains in the northeastern Pacific Ocean, *J. Geophys. Res., 105*:*B7*, 16,541-16,561, 2000.

Cousens B., Basalt geochemistry of the Explorer Ridge area, Northeast Pacific Ocean, *Canadian Journal of Earth Sciences 21***,** 157, 1984.

Cousens B. L., Depleted and enriched upper mantle sources for basaltic rocks from diverse tectonic environments in the Northeast Pacific Ocean; the generation of oceanic alkaline vs. tholeiitic basalts; Earth processes; reading the isotopic code, *Geophysical Monograph 95***,** 207-231, 1996a.

Cousens, B. L., Magmatic evolution of Quaternary mafic magmas at Long Valley Caldera and the Devils Postpile, California: Effects of crustal contamination on lithospheric mantle-derived magmas, *J. Geophys. Res., 101,* 27,673-27,689, 1996b.

Cousens B. L., R. L. Chase, and J. G. Schilling, Geochemistry and origin of volcanic rocks from Tuzo Wilson and Bowie seamounts, Northeast Pacific Ocean, *Canadian Journal of Earth Sciences; Journal Canadien des Sciences de la Terre 22***,** 1609-1617, 1985.

Cousens B. L., J. F. Allan, M. I. Leybourne, R. L. Chase, and N. Van Wagoner, Mixing of magmas from enriched and depleted mantle sources in the Northeast Pacific; West Valley segment, Juan de Fuca Ridge, *Contributions to Mineralogy and Petrology 120***,** 337-357,

Danyushevsky, L.V., The effect of small amounts of H2O on crystallisation of mid-ocean ridge and backarc basin magmas, *Journal of Volcanology and Geothermal Research, 110,* 265–280, 2001.

Davis, A. S., and D. A. Clague, Geochemistry, mineralogy, and petrogenesis of basalt from the Gorda Ridge, *J. Geophys. Res., 92*, 10,467-10,483, 1987.

Davis, A. S., D. A. Clague, and W. F. Friesen, Petrology and mineral chemistry of basalt from the Escanaba Trough, southern Gorda Ridge, *U.S. Geol. Surv. Bull. 2022*, 153-170, 1994.

Davis, E. E., and J. L. Karsten, On the cause of the asymmetric distribution of the seamounts about the Juan de Fuca Ridge: Ridge-crest migration over a heterogeneous astenosphere, *Earth Planet. Sci. Letters, 79*, 385-396, 1979.

Desonie, D. L., and R. A. Duncan, The Cobb-Eickelberg Seamount Chain: Hotspot volcanism with mid-ocean ridge basalt affinity, *J. Geophys. Res., 95*, 12,697-12,711, 1990.

Eaby J. S., D. A. Clague, and J. R. Delaney, Sr isotopic variations along the Juan de Fuca Ridge, *J. Geophys. Res., 89***,** 7,883-7,890, 1984.

Epp, D., and N. C. Smoot, Distribution of seamounts in the North Atlantic, *Nature, 337*, 254-257, 1989.

Finney, A. R., Petrology and geochemistry of the Vance Seamounts: Near-ridge seamounts along the Juan de Fuca Ridge, undergraduate honors thesis, 115 pp, Univ. of Fla., Gainesville, 1989.

Fornari, D. J., R. Batiza, and J. F. Allan, Irregularly shaped seamounts near the East Pacific Rise: Implications for seamount origin and rise-crest processes, in *Seamounts, Islands, and Atolls, Geophys. Monogr. Ser.,* vol. 43, edited by B. H. Keating et al., pp. 35-47, AGU, Washington, D. C., 1987.

Fornari, D. J., M. R. Perfit, J. F. Allan, and R. Batiza, Small-scale heterogeneities in depleted mantle sources; near-ridge seamount lava geochemistry and implications for mid-ocean-ridge magmatic processes, *Nature (London) 331***,** 511-513, 1988a.

Fornari, D. J., M. R. Perfit, J. F. Allan, and R. Batiza, Geochemical and structural studies of the Lamont Seamounts: Seamounts as indicators of mantle processes, *Earth and Plant. Sci. Letters, 89,* 63-83, 1988b.

Frey, F. A., C. J. Suen, and H. W. Stockman, The Ronda high temperature peridotite: Geochemistry and petrogenesis, *Geochimica et Cosmochimica Acta, 49,* 2,469-2,491, 1985.

Ghiorso, M. S., and R. O. Sack, Chemical mass transfer in magmatic processes. IV. A revised and internally consistent thermodynamic model for the interpolation and extrapolation of liquid-solid equilibria in magmatic systems at elevated temperatures and pressures, *Contributions to Mineralogy and Petrology, 119,* 197-212, 1995.

Hammond, S. R., Offset caldera and crater collapse on Juan de Fuca ridge-flank volcanoes, *Bull. Volcanol., 58,* 617-627, 1997.

Hegner E. and M. Tatsumoto, Pb, Sr, and Nd isotopes in basalts and sulphides from the Juan de Fuca Ridge, *J. of Geophys. Res., 92,* 11,380-11,385, 1987.

Hellebrand, E., J. E. Snow, P. Hope, and A. W. Hofman, Garnet-field melting and late-stage refertilization in "residual" abyssal peridotites from the Central Indian Ridge, *J. Petrology, 43,* 2,305-2,338, 2002.

Ito E., W. M. White, and C. Goepel, The O, Sr, Nd and Pb isotope geochemistry of MORB, *Chemical Geology 62,* 157-176, 1987.

Karsten, J. L., J. R. Delaney, J. M. Rhodes, and R. A. Liias, Spatial and temporal evolution of magmatic systems beneath the Endeavour segment, Juan de Fuca Ridge: Tectonic and petrologic constraints, *J. Geophys. Res., 95,* 19,235-19,256, 1990.

Langmuir, C. H., R. D. Vocke, Jr., and G. N. Hanson, A general mixing equation with applications to Icelandic basalts, *Earth and Planet. Sci. Letters, 37,* 380- 392, 1978.

Langmuir, C. H., E. M. Klein, and T. Plank, Petrological systematics of mid-ocean ridge basalts: Constraints on melt generation beneath ocean ridges, in *Mantle Flow and Melt Generation at Mid-Ocean Ridges, Geophys. Monogr. Ser.,* vol. 71, edited by J. Phipps Morgan, D. Blackman, and J. Sinton, pp. 183-280, AGU, Washington, D. C., 1992.

Leybourne, M. I., and N. A. Van Wagoner, Heck and Heckle seamounts, Northeast Pacific Ocean: High extrusion rates of primitive and highly depleted mid-ocean ridge basalt on off-axis seamounts, *J. Geophys. Res., 96,* 16,275-16,293, 1991.

Lonsdale, P., and F. N. Spiess, A pair of young cratered volcanoes on the East Pacific Rise, *J. Geol., 87,* 157-173, 1979.

Marti, J., G. J. Ablay, T. L. Redshaw, and R. S. J. Sparks, Experimental studies of collapse calderas, *J. Geol. Soc. London, 151,* 919-929, 1994.

MBARI Mapping Team, Santa Barbara Multibeam Survey, Monterey Bay Aquarium Research Institute, Digital Data Series No. 4, 2001.

Menard, H. W., *Marine Geology of the Pacific,* McGraw-Hill, New York. 271 pp, 1964.

Menard, H. W., Growth of drifting volcanoes, *J. Geophys. Res., 74,* 4,827-4,837, 1969.

Niu, Y., and R. Batiza, Trace element evidence from seamounts for recycled oceanic crust in the Eastern Pacific mantle, *Earth Planet. Sci. Lett., 148,* 471-483, 1997.

Perfit M. R., D. J. Fornari, M. C. Smith, J. F. Bender, C. H. Langmuir, and R. M. Haymon, Small-scale spatial and temporal variations in mid-ocean ridge crest magmatic processes, *Geology (Boulder) 22,* 375-379, 1994.

Perfit, M. R., and W. W. Chadwick, Magmatism at mid-ocean ridges: constraints from volcanological and geochemical investigations, *Geophysical Monograph, 106,* 59-115, 1998.

Raddick, M. J., E. M. Parmentier, and D. S. Scheirer, Buoyant decompression melting: A possible mechanism for intraplate volcanism, *J. Geophys. Res., 107:B10,* 17 pp, 2002.

Roche, O., T. H. Druitt, and O. Merle, Experimental study of caldera formation, *J. Geophys. Res., 105,* 395-416, 2000.

Rhodes J. M., C. Morgan, and R. A. Liias, Geochemistry of Axial Seamount lavas; Magmatic relationship between the Cobb hotspot and the Juan de Fuca Ridge; Special section; Axial Seamount; an active ridge axis volcano on the central Juan de Fuca Ridge. *J. Geophys. Res. 95,* 12-12,733, 1990.

Rollinson, H. R., *Using geochemical data; evaluation, presentation, interpretation,* John Wiley & Sons, Inc., New York, NY, 1993.

Schouten, H., H. J. B. Dick, and K. D. Klitgord, Migration of mid-ocean-ridge volcanic segments, *Nature, 326,* 835-839, 1987.

Sleep, N. H., Tapping of magmas from ubiquitous mantle heterogeneities: An alternative to mantle plumes?, *J. Geophys. Res., 89,* 10,029-10,041, 1984.

Smith, M. C., M. R. Perfit, and I. R. Jonasson, Petrology and geochemistry of basalts from the southern Juan de Fuca Ridge: Controls on the spatial and temporal evolution of mid-ocean ridge basalts, *J. Geophys. Res., 99*, 4,787-4,812, 1994.

Stakes, D. S., M. R. Perfit, M. A. Tivey, D. Caress, T. M. Ramirez, and N. Maher, The Cleft Revealed: Geologic, magnetic and morphologic evidence for construction of upper oceanic crust along the southern Juan de Fuca Ridge, *Geochemistry Geophysics Geosystems*, *7*, 2006.

Sun, S.S. and McDonough, W.F., Chemical and isotopic systematics of oceanic basalts; implications for mantle composition and processes, *Magmatism in the ocean basins*, Saunders, A.D. and Norry, M.J. (Editors), Geological Society of London, London, pp. 313-345, 1989.

Takazawa, E., F. A. Frey, N. Shimizu, and M. Obata, Whole rock compositional variations in an upper mantle peridotite (Horoman, Hokkaido, Japan): Are they consisitent with a partial melting process?, *Geochimica et Cosmochimica Acta*, *64*, 695-716, 2000.

Vollmer, R., Rb-Sr and U-Th-Pb systematics of alkaline rocks: the alkaline rocks from Italy, *Geochimica et Cosmochimica Acta, 40*, 283-295, 1976.

White W. M., A. W. Hofmann, and H. Puchelt, Isotope geochemistry of Pacific mid-ocean ridge basalt, *J. Geophys. Res., 92*, 4,881-4,893, 1987.

Zindler, A., H. Staudigel, and R. Batiza, Isotope and trace element geochemistry of young Pacific seamounts: Implications for the scale of upper mantle heterogeneity, *Earth Planet. Sci. Lett., 70*, 175-195, 1984.

BIOGRAPHICAL SKETCH

Rachel Elizabeth Wendt was born one fine June morning in Lakeland, FL, after what was a quite eventful night, which included her father running out of the house wearing naught but shorty-shorts (you know, it was the 80s). Rachel spent most of her childhood in the beachside town of New Smyrna Beach and enjoyed everything that had to do with being outdoors, including hiking, swimming, boogie boarding, climbing trees, riding horses, and playing soccer. During high school, Rachel was the typical over-achiever, and tried (most of the time pretty successfully) to do everything all at once. She was a starter on the varsity soccer team, a class officer, in every honor society possible, and still had time to fit in her weekend job (mucking out stalls at the horse stable). She graduated summa cum laude in 2001.

After that, it was off to the University of Miami, where she (quite by accident) stumbled into geology, after reading a truly inspiring course description. After meeting some truly incredible people, she never looked back and graduated four years later with a bachelor of science in geology and marine science and a minor in religious studies. Finding the need to do more, she moved to Gainesville and started a master of science in geology, where she enjoyed teaching and researching. She completed her master's degree in geology in December 2008.